

HOW TO CONSTRAIN YOUR M DWARF: MEASURING EFFECTIVE TEMPERATURE, BOLOMETRIC LUMINOSITY, MASS, AND RADIUS

ANDREW W. MANN,^{1,2} GREGORY A. FEIDEN,³ ERIC GAIDOS,^{4,5} TABETHA BOYAJIAN⁶, KASPAR VON BRAUN⁷
ApJ accepted

ABSTRACT

Precise and accurate parameters for late-type (late K and M) dwarf stars are important for characterization of any orbiting planets, but such determinations have been hampered by these stars' complex spectra and dissimilarity to the Sun. We exploit an empirically calibrated method to estimate spectroscopic effective temperature (T_{eff}) and the Stefan–Boltzmann law to determine radii of 183 nearby K7–M7 single stars with a precision of 2–5%. Our improved stellar parameters enable us to develop model-independent relations between T_{eff} or absolute magnitude and radius, as well as between color and T_{eff} . The derived T_{eff} –radius relation depends strongly on $[\text{Fe}/\text{H}]$, as predicted by theory. The relation between absolute K_S magnitude and radius can predict radii accurate to $\simeq 3\%$. We derive bolometric corrections to the $VR_CI_CgrizJHK_S$ and *Gaia* passbands as a function of color, accurate to 1–3%. We confront the reliability of predictions from Dartmouth stellar evolution models using a Markov Chain Monte Carlo to find the values of unobservable model parameters (mass, age) that best reproduce the observed effective temperature and bolometric flux while satisfying constraints on distance and metallicity as Bayesian priors. With the inferred masses we derive a semi-empirical mass–absolute magnitude relation with a scatter of 2% in mass. The best-agreement models over-predict stellar T_{eff} s by an average of 2.2% and under-predict stellar radii by 4.6%, similar to differences with values from low-mass eclipsing binaries. These differences are not correlated with metallicity, mass, or indicators of activity, suggesting issues with the underlying model assumptions e.g., opacities or convective mixing length.

Subject headings: stars: fundamental parameters — stars: statistics — stars: abundances — stars: late-type — stars: low-mass — stars: planetary systems

1. INTRODUCTION

Very-low-mass stars ($0.1_{\odot} < M_* < 0.6M_{\odot}$), i.e., late K and M dwarf stars, have become prime targets in the search for exoplanets, particularly Earth-like planets that orbit in circumstellar "habitable zones" where the level of stellar irradiation and a planet's equilibrium temperature permit stable liquid water. M dwarfs dominate the stellar population, comprising more than 70% of all stars in the Galaxy (Henry et al. 1994), and thus their planets weigh heavily on the overall occurrence of planets in the Milky Way. Because transit and Doppler signals increase with decreasing stellar radius (R_*), stellar mass (M_*), and orbital period, Earth-size planets in the habitable zone are much easier to detect around M dwarfs.

Results based on observations by the NASA *Kepler* mission suggest that M dwarfs are teeming with rocky planets, with $\simeq 1$ planet per low-mass star with orbital periods of less than 50 days (Cassan et al. 2012; Morton & Swift 2014; Gaidos et al. 2014). Future space-based

transit surveys such as TESS (Ricker 2014) and PLATO (Rauer et al. 2014) are expected to detect hundreds of rocky planets around *nearby* stars, including M dwarfs. Bright host stars make transit spectroscopy to detect the planets' atmospheres and search for biosignatures possible with observatories such as the *James Webb Space Telescope*.

Estimates of planet properties depend directly on properties of the host stars as well as observables such as transit depth or Doppler radial velocity amplitude, thus it is critical that we have accurate stellar parameters to match the precise measurements achievable with current and planned instrumentation. The radius of the host star R_* is required to establish the radius of a transiting planet. The stellar density ρ_* is required to determine the probability that a planet with a given orbital period is on a transiting orbit and infer the occurrence of such planets around a set of stars targeted by a transit survey. The mass of a planet detected with a given orbital period and radial velocity reflect amplitude scales with mass of the star as $M_*^{2/3}$. The orbit-averaged irradiance on a planet is proportional to stellar luminosity L_* and thus the equilibrium temperature scales as $L_*^{1/4}$. Among other applications, this information is required to determine if a planet falls within a "habitable zone" bounded by runaway greenhouse conditions and the maximum greenhouse effect that a CO₂ atmosphere can provide (Kopparapu et al. 2013).

Stellar parameters are also useful when comparing planetary systems in search of clues to the origins of their diversity. The occurrence of giant planets around FGK

¹ Harlan J. Smith Fellow, University of Texas at Austin; amann@astro.as.utexas.edu

² Visiting Researcher, Institute for Astrophysical Research, Boston University, USA

³ Department of Physics and Astronomy, Uppsala University, Box 516, SE-751 20, Uppsala, Sweden

⁴ Department of Geology and Geophysics, University of Hawai'i at Manoa, Honolulu, HI 96822, USA

⁵ Visiting Scientist, Max Planck Institut für Astronomie, Heidelberg, Germany

⁶ Department of Astronomy, Yale University, New Haven, CT 06511, USA

⁷ Lowell Observatory, 1400 W. Mars Hill Rd., Flagstaff, AZ, USA

dwarfs is a strong function of metallicity (Santos et al. 2004; Fischer & Valenti 2005), and this correlation may also hold for M dwarfs (Johnson et al. 2010; Mann et al. 2013c; Gaidos & Mann 2014). Giant planet occurrence also likely scales with M_* (Johnson et al. 2010; Gaidos et al. 2013), and the occurrence of small, close-in planets appears to increase with decreasing M_* (Howard et al. 2012).

Parameters of M dwarfs can be estimated by direct comparison with model predictions (e.g., Casagrande et al. 2008; Gaidos 2013; Dressing & Charbonneau 2013). Although models of M dwarf atmospheres have continued to advance (Allard et al. 2013; Rajpurohit et al. 2013), there remain important molecular bands that are poorly described or completely omitted. Such an approach is also ultimately unsatisfactory as the interiors and atmospheres of these stars are dissimilar to the Sun and we wish to test the models, not trust them.

Studies of low-mass eclipsing binary systems (LMEBs) find that stellar models systematically under-predict stellar radii and over-predict T_{eff} s by up to 4% (e.g., Kraus et al. 2011; Feiden & Chaboyer 2012a; Spada et al. 2013). The leading hypothesis is that magnetic phenomena (magneto-convection or spots) are responsible for the observed discrepancies, motivated by theoretical predictions (e.g., Mullan & MacDonald 2001) and bolstered by observational evidence (e.g., López-Morales 2007). Further investigations have led to contradictory results, with some studies suggesting magnetic fields are adequate to reconcile models and observations (e.g., MacDonald & Mullan 2012; Feiden & Chaboyer 2013; Torres et al. 2014), while others question the validity of the magnetic hypothesis (e.g., Chabrier et al. 2007; Feiden & Chaboyer 2014a). It is clear that, if magnetic fields are to blame, single inactive field stars are not expected to display significant disagreements with model predictions. However, results from Boyajian et al. (2012b) indicate that single inactive field stars may in fact show similar disagreements.

Recent observational advances have led to more precise, *model-independent* estimates of some M dwarf parameters. Long-baseline optical interferometry (LBOI) has been used to measure the angular diameters (θ), and with trigonometric parallaxes, physical diameters, of some very nearby, bright M dwarfs with uncertainties of 1-5% (e.g., Boyajian et al. 2012b; von Braun et al. 2014). The angular diameter plus the parallax yields the physical stellar radius. The angular diameter plus an estimate of the star’s bolometric flux (F_{bol}) yields a direct determination of T_{eff} via the Stefan–Boltzmann law:

$$T_{\text{eff}} = 2341 \left(\frac{F_{\text{bol}}}{\theta^2} \right)^{1/4}, \quad (1)$$

where F_{bol} is in units of $10^{-8} \text{ erg s}^{-1} \text{ cm}^{-2}$. These estimates are thus model-independent (with the exception of small limb darkening corrections to angular diameters) and are applicable to single stars (close binaries being obvious in interferometric data).

Effective temperatures derived from fits to model grids can be compared to these bolometrically derived temperatures to calibrate or correct the former to within 60 K (Mann et al. 2013b). Likewise, improvements in the accuracy of photometric zero points and system passbands (Mann & von Braun 2015) allow *bolometric fluxes* to be

measured to an accuracy of $\lesssim 1\%$ using well-calibrated, high signal-to-noise (S/N) spectra. *Metallicities* of M dwarfs have previously eluded precise determination because analysis of spectra visible wavelengths is complicated by confusion of many overlapping lines and the lack of a well-defined continuum. However, the isolated lines in infrared spectra, combined with calibration by observations of common proper motion pairs of solar-type stars and M dwarfs, have been recently to estimate $[\text{Fe}/\text{H}]$ to a precision as good as 0.07 dex (e.g., Neves et al. 2012; Terrien et al. 2012; Mann et al. 2013b; Newton et al. 2014). These estimates are model-independent to the extent that the metallicities of the solar-type calibrators are derived independently of any model assumptions but will nonetheless be affected by any systematic errors in the latter (Mann et al. 2013a).

Precise parameter values for calibrator M dwarfs can be used to construct empirical relations between parameters that are, in principle, applicable to fainter, more distant stars for which distances or angular diameters are currently unobtainable (Mann et al. 2013b). They can also be used to test models of M dwarf interiors and atmospheres (e.g., Boyajian et al. 2015). However, only a small ($\simeq 30$) number of M dwarfs are near and bright enough for observations by LBOI. This restricts the calibration to hotter values of T_{eff} and sparsely samples the relevant range of $[\text{Fe}/\text{H}]$. For example, it has been difficult to evaluate whether R_* increases with $[\text{Fe}/\text{H}]$ for a fixed T_{eff} , a basic prediction of models.

If T_{eff} and F_{bol} can be determined without interferometry, Equation 1 can be inverted to estimate θ , and with a trigonometric parallax, physical radius. Because precise spectroscopic temperatures, bolometric fluxes, and trigonometric parallaxes can be obtained for a much larger number of stars than are reachable with existing LBOI instrumentation, this greatly expands the potential pool of calibrators. A similar method called Multiple Optical-Infrared Technique (MOITE) has been used to determine the radii of M dwarfs (Casagrande et al. 2008). However, that method is sensitive to the model temperatures and photometric zero points.

In this work we present estimates of F_{bol} , T_{eff} and $[\text{Fe}/\text{H}]$ for 183 bright nearby M dwarfs with precise trigonometric parallaxes, which we use to determine R_* . We construct improved empirical relations between these parameters and confront the predictions of models of M dwarfs with these values. In Section 2 we define the sample. We describe our spectroscopic observations in Section 3 and how we turn spectra into determinations of F_{bol} , T_{eff} , $[\text{Fe}/\text{H}]$, and R_* in Section 4. We compare our estimates to values available from the literature in Section 5. Using our derived M dwarf parameters, we develop empirical relations between observables (i.e., color, T_{eff} , and M_{K_S}) and fundamental parameters (R_* , L_{bol}) in Section 6, and provide empirical bolometric corrections in Section 7. We compare predictions from the Dartmouth stellar evolutionary model (Dotter et al. 2008) to our values in Section 8, including exploring the impact of changes in the model physics. We conclude in Section 9 with a summary of our work, a brief discussion of some of the issues with our analysis, and potential applications of our methods with the advent of extremely precise trigonometric parallaxes from the ESO *Gaia* astrometric mission.

2. SAMPLE SELECTION

M dwarf stars were selected from the CONCH-SHELL (Gaidos et al. 2014) or LG11 (Lépine & Gaidos 2011) catalogs. We first selected stars with parallax errors $< 5\%$. Trigonometric parallaxes were taken from Harrington et al. (1993), Jao et al. (2005), Henry et al. (2006), van Leeuwen (2007), Gatewood (2008), Gatewood & Coban (2009), Lépine et al. (2009), Riedel et al. (2010), Jao et al. (2011), and Dittmann et al. (2014). For targets with multiple parallax measurements we adopted the distance from the most precise measurement. This selection yielded 923 stars, about two thirds of which are visible to our instruments/telescopes (Section 3). We prioritized our spectroscopic observations for targets based on: (i) error in stellar parallax, (ii) brightness, and (iii) estimated spectral type or color (since late-type stars tend to be removed by the first two criteria. Existing optical and/or near-infrared (NIR) spectra (Lépine et al. 2013; Mann et al. 2013b; Gaidos et al. 2014) were used where available.

Our prioritization coupled with available observing time yielded 191 stars. To this we added an additional 36 M dwarfs in wide ($\gtrsim 5''$) binaries from Mann et al. (2013a) and Mann et al. (2014). These M dwarfs did not make the original cut because they do not have trigonometric parallaxes or a sufficiently precise trigonometric parallaxes. However, their primaries have parallaxes, which we use to calculate the distance to the M dwarf companion. We also added three M dwarfs with LBOI θ measurements that were not in the LG11 or CONCH-SHELL catalogs. We then removed three stars because of insufficient (< 5 points) photometry to absolutely calibrate the spectrum (see Section 3.3) or because there was poor agreement between photometry and spectra, i.e., reduced $\chi^2 > 10$ (χ_ν^2).

2.1. Binary Contamination

Unresolved binaries are problematic for our analysis. Unlike photometric variability, which changes the photometry and any derived stellar properties randomly, an unresolved and uncorrected companion will always increase F_{bol} , and hence systematically bias the radii of the overall sample. It has been estimated that $\simeq 40\%$ of M dwarfs in the solar neighborhood have at least one companion within 1000 AU (Fischer & Marcy 1992; Lada 2006; Raghavan et al. 2010). The median distance to our targets is 10 pc, so the majority of these were sufficiently separated ($> 5''$ or > 50 AU) such that the photometry and spectroscopy is unaffected. We flagged all binaries that are resolved in the spectrographs finder cameras (Section 3), which is capable of detecting companions with $\Delta K \lesssim 2$ and as close as $1 - 2''$ to the primary, depending on conditions. Systems with high contrast ratios ($\Delta K \gg 2$) which were more likely to be missed have a negligible effect on the F_{bol} (see below).

To identify tighter binaries we crosschecked our sample with the Fourth Catalog of Interferometric Measurements of Binary Stars (Hartkopf et al. 2001), the Washington Double Star Catalog (Mason et al. 2001), and SIMBAD. Each of these catalogs reports heterogeneous information, e.g., contrast ratios are not always given in the same filter and sometimes just spectral types are given rather than flux differences. To deal with this heterogeneity, we use our sample to estimate the impact of binarity on

our derived parameters as a function of contrast ratio or spectral type. We scaled all spectra in our sample so that they are at the same distance (10 pc, but the exact value is arbitrary) then added random pairs of spectra together, calculating F_{bol} before and after addition (Figure 1). We removed any target with a companion that would increase F_{bol} by more than 8%. This cut was selected because an 8% increase in F_{bol} results in a 2% increase in derived R_* , which is still less than our typical measurement errors. This binarity criterion removed 41 targets, or 18% of the sample.

Using the binary period distribution from Raghavan et al. (2010) and the overall binarity rate for M dwarfs from Fischer & Marcy (1992) we estimated that $\simeq 17\%$ of our sample contains binaries that are tight enough to be unresolved in our photometry/spectroscopy and not resolved in SpeX/SNIFS finder images, but could have increased the derived F_{bol} by $\gtrsim 8\%$. The actual binarity rate may differ in our sample because it is not volume-limited while the binary fraction estimates are. However, the expected binary fraction is consistent with or lower than the fraction of targets that were removed because they are known binaries (18%), suggesting binary contamination will not be a significant problem for our analysis. Most of our targets are close, and have been studied extensively for companions (e.g., Janson et al. 2012, 2014; Ansdell et al. 2015), and hence the agreement between the estimated and observed binarity is not surprising.

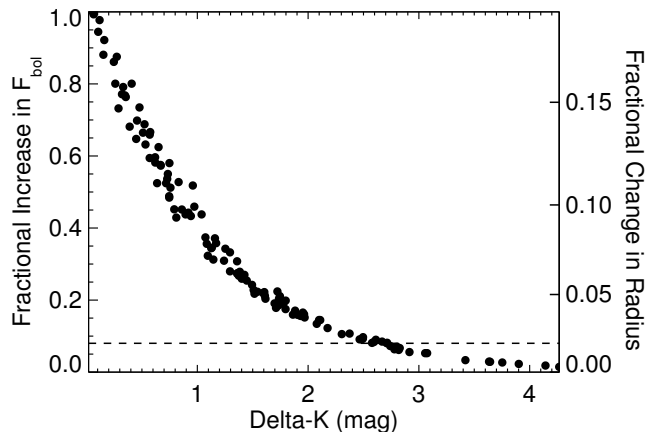


Figure 1. The effect on the derived F_{bol} and R_* from an unresolved binary as a function of the K -magnitude contrast ratio. The dashed line indicates the maximum change in F_{bol} (8%) from a binary, above which we remove the target from our sample. The scatter in the locus of points is larger than expected from measurement errors because we are combining spectra of a range of metallicities, and therefore have varying F_{bol} 's for a given M_K . More details can be found in Section 2.1.

The final sample contains 183 stars with spectral types ranging from K7 to M7 (median spectral type of M3), $[\text{Fe}/\text{H}]$ from -0.60 to $+0.53$ (median $[\text{Fe}/\text{H}]$ of -0.03), and distances from 1.8 pc (Barnard's Star) to 38 pc (median distance of 11 pc).

3. OBSERVATIONS AND REDUCTION

3.1. Optical Spectra from SNIFS and STIS

Optical spectra of all stars were obtained with the SuperNova Integral Field Spectrograph (SNIFS, Aldering et al. 2002; Lantz et al. 2004) on the University of Hawai'i 2.2m telescope on Mauna Kea. SNIFS provides simultaneous coverage from 3200–9700 Å by splitting the beam with a dichroic mirror onto blue (3200–5200 Å) and red (5100–9700 Å) spectrograph channels. Although the spectral resolution of SNIFS is only $R \simeq 1000$, the instrument provides excellent spectrophotometric precision (Mann et al. 2011, 2013b). This is in part a consequence of the stability of the atmosphere over Mauna Kea (Hill et al. 1994; Buton et al. 2013) and because the instrument is an integral field spectrograph and does not suffer from wavelength dependent slit losses that can be difficult to accurately remove.

Spectra were obtained between 2010 and 2014 under varying conditions, although most nights were photometric or nearly photometric (few to zero cloud cover). Integration times varied from 2 to 600 s, yielding S/N > 100 per resolution element in the red channel for all targets, while avoiding the non-linear regime of the detector. For exposure times < 5 s, multiple exposures were taken and stacked after reduction to suppress scintillation noise.

SNIFS data reduction was broken into two parts: initial reduction from the SuperNova Factory (SNF) team pipeline, which was performed concurrently with all observations, and a more precise flux calibration and telluric correction, which we applied to the SNF pipeline reduced data. Detailed information on the SNF pipeline can be found in Bacon et al. (2001) and Aldering et al. (2006). To summarize, the SNF pipeline performed dark, bias, and flat-field corrections, and cleaned the data of bad pixels and cosmic rays. It then fit and extracted each of spectra from the 15×15 "spaxels" in the red and blue channels and converted these into spectral-spatial image cubes. The pipeline applied a wavelength calibration to the cubes based on arc lamp exposures taken at the same telescope pointing and time as the science data, and a rough flux calibration based on an archive correction. Lastly, the pipeline extracted one-dimensional spectra from each of the cubes using an analytic model of the point spread function.

Our part of the reduction is described in some detail in Lépine et al. (2013) and Gaidos et al. (2014). We restate most of the process here as there has been some improvements in our data reduction since the publication of those papers. Over several years of observing with SNIFS we collected more than 400 observations of 42 spectrophotometric standards⁸. We first identified all standard star observations taken on photometric nights based on extinction estimates from the CFHT skyprobe⁹. We divided the "true" spectrum of each standard star, as taken from the literature (Oke 1990; Hamuy et al. 1994; Bessell 1999; Bohlin et al. 2001), by the corresponding spectra from the SNF pipeline. We then found the best-fit correction as a function of airmass:

$$\kappa(\lambda) = a(\lambda) + b(\lambda)z + c(\lambda)z^2, \quad (2)$$

where κ is the true atmospheric (including telluric) and instrumental correction, z is the airmass, and a , b , and c

are fit variables that also depend on wavelength (λ). We compared this model derived from all photometric nights to a correction derived using just standards taken in a single night. We found that the differences between these corrections is only $\simeq 1\%$ in the red and $\lesssim 2\%$ in the blue, excluding regions of significant telluric contamination. For a more accurate flux calibration we took the median derived correction from all standard stars observed in a single night (without an airmass fit), which we used to derive an additional wavelength dependent adjustment we applied to κ (in addition to Equation 2). The final correction was then applied to all stars from that night. This assumes that while the atmospheric transparency (a) varies between nights, the effect of airmass (b , c) does not.

Five of our stars are included in the Next Generation Spectral Library (NGSL, Gregg et al. 2006; Heap & Lindler 2007), which consists of spectra obtained with the Space Telescope Imaging Spectrograph (STIS) on the *Hubble Space Telescope* (HST) using the G230LB, G430L, and G750L gratings. NGSL spectra cover 2000–10000 Å with spectrophotometric precision of $\simeq 0.5\%$ (Bohlin et al. 2001; Bohlin & Gilliland 2004a,b). We used the NGSL instead of the SNIFS data for these five stars.

To test the quality of our spectrophotometric calibration we compared our SNIFS data to the NGSL spectra for the five overlapping targets. We found that we can reproduce the HST spectra with a scatter (1σ) of 1.1% in the red and 1.5% in the blue, with median offsets of 0.1% and 0.3% respectively. We added this estimate of the systematic error in quadrature to the formal errors in each spectrum for our error analysis of F_{bol} (Section 4).

3.2. Near-infrared (NIR) Spectra from SpeX

Between 2012 and 2014 we obtained NIR spectra of all stars using the SpeX spectrograph (Rayner et al. 2003) attached to the NASA Infrared Telescope Facility (IRTF) on Mauna Kea. As with the SNIFS observations, data were taken under mixed conditions, but most nights were photometric or near-photometric. SpeX observations were taken in the short cross-dispersed (SXD) mode using the $0.3 \times 15''$ slit, yielding simultaneous coverage from 0.8 to $2.4\mu\text{m}$ with a small gap at $\simeq 1.8\mu\text{m}$, and at a resolution of $R \simeq 2000$. Each target was placed at two positions along the slit (A and B) and observed in an ABBA pattern in order to subsequently subtract the sky background. For each star we took 6–10 exposures following this pattern, which, when stacked, provided a S/N per resolution element of > 100, and typically > 150 in the *H*- and *K*-bands. In 2014 July the SpeX chip was upgraded (now called uSpeX), which resulted in better wavelength coverage (0.7– $2.5\mu\text{m}$), including coverage of the region between the *H* and *K* bands that SpeX lacked. In total, 18 of 183 stars were observed with uSpeX. Observation procedures and reduction were nearly identical for the two detectors.

SpeX and uSpeX spectra were extracted using the SpeX-Tool package (Cushing et al. 2004), which performed flat-field correction, wavelength calibration, sky subtraction, and extraction of the one-dimensional spectrum. Multiple exposures were combined using the IDL routine *xcombpec*. To correct for telluric lines, we observed an A0V-type star within 1 hr and 0.1 airmass of the target observation (usually much closer in time and airmass). A telluric correction spectrum was constructed from each A0V star

⁸ Full list at <http://snfactory.lbl.gov/snf/snf-specstars.html>

⁹ <http://www.cfht.hawaii.edu/Instruments/Skyprobe/>

and applied to the relevant spectrum using the *xtellcor* package (Vacca et al. 2003). Separate orders were stacked using the *xcombspec* tool, which also shifts the flux level in each orders to match. These corrections are generally 1% or less per order.

Rayner et al. (2009) noted that using the 0.3'' slit can lead to errors in the slope of the spectrum by 1-3% due to changes in seeing, guiding, and differential atmospheric refraction between target and standard star observation. We reduced the impact of this problem by observing at the parallactic angle and minimizing the time between target and standard star observations. We compared the slopes of unstacked observations of the same star and found that slope errors are 1 – 2%, which is backed up by a comparison *JHK* magnitudes from the literature (Mann & von Braun 2015). This source of error was included in all analyzes.

3.3. Absolute Flux Calibration of Spectra

SpeX spectra have a gap at $\simeq 1.8\mu\text{m}$ between the *H* and *K* bands, although there is no gap for uSpeX data. Also, several regions in the NIR are strongly affected by telluric absorption. Although our observations of A0V stars enabled us to correct for telluric absorption, the S/N in some regions was too low for accurate reconstruction of the spectra. We replaced these regions with the best-fit atmospheric model from the BT-SETTL grid (Allard et al. 2011, 2013). We did the same for 2.4–10 μm . Our method for finding the best model spectrum is explained in Section 4. As a test, we examined the spectra of the 12 targets with S/N > 500 in the NIR, and found that using a model to replace the regions of telluric contamination changes the derived F_{bol} by $0.15\pm 0.26\%$, and hence adds negligible error.

Blueward of our cutoff at 0.32 μm (0.2 μm for targets with STIS spectra) we assumed the spectrum follows Wein’s approximation and redward of 10 μm we assumed it follows the Rayleigh-Jeans law. We fit these functions using the data at 0.3–0.4 μm and 2.0–10 μm , respectively. Flux in each of these regions represented $\ll 1\%$ of the total flux from a typical star, and comparison to photometry from the *Wide-field Infrared Survey Explorer* (*WISE*, Wright et al. 2010) and UV spectra from STIS (Heap & Lindler 2007) indicated that these approximations are negligible compared to other measurement errors.

For each star we retrieved (where available) *JHK_S* photometry from the Two-Micron All-Sky Survey (2MASS, Skrutskie et al. 2006), *BV* photometry from the AAVSO All-Sky Photometric Survey (APASS, Henden et al. 2012), *H_P* from *Hipparcos* (van Leeuwen 2007), *V_T* and *B_T* from Tycho-2 (Høg et al. 2000), *W1* and *W2* from *WISE* (Wright et al. 2010), and all photometry from the General Catalog of Photometric Data (Mermilliod et al. 1997). We discarded APASS data for stars brighter than $V = 10$ where images were potentially saturated. Much of the *WISE* photometry was saturated or had measurement quality flags and hence was discarded. Photometric magnitudes were converted to fluxes using the zero points from Cohen et al. (2003) for 2MASS, Jarrett et al. (2011) for *WISE*, and Mann & von Braun (2015) for all other photometry. The number of photometric points per star varied from 5 to 179, with a median of 22.

We calculated fluxes from the spectrum (synthetic photometry) corresponding to the available photometry using

the formula:

$$f_{\text{spec},x} = \frac{\int f_{\lambda}(\lambda)S_x(\lambda)d\lambda}{\int S_x(\lambda)d\lambda}, \quad (3)$$

where $f_{\lambda}(\lambda)$ is the spectrum (radiative flux density) as a function of wavelength (λ) and $S_x(\lambda)$ is the system throughput the filter x (e.g., *U*, *B*, *V*) in energy units. As with the zero points, filter profiles were taken from Cohen et al. (2003), Jarrett et al. (2011), and Mann & von Braun (2015). We calculated the ratio of the synthetic flux to that derived from the photometry for each band as well as corresponding uncertainties accounting for errors in the spectrum, photometry, and photometric zero points.

Excluding the five stars with STIS spectra, each of our stars had a spectrum composed of three components from the SNIFS blue channel, the SNIFS red channel, and SpeX. The blue and red channels were relatively flux-calibrated independently from our reduction explained in Section 3.1. However, repeat measurements and comparison with spectra from other instruments suggested that the relative flux calibration between these two channels is only accurate to 3%, while the calibration is accurate to 1% within a channel. The overlapping region covers only $\simeq 50\text{\AA}$ and this spectral region of the instrument has little throughput and hence low S/N. For the SpeX to SNIFS transition there is significantly more overlap ($> 600\text{\AA}$), but this region is complicated by telluric H₂O absorption, low throughput for SpeX, and small but significant shape errors ($\lesssim 1\%$ in the optical and 2% in the NIR) above the Poisson and measurement errors (typically $\ll 1\%$). We used the overlapping region between SNIFS and SpeX (excluding 50 \AA on each end) data to calculate an offset and error, but the result is dominated by errors in the shape of each spectral component.

The absolute fluxes of the three components of each spectrum were adjusted to minimize the difference (in standard deviations) between SNIFS and SpeX overlapping regions, the difference between photometric and spectroscopic fluxes (as described above), and the independent flux calibrations of the SNIFS red and blue channels. This renormalization process served to both combine the three components and absolutely flux calibrate each complete spectrum. For the targets with STIS data there is no separate blue channel, so the analysis had one fewer free parameter, but otherwise the method was the same. We show combined and absolutely calibrated spectra of four representative stars (Gl 699, Gl 876, Gl 880, and Gl 411) in Figure 2. These four are highlighted because they span a wide range of parameter space in terms of stellar mass and metallicity; two are below the fully convective boundary (Gl 699 and Gl 876), two above (Gl 411 and Gl 880), two metal-poor (Gl 699 and Gl 411), and two metal-rich (Gl 876 and Gl 880).

The median reduced χ^2 (χ^2_{ν}) value for our fits was 1.5, and the highest was 7.0 (for Gl 725B). Many of the χ^2_{ν} values > 1 may be due stellar variability, which was not accounted for in our error analysis. Conversely, the low χ^2_{ν} of the sample suggests that either the number of highly variable stars in the sample is relatively low, or that errors are somewhat overestimated.

4. DERIVATION OF STELLAR PARAMETERS

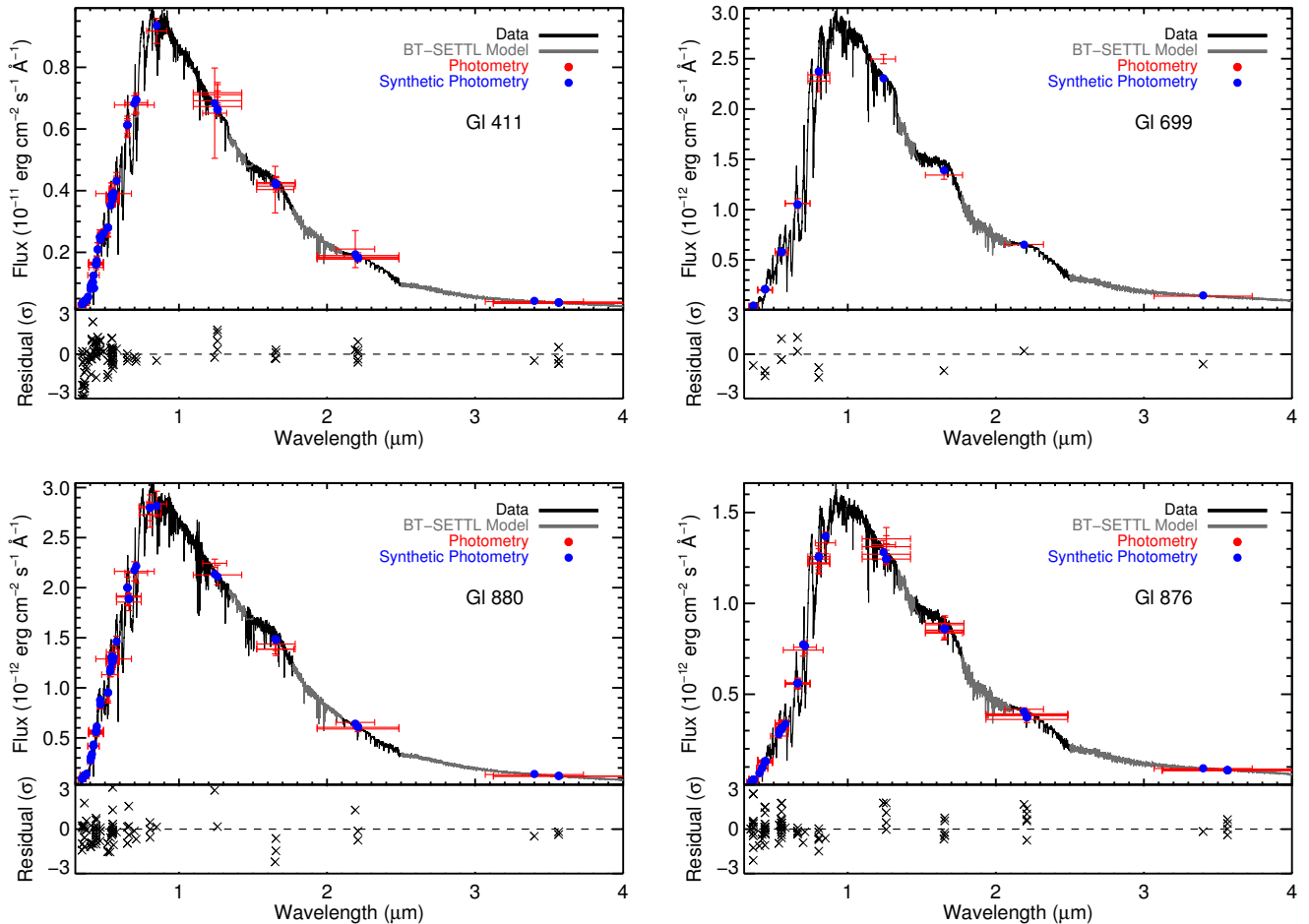


Figure 2. Combined and absolutely flux-calibrated spectra of four representative stars in our sample. The spectra are shown in black, with regions replaced by models in gray. Photometry is shown in red, with the horizontal ‘error bars’ indicating the width of the filter, and vertical errors representing combined measurement and zero point errors. Blue points indicate the corresponding synthetic fluxes calculated using Equation 3. Residuals are plotted in the bottom subpanels in units of standard deviations. More details on observations can be found in Section 3 and absolute flux calibration in Section 3.3. These stars are selected because they roughly span the parameter space in metallicity and mass of our whole sample.

Using the absolutely flux-calibrated spectra (Section 3.3) and trigonometric parallaxes from the literature (Section 2) we calculated F_{bol} , T_{eff} , $[\text{Fe}/\text{H}]$, R_* , M_* , synthetic photometry (Equation 3), and spectral types for all targets in our sample. For these calculations we ignored interstellar extinction, as all stars are within 40 pc and Aumer & Binney (2009) showed that reddening is $\simeq 0$ for stars within 70 pc due to the Local Bubble. Allowed reddening to float had negligible effects on the F_{bol} determinations, reinforcing this assumption. We also assumed every star is single, or a resolvable binary, i.e., each spectrum and photometric measurement is from just one object (also see Section 2.1). Details of our calculations follow. Values and formal errors for all stellar parameters are reported in Table 5, with the synthetic photometry given in Table 6.

4.1. Spectral Type

Spectral types were determined from our optical spectra following the procedure from Lépine et al. (2013). We calculated CaH2, CaH3, TiO5, TiO6, VO1, and VO2 band indices for each of the optical spectra following the definitions given in Reid et al. (1995) and Lépine et al.

(2003). We then applied the empirical relations between these indices and stellar spectral type provided by Lépine et al. (2013). The assigned spectral type was the weighted (by the measurement error of the index) mean of spectral types from each empirical relation (six in total, but VO1 and VO2 were only used if the star is later than M3). This method gives consistent spectral types to those assigned by-eye and has an accuracy of ± 0.3 subtypes (Lépine et al. 2013). The use of indices instead of template matching allowed us to assign fractional subtypes, which is justified given the uncertainties.

4.2. Bolometric Flux

The bolometric flux (F_{bol}) was calculated by integrating over the radiative flux density (the spectrum). Errors on F_{bol} were calculated from Monte Carlo randomization of our flux calibration. Specifically, we randomly varied the photometry, spectra, and photometry zero points according to their estimated errors. We then repeated the process described in Section 3.3 10,000 times, recalculating F_{bol} each time. We used the standard deviation of these values as the error on F_{bol} . While many of our stars have $S/N \gg 100$ and $\gg 20$ photometric points, other

sources of error (e.g., flux calibration, photometric zero points) are typically 0.5-2% and usually dominate the error budget. As a result no star has a F_{bol} error $< 0.5\%$, and typically the error is $\gtrsim 1\%$.

Due to slight modifications in our procedure for combining optical and NIR spectra, updates to our SNIFS reduction pipeline, and changes in the photometry zero points and filter profiles (Mann & von Braun 2015), our F_{bol} values are slightly different from those presented in Mann et al. (2013b) for the interferometry stars. However, these differences are almost all $< 1\sigma$. Further, our F_{bol} values are in good agreement with those determined using the (similar) procedure outlined in van Belle et al. (2008) and von Braun et al. (2011) provided the same photometric zero points are used.

4.3. Effective Temperature

T_{eff} was calculated by comparing our optical spectra with the CFIST suite¹⁰ of the BT-SETTL version of the PHOENIX atmosphere models (Allard et al. 2013). More details of this procedure are given in Mann et al. (2013b) and Gaidos et al. (2014), although we modified their methods slightly. Unlike Gaidos et al. (2014) we did not fit and remove a polynomial trend in wavelength to correct for slit losses, as the flux calibration of SNIFS is better than many of the instruments used in the Gaidos et al. (2014) study. Like Gaidos et al. (2014) we used linear combinations of the three best models to interpolate between grid points, while Mann et al. (2013b) used only two. Mann et al. (2013b) used $[\text{Fe}/\text{H}]$ to restrict which models are allowed in the fit, while this work and Gaidos et al. (2014) added $[\text{Fe}/\text{H}]$ as a term in the equation for χ^2 . These differences resulted in almost negligible changes to the overall sample T_{eff} (median change of 8 K) between the three papers, although several stars changed by >100 K.

Errors in T_{eff} were calculated as the quadrature sum of the calibration error found by Mann et al. (2013b) and the scatter in T_{eff} from the model comparison. Generally the first term dominates, resulting in typical errors in T_{eff} of $\simeq 60$ K.

4.4. Metallicity

Metallicities were calculated from the NIR spectra using the empirical relations from Mann et al. (2013a) for K7-M4.5 dwarfs and from Mann et al. (2014) for M4.5-M7 dwarfs. Mann et al. (2013a, 2014) provide relations between the equivalent widths of atomic features (e.g., Na, Ca) in NIR spectra and the metallicity of the star, calibrated using wide binaries with an FGK primary and an M dwarf companion. Errors on $[\text{Fe}/\text{H}]$ were calculated by adding (in quadrature) measurement errors in the spectra and scatter in the empirical calibration. Comparison with other methods of measuring M dwarf metallicities (e.g., Terrien et al. 2012; Neves et al. 2013; Newton et al. 2014) suggests that our internal errors are only 0.04-0.06 dex (Gaidos & Mann 2014), which is significantly lower than the error estimated by Mann et al. (2013a) and Mann et al. (2014). This might be due to overlap in the calibration sample of the aforementioned studies, or underestimated errors in the FGK star metallicities (Torres et al. 2012;

Hinkel et al. 2014). We conservatively adopt the larger value as the calibration error, which, because the S/N of our spectra is generally very high, dominate the total error in $[\text{Fe}/\text{H}]$.

For 17 of the wide wide binaries among our current sample we adopted the metallicity reported for the primary. These metallicities are more precise (errors typically 0.03-0.05 dex) than those derived from our NIR spectra for the M dwarf.

Metallicities reported here differ slightly from those in Gaidos et al. (2014). Gaidos et al. (2014) based their $[\text{Fe}/\text{H}]$ values on the optical metallicity calibration of Mann et al. (2013a), while ours are based on the NIR calibration. The optical calibration gives $[\text{Fe}/\text{H}]$ accurate to 0.10–0.13 dex, depending on spectral type, while the NIR calibration is good to 0.08 dex. For the stars with $[\text{Fe}/\text{H}]$ measurements in both samples the standard deviation of the differences is 0.10 dex with a mean offset of 0.017 ± 0.007 , consistent with the expected errors.

4.5. Synthetic Photometry

We synthesized $VR_{CI}JHK_S$ photometry using the absolutely flux-calibrated spectra using Equation 3 and procedure from Section 3.3. We generated SDSS *griz* magnitudes using the zero point and filter profiles from the Sloan Digital Sky Survey¹¹ (Fukugita et al. 1996). We also calculated *Gaia* G , G_{BP} , and G_{RP} magnitudes (Jordi et al. 2010). The *Gaia* system profiles were provided by C. Bailer-Jones (2015, personal communication), and the zero point was estimated using a calibrated STIS spectrum of Vega (Bohlin 2007) and assuming $G_{\text{Vega}} = 0.03$. Readers are cautioned that the system throughput we used for *Gaia* passbands may prove to be inaccurate once the mission does its own on-sky calibrations. Hence our derived magnitudes could require corrections for small color terms or zero point errors when real *Gaia* magnitudes become available.

Generating synthetic photometry ensured that we had a homogeneous set of *all* relevant magnitudes for every star. This also provided us with SDSS *griz* magnitudes, which are not available for nearly all the stars in our sample. Further, in many cases our synthetic photometry was superior to the literature photometry in terms of precision and accuracy. While almost all stars have 2MASS JHK_S magnitudes, many of the objects are brighter than the linearity/saturation limit, and hence the 2MASS JHK_S magnitudes are unreliable.

4.6. Mass

Masses for each target were derived using the empirical mass-luminosity (M_K -mass) relation in Delfosse et al. (2000), which was based on mass measurements of M dwarf eclipsing and astrometric binaries. We converted our synthetic K_S magnitudes to CIT K magnitudes using the corrections in Carpenter (2001), i.e., a shift of $\simeq 0.02$ mag. Based on the scatter between the relation and the binaries in Delfosse et al. (2000) we assumed 10% errors on our masses derived this way.

4.7. Angular Diameter and Physical Radius

¹¹ We followed the procedure outlined at <http://classic.sdss.org/dr7/algorithms/fluxcal.html>, so these are true SDSS magnitudes.

¹⁰ <http://phoenix.ens-lyon.fr/Grids/BT-Settl/CIFIST2011/>

Angular diameters were calculated from T_{eff} and F_{bol} using Equation 1. Radii were then determined from θ and the trigonometric parallax for each star. Errors on R_* and θ were estimated by Monte Carlo simulation. We randomly perturbed the T_{eff} and F_{bol} according to estimated errors (see above), and the parallax according to errors reported in the literature. We then recalculated all relevant parameters for each star. We repeated this process 10,000 times. We adopted the standard deviation of these 10,000 iterations as the error in each parameter. There derived values show significant correlations between parameters (e.g., T_{eff} and R_*), which are accounted for by the MC error estimate.

Errors on R_* are typically $\simeq 3 - 4\%$, although they tend to be larger with decreasing R_* . Our F_{bol} values are generally very precise (1–2%) as are our constraints on T_{eff} ($\simeq 2\%$). However, because $\theta \propto F_{\text{bol}}^{1/2}$ and $\theta \propto T_{\text{eff}}^{-2}$, errors in θ (and hence R_*) are primarily driven by errors in T_{eff} . Trigonometric parallax errors are typically 2%, and hence also noticeably contribute to errors in R_* .

5. COMPARISON WITH PREVIOUSLY PUBLISHED PARAMETER VALUES

5.1. Interferometric T_{eff} and θ

Twenty-nine stars in our sample have interferometric radii in Lane et al. (2001), Ségransan et al. (2003), Berger et al. (2006), Kervella et al. (2008), Demory et al. (2009), von Braun et al. (2011), von Braun et al. (2012), Boyajian et al. (2012b), von Braun et al. (2014), or Boyajian et al. (2015, in preparation). We derived radii for these stars in the same manner as was done for every other star, i.e., we took SNIFS and SpeX spectra of these stars, absolutely flux-calibrated the spectra, measured the temperature by fitting to atmospheric models, and then derived θ and R_* . We also recalculated interferometric T_{eff} for these stars using the LBOI θ measurements and our F_{bol} values using Equation 1 (although our conclusions do not change significantly if we use the T_{eff} and F_{bol} values from the original reference).

Agreement between the T_{eff} and θ determinations is excellent (Figure 3). The mean difference in T_{eff} is 20 ± 11 K and the χ^2_ν is 0.90. Similarly, the mean difference in θ is $1.4 \pm 0.7\%$ with a χ^2_ν of 1.01. Our method for measuring T_{eff} was tuned (choice of atmospheric model and spectral regions utilized) to match LBOI measurements (see Mann et al. 2013b, for more details), so consistency is not surprising. However, Mann et al. (2013b) had only 18 LBOI stars in this T_{eff} range, while the expanded sample used here includes 29 LBOI stars, so this comparison is still demonstrative. The near-unity χ^2_ν values suggest that our assigned errors are reasonable. Importantly, there is no statically significant correlation between the R_* residuals and $[\text{Fe}/\text{H}]$, or T_{eff} , suggesting that our R_* determinations are clean of systematic errors.

The largest discrepancy between our values and those from LBOI is for the star Gl 725B. Our T_{eff} was 3.6σ warmer, and our radius was 3.4σ smaller than LBOI estimates. Assuming the interferometric parameters are correct, Gl 725B has a significantly larger radius than stars of similar T_{eff} . Photometry is also in relatively poor agreement with the spectrum compared to most stars ($\chi^2_\nu \simeq 7$, see Section 3.3). Photometry for this star may be inaccurate, which would have affected our derived ra-

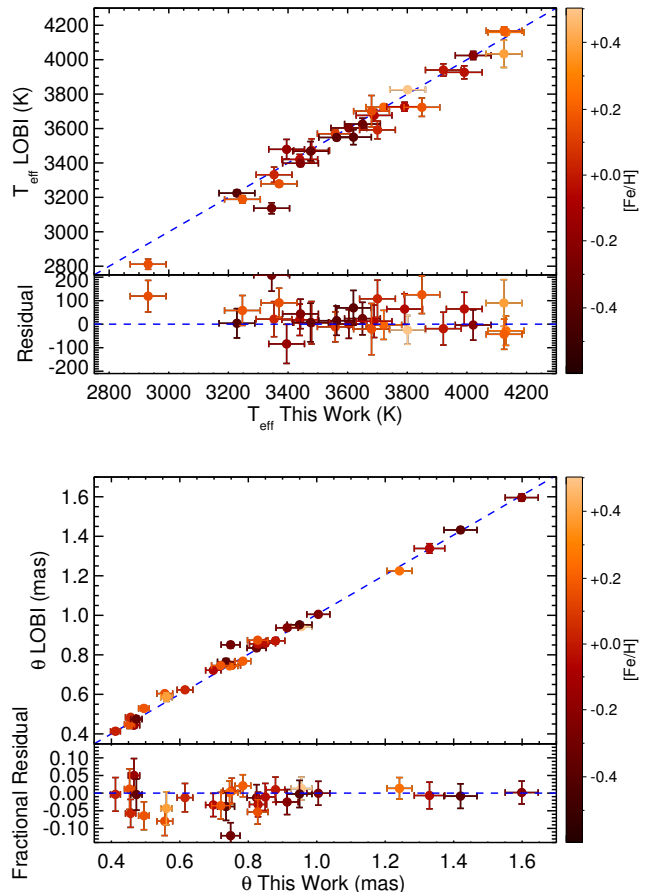


Figure 3. Comparison of T_{eff} (left) and angular diameter (θ , right) determined through our methods (Section 4) compared to those determined from interferometry (LBOI). Bottom panels in both plots show the residuals. All points are color-coded by metallicity. Details are in Section 5.1.

dius and the LBOI T_{eff} . However, F_{bol} would need to be increased by $\gtrsim 20\%$ to reach $\leq 1\sigma$ agreement between the two determinations (although increased by just 4% increase to achieve agreement at 3σ). Variability cannot explain the difference; the scatter in V -band measurements for Gl 725B is $\lesssim 0.02\%$ and the LBOI visibility curve shows no sign of multiplicity.

5.2. M_* - R_* from Low-mass Eclipsing Binaries

We compared our derived masses and radii to those from low-mass eclipsing binaries (LMEBs). Since unresolved binaries hamper our F_{bol} and T_{eff} estimates, and most LMEBs do not have trigonometric parallaxes (or sufficiently precise parallaxes) we did not make a direct comparison as we did with the interferometry targets. Instead we could only see if the trends in the data are in agreement. We compare with a collection of detached, double-line eclipsing binaries with mass and radius errors less than 5% in Figure 4. LMEB parameters are taken from Torres & Ribas (2002), Ribas (2003), López-Morales & Ribas (2005), Lopez-Morales et al. (2006), López-Morales & Shaw (2007), Morales et al. (2009b), Irwin et al. (2009), Morales et al. (2009a), Carter et al. (2011), Irwin et al. (2011), Kraus et al. (2011), Doyle et al. (2011), Orosz et al. (2012a), Orosz et al. (2012b),

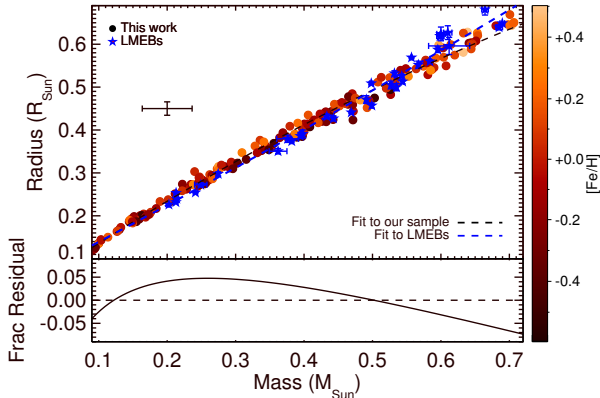


Figure 4. Mass–radius diagram for stars in our sample (red circles) and those from low-mass eclipsing binaries (LMEBs, blue stars). A typical error bar on our measurements is shown to the left. Stars in our sample are color-coded by their metallicity. The fit to both samples is shown as a dashed line. The bottom panel shows the fractional residual between these two fits. More details can be found in Section 5.2.

Helminiak et al. (2012), Bass et al. (2012), and Torres et al. (2014).

We fit the M_* - R_* relations for both our stars and the LMEBs with second order polynomials. We show the fractional difference between these fits in Figure 4. There is a notable discrepancy at the masses $M_* \gtrsim 0.65M_\odot$. Below $0.65M_\odot$ agreement is better than 5%. As we show in Section 8.4, model-inferred masses for our sample better reproduce the LMEB mass-luminosity relation across the sample. Thus the disagreement is most likely due to (expected) errors in the mass-luminosity relation from Delfosse et al. (2000), which was based on only 2-3 objects with masses in this range.

5.3. Temperatures and Bolometric Magnitudes Based on the Infrared Flux Method

Casagrande et al. (2008) extended the infrared flux method for FGK dwarfs from Casagrande et al. (2006) to M dwarfs with a method they called the multiple optical-infrared technique (MOITE). There are 19 stars in our sample with parameters from Casagrande et al. (2008). We found significant systematic differences between MOITE derived parameters and our values for these 16 stars, which we show in Figure 5. Our T_{eff} are on average 140 ± 24 K hotter, with increasing disparity at lower T_{eff} and higher metallicity. Our bolometric magnitudes are 0.020 ± 0.05 mag higher. For any individual star the difference in the bolometric magnitude is small, but taken together the systematic offset is significant. The MOITE values for T_{eff} and F_{bol} convert to θ values that were on average $8.1 \pm 1.5\%$ larger than ours.

IRFM and MOITE assume that a star can be approximated as a blackbody beyond $\simeq 2\mu\text{m}$. While this is reasonable for warmer stars, M dwarfs have significantly more flux in the NIR than predicted by a blackbody (Rajpurohit et al. 2013). Hence MOITE T_{eff} values tend to be systematically too low, with growing disparity at cooler temperatures where stars deviate more strongly from the Rayleigh-Jeans law. Our F_{bol} determinations also assumed a blackbody, but we only invoked this at $\lambda > 10\mu\text{m}$, where models suggest this is a safe assumption.

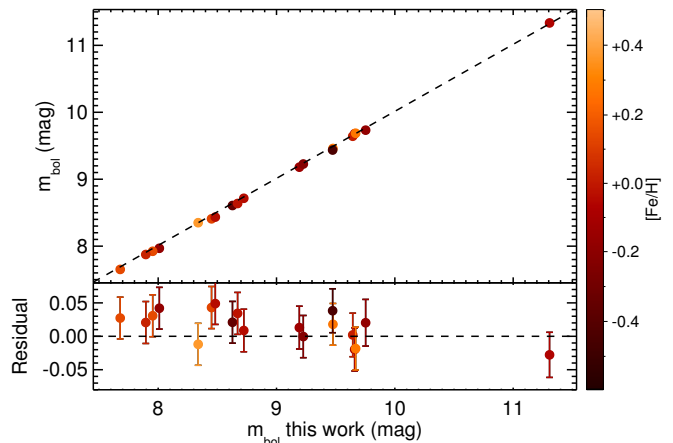
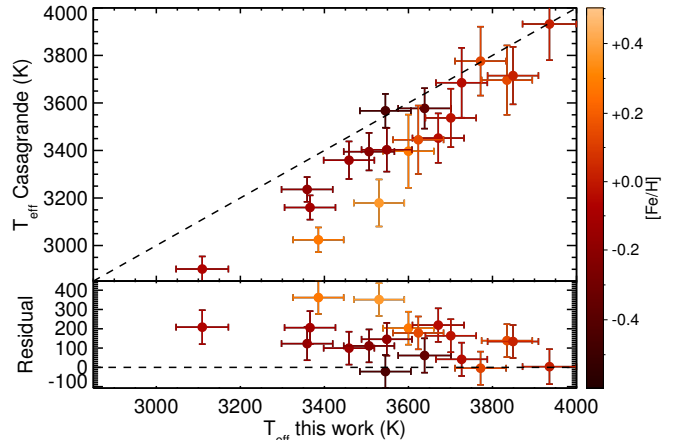


Figure 5. Comparison between T_{eff} (left) and m_{bol} (right) from this work to those derived in Casagrande et al. (2008). Dashed line indicates equality. The difference between the measurements is shown in the bottom panel of each figure. Points are color-coded by our metallicities. See Section 5.3 for more information.

Further, while this assumption could change our F_{bol} values, it has no effect on our T_{eff} determinations. MOITE also assumes that the PHOENIX model T_{eff} scale is accurate. While the more recent CIFIST version reproduces the T_{eff} scale from LBOI determinations, the older versions (i.e., the best available to Casagrande et al. (2008)) differ systematically from LBOI derived T_{eff} s (Mann et al. 2013b).

Casagrande et al. (2008) argued that MOITE is in agreement with LBOI determinations. However, this was based on just nine stars, many of which have since had their parameters revised by more precise LBOI measurements. Further, at least four of these stars have problematic 2MASS magnitudes (saturated or near saturated). Since MOITE depends on reliable infrared magnitudes, it could not be directly applied to these stars. We conclude that our T_{eff} and θ determinations are more reliable, and that the MOITE values are more likely systematically in error.

5.4. Metallicities and Temperatures from Rojas-Ayala et al. (2012) and Neves et al. (2014)

Gaidos & Mann (2014) compared the metallicities derived from our calibration (Mann et al. 2013a, 2014, based

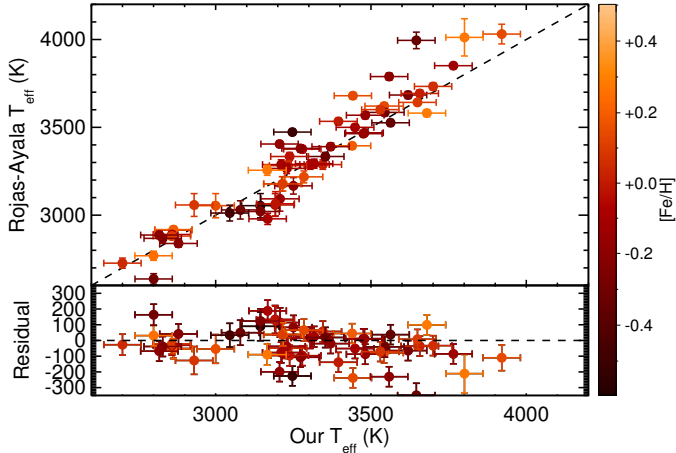


Figure 6. Comparison of T_{eff} from our analysis and T_{eff} from Rojas-Ayala et al. (2012) for the 59 overlapping stars. Points are color-coded by our metallicity determinations, although our $[\text{Fe}/\text{H}]$ values are consistent with those from Rojas-Ayala et al. (2012). Further details can be found in Section 5.4.

on NIR spectra) to those from Rojas-Ayala et al. (2012, also based on NIR spectra), Neves et al. (2013, based on absolute V, K magnitude), and Neves et al. (2014, based on high-resolution optical spectra). To summarize their findings, the mean metallicity differences are 0.03 ± 0.03 , 0.08 ± 0.02 , and 0.06 ± 0.02 dex, with χ^2_ν values of 0.23, 0.28, and 0.58, respectively. All of these methods used wide binaries to calibrate their metallicity measurements. The small systematic offset between our $[\text{Fe}/\text{H}]$ values and those from Neves et al. (2013) and Neves et al. (2014) may be a reflection of small systematic differences in the metallicities of the primaries of these calibrators (Hinkel et al. 2014). The low χ^2_ν values may be due to significant overlap in binary calibration samples, and/or overestimated errors for one or more method.

T_{eff} values from Neves et al. (2014) were calibrated using the Casagrande et al. (2008) T_{eff} scale, which we already discussed in Section 5.3 and found to be problematic. We compared our T_{eff} values to those from Rojas-Ayala et al. (2012) in Figure 6. Rojas-Ayala et al. (2012) estimated T_{eff} based on their measurement of $\text{H}_2\text{O-K2}$ index, which they interpolated onto BT-SETTL models. Because we also used BT-SETTL models the methods are not completely independent. However, Rojas-Ayala et al. (2012) used a different model grid (AGSS; with Asplund et al. (2009) relative abundances), and based their results on NIR instead of optical spectra, so this comparison is still illuminating. The mean difference is 28 ± 14 K, which is not significant, but there are some notable trends. Rojas-Ayala et al. (2012) appear to overestimate T_{eff} for the warmest stars. The χ^2_ν of the T_{eff} difference was 2.4, which is particularly high considering the methods are based on a similar set of models. Rojas-Ayala et al. (2012) estimated the errors in their T_{eff} values just from the measurement error in their derived $\text{H}_2\text{O-K2}$ values, and did not factor in errors in the models or shape errors in the spectra (Newton et al. 2014). These are exaggerated by the fact that changes in M dwarf T_{eff} s have a weaker effect on NIR spectra than optical. Hence errors from Rojas-Ayala et al. (2012) are probably underestimates.

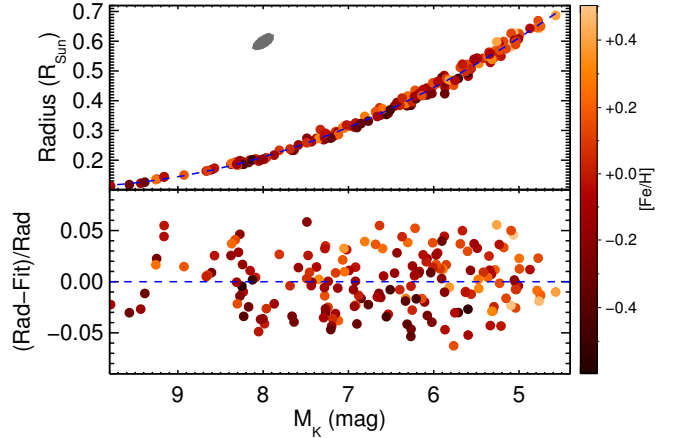


Figure 7. Top: R_* as a function of absolute K_S -band magnitude. The best-fit to the data is shown as a blue dashed line (see Equation 4 and Table 1). M_K and radius both depend on the distance, so the errors are correlated. Hence we show a one-sigma error ellipse in the top-left which indicates the typical 1σ errors for a typical point ($M_{K_S} \simeq 6.6$, $R_* \simeq 0.35$). Bottom: fractional residual to the fit. All points are color-coded by metallicity.

6. EMPIRICAL RELATIONS

We calculated empirical relations between observable (e.g., M_{K_S}) and intrinsic (e.g., R_*) stellar parameters. These relations are valid for $0.1R_\odot \lesssim R_* \lesssim 0.7R_\odot$ (spectral types K7–M7, $4.6 < M_{K_S} < 9.8$, $2700 < T_{\text{eff}} < 4100$ K), and $-0.6 < [\text{Fe}/\text{H}] < 0.5$. However, because of sample selection biases, the range of metallicities is significantly smaller for stars of spectral types later than M4 (mostly slightly metal-poor) and for the late-K dwarfs (mostly metal-rich). There are also only 15 stars in total with spectral types M5–M7 and only three stars with $[\text{Fe}/\text{H}] < -0.5$. These sample biases should be considered when applying these formulae.

For all relations we found the best-fit parameters of polynomial functions with the least-squares minimization algorithm *MPFIT* (Markwardt 2009). The number of parameters (polynomial order) was determined by an *F*-test; a probability of $> 95\%$ that the fit is an improvement is required to increase the fit order. Fits for R_* and M_* can be found in Table 1, for T_{eff} (from color) in Table 2, and bolometric corrections (BC) in Table 3.

6.1. Radius-Absolute Magnitude

In Figure 7 we show the relation between absolute K_S band magnitude (M_{K_S}) and R_* . We derived the best-fit of the form:

$$Y = a + bX + cX^2 + \dots, \quad (4)$$

where X is the absolute K band magnitude (M_{K_S}), Y is the stellar radius (R_*), and a , b , and c were parameters allowed to float to provide a better fit (reported in Table 1).

The fit yielded an RMS scatter of only 2.9%, which is remarkably tight given that typical errors in our radii were 3–4%. The scatter is low because errors in M_K and R_* are correlated in a direction similar to the trend (see the ellipse in Figure 7), a result in turn of both being driven largely by error in the distance. For example, imagine a star with a measured distance 4% closer than

the true value. The star’s derived radius will be 4% greater than the true value, but the M_{K_S} will also be $\simeq 0.1$ mag smaller (brighter). The result is that a 4% radius error corresponds to only a 1-2% deviation from the fit (the exact numbers depending on where the point is along the relation).

We perform a fit including $[\text{Fe}/\text{H}]$ as a second independent variable:

$$Y = (a + bX + cX^2 + \dots) \times (1 + f[\text{Fe}/\text{H}]), \quad (5)$$

where (as before) $Y = R_*$ and $X = M_{K_S}$. This particular functional form (multiplying by $1 + f[\text{Fe}/\text{H}]$ term) was used because linear changes in $[\text{Fe}/\text{H}]$ result in fractional changes in R_* . A simpler polynomial fit resulted in noticeable residuals at extreme values of R_* and $[\text{Fe}/\text{H}]$. The fit including $[\text{Fe}/\text{H}]$ produced a small but statistically significant improvement (based on an F test), with a resulting scatter of 2.7%. This relation is especially useful when trying to reduce systematic errors with metallicity, such as studying correlations between planet size and stellar metallicity.

We tested the absolute magnitude-radius relations for all SDSS and 2MASS magnitudes (*grizJHK_S*). We used the same formula (Equation 4) but the number of parameters was allowed set according to an F -test. K_S gave the smallest scatter (2.9%) and lowest χ^2_ν (0.93), although M_J and M_H performed similarly (3.4% and 3.2% scatter, and χ^2_ν of 1.1 and 1.3, respectively). The scatter and χ^2_ν grew as we used filters at bluer wavelengths because of the increasing effect of metallicity on the shape of the spectrum (Ségransan et al. 2003). This effect has been seen previously when fitting mass-luminosity relations (Delfosse et al. 2000), and even exploited to estimate metallicities of M dwarfs (e.g., Bonfils et al. 2005; Schlaufman & Laughlin 2010; Neves et al. 2012). It manifests in our data as a strong correlation between the luminosity-radius relation for optical colors and $[\text{Fe}/\text{H}]$, which we show in Figure 8.

6.2. Radius–Temperature

In Figure 9 we show stellar radius as a function of T_{eff} . Ignoring metallicity, we derived a fit of the same form as Equation 4, but with $X = T_{\text{eff}}/3500$ K. Values for the fitted variables are in Table 1. There is considerable scatter (13% in radius) in the relation and the fit has a χ^2_ν of 2.4, in part owing to significant correlation in the residuals with $[\text{Fe}/\text{H}]$. Accordingly, we derived a fit accounting for metallicity following Equation 5, again with $X = T_{\text{eff}}/3500$ K. Values for the fitted variables are in Table 1. The fit produced a scatter in R_* of 9%. Accounting for strong correlations between T_{eff} and R_* the χ^2_ν for Equation 5 was 1.10, suggesting that all of the scatter can be explained by measurement errors, and that the precision of this formula is limited primarily by errors in T_{eff} and $[\text{Fe}/\text{H}]$.

6.3. Color–Temperature

We used our synthetic magnitudes to construct colors and fit color- T_{eff} relations following the functional form of Equation 4, with $Y = T_{\text{eff}}/3500$ and X representing the relevant color. Figure 10 plots the relations for some of the colors that are most predictive of T_{eff} (based on the

standard deviation) and Table 2 reports the fit parameters. Readers are cautioned against using our empirical relations outside the color range of our sample where empirical fits show slope changes that are probably not real (See Figure 10). Additional color relations can be derived using the T_{eff} values in Table 5 and synthetic photometry provided in Table 6.

All relations show significant dependence on metallicity, and hence should be not be used on stars with metallicities far from solar. For cases where the target’s metallicity is known, we derive relations following the formula:

$$T_{\text{eff}} = a + bX + cX^2 + dX^3 + eX^4 + f([\text{Fe}/\text{H}]). \quad (6)$$

In the case that metallicity is not known, *JHK_S* colors can be used to approximate metallicity (Leggett 1992; Johnson et al. 2012; Mann et al. 2013a; Newton et al. 2014). Motivated by this, we tested different color combinations and found that the metallicity term could be best mitigated by including $J - H$ in the fit using the formula:

$$T_{\text{eff}} = a + bX + cX^2 + dX^2 + eX^3 + f(J - H) + g(J - H)^2. \quad (7)$$

Including $J - H$ color significantly reduced, but did not totally eliminate, the residuals with $[\text{Fe}/\text{H}]$. The scatter is notably smaller in T_{eff} when using $[\text{Fe}/\text{H}]$ then when using $J - H$ color, and therefore actual metallicities should be used over the single-color formulae if $[\text{Fe}/\text{H}]$ can be independently determined.

A comparison of spectroscopically derived T_{eff} vs. T_{eff} from Equation 7 is shown in Figure 11 and the coefficients are given in Table 2.

7. BOLOMETRIC CORRECTIONS

We calculated apparent bolometric magnitudes from our F_{bol} values using $m_\odot = -26.8167$ (Mamajek 2012; Pecaut & Mamajek 2013)¹². We then derived bolometric corrections for each filter for which we have synthetic magnitudes ($VR_C I_C grizJHK_S$ and *Gaia G*). We fit BCs with a second order polynomial in a color and performed these fits for all major passbands for which we have synthetic magnitudes ($VR_C I_C grizJHK_S$), using all possible color combinations. Relations using $V - J$ and $r - J$ colors exhibited the smallest standard deviations between fit and observed BC, and we show these for the most relevant passbands in Figures 12 and 13. Coefficients for the polynomial fits are given in Table 3. The scatter indicates that we can infer BC to 2 – 3% using just a $V - J$ or $r - J$ color.

All of the fit residuals show significant correlations with $[\text{Fe}/\text{H}]$. We derived additional relations useful for when the metallicity is known by adding an $e([\text{Fe}/\text{H}])$ term to the fits (given in Table 3). When metallicity is included it is possible to estimate BC within 1-3%. For cases where the metallicity of the star is not known, it is possible to mitigate these systematics by averaging over several corrections. For example, for BC_V , metal-rich stars land preferentially above the fit (larger BC), while for BC_J they land preferentially below (for both $V - J$ and $r - J$).

¹² see <http://sites.google.com/site/mamajeksstarnotes/bc-scale>.

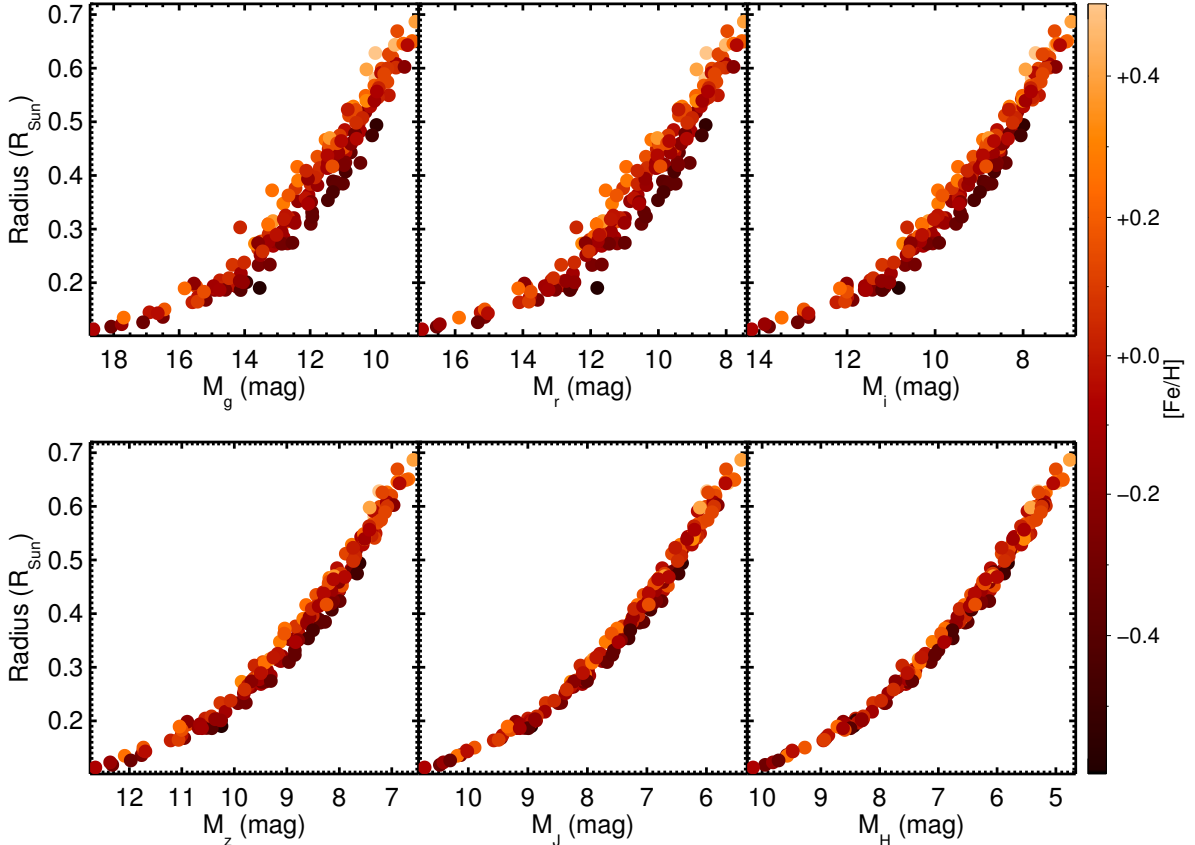


Figure 8. Relation between radius and absolute magnitude (for SDSS *griz* and 2MASS *JH* bands). The same relation for K_S is shown in Figure 7. All magnitudes are generated synthetically from our flux-calibrated spectra to match 2MASS *JH* and SDSS *griz* (Section 3.3). All Y-axis ranges are identical, but the X-axis ranges are different.

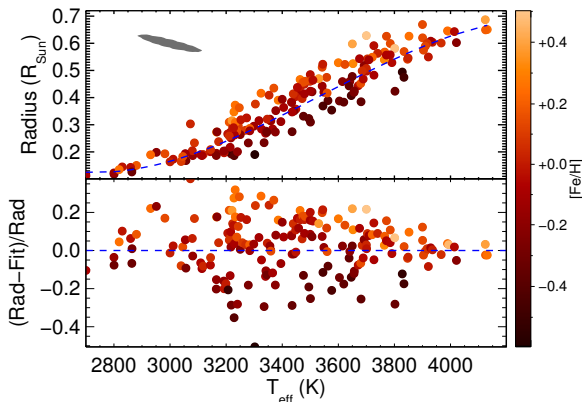


Figure 9. Top: R_* as a function of stellar T_{eff} . The derived R_* depends on T_{eff} (Equation 1) so the errors are strongly correlated. A typical error is shown as a gray ellipse in the top left of the plot. The best-fit ignoring $[\text{Fe}/\text{H}]$ (Equation 4) is shown as a dashed blue line. Bottom: residual from the best-fit. Points are colored according to their metallicity.

8. COMPARISON WITH PREDICTIONS OF A STELLAR EVOLUTION MODEL

Predictions from the Dartmouth stellar evolution models (Dotter et al. 2008; Feiden & Chaboyer 2012a, 2014a) were compared with the parameters measured or estimated in Section 4. Previous investigations have shown

that disagreements between model predictions and observations of low-mass stars are of similar magnitude among standard stellar evolution models that adopt appropriate physics for the physical conditions in these objects (e.g., Lyon, Dartmouth, Yale, Pisa, and Padova models; Feiden & Chaboyer 2012a; Boyajian et al. 2012b; Spada et al. 2013; Chen et al. 2014; Torres et al. 2014). Therefore, our results should be applicable to other model sets.

8.1. Model Physics & Grid Description

Models were computed using an updated version of the Dartmouth stellar evolution code (Dotter et al. 2008). The updates have been previously described (Feiden & Chaboyer 2013, 2014a; Muirhead et al. 2014), but here we summarize changes relevant to low-mass stars. First, nuclear reaction cross sections were updated to the recommended values from the Solar Fusion II review (Adelberger et al. 2011). This largely affects the cross section for the primary channel of the proton-proton chain, although nuclear reaction rates in low-mass stars are not significantly altered. Second, the specification of surface boundary conditions was moved deeper into the interior model to the location where the optical depth $\tau = 10$ to more accurately treat regions in low-mass stars where convection occurs in optically thin layers. Compare this with the formulation in Dotter et al. (2008) where surface boundary conditions are defined where $T = T_{\text{eff}}$, which leads to boundary conditions being specified in layers where

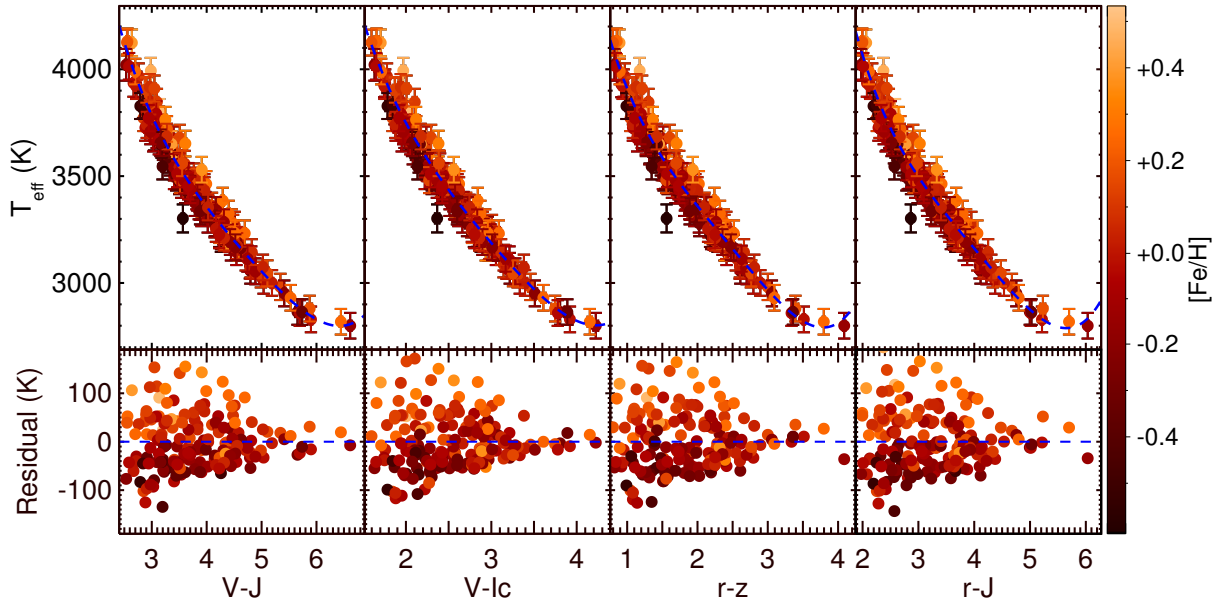


Figure 10. Spectroscopically derived T_{eff} as a function of different color combinations. The best-fit is overlotted as a blue dashed line. The bottom panels show the fit residuals. Fit coefficients are given in Table 2.

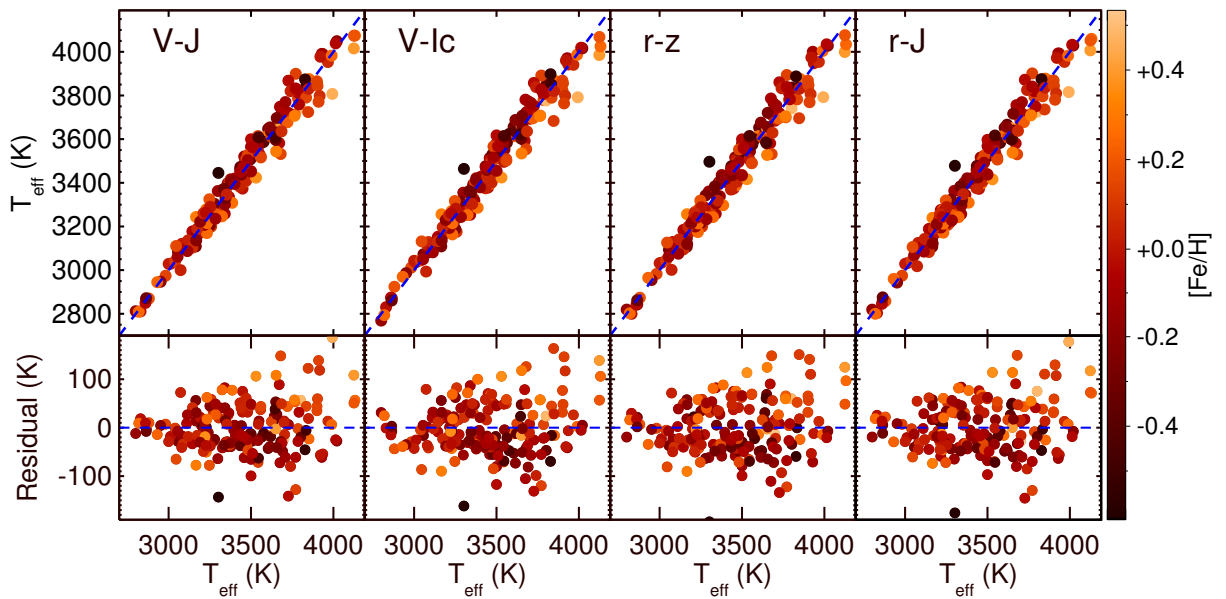


Figure 11. Spectroscopically derived T_{eff} vs. T_{eff} derived from the color marked in the top left of each pane and $J-H$ to correct for metallicity. The bottom panels show the best-fit residuals. Best-fit coefficients are given in Table 2.

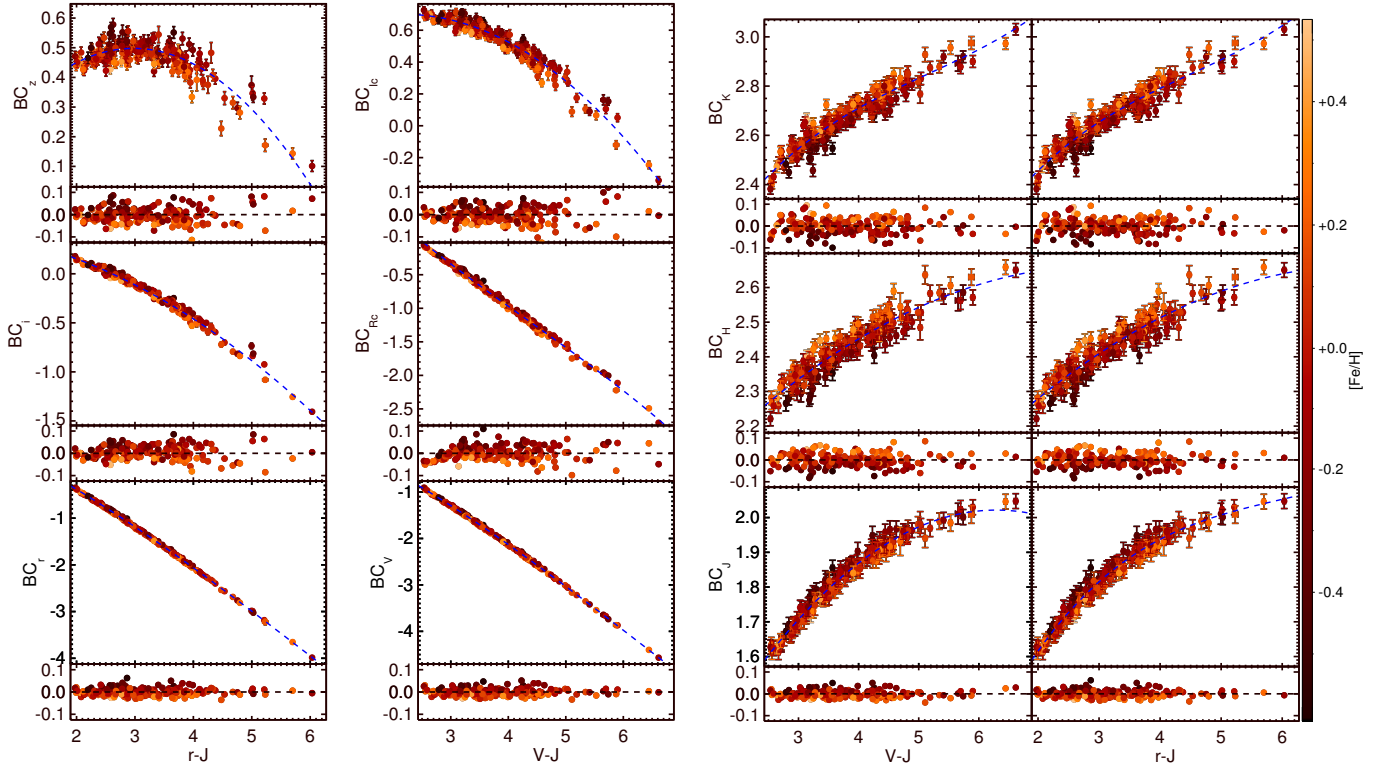


Figure 12. Bolometric corrections for SDSS (*riz*) passbands vs. $r - J$ (left), Johnson-Cousins VR_cI_C vs. $V - J$ (middle left), and 2MASS JHK_S vs. $V - J$ (middle right) and $r - J$ (right). Best-fits are plotted in blue (dashed line). Small panels below each of the relations show the residuals of the fit. Coefficients for each fit can be found in Table 3. Note that the scales for Y-axes in the residual plots are all the same. Points are color-coded according to metallicity. See Section 7 for more details.

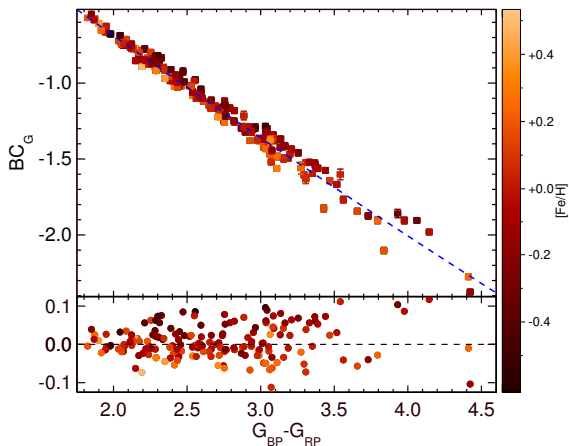


Figure 13. Same as Figure 12 but for the *Gaia* G passband vs. $G_{BP} - G_{RP}$ color.

$\tau \ll 1$. As described in Muirhead et al. (2014), moving the fit point to an optical depth $\tau = 10$ makes computations more reliable below $0.20 M_{\odot}$, but also causes all low-mass models to have hotter T_{eff} by up to 60 K. Model radii are not affected significantly by this update, meaning there is an increase in luminosity owing to the increase in T_{eff} . Finally, Feiden & Chaboyer (2014a) revised the grid of model atmospheres used to define surface boundary conditions to provide a finer sampling with metallicity. This was achieved by interpolating within the existing grid of model atmosphere structures, and

allows for greater accuracy when calculating models with metallicities between the values in the previous grid. Note that the models still adopt PHOENIX Next-Gen model atmospheres (Hauschildt et al. 1999) with the Grevesse & Sauval (1998) relative abundance pattern for the Sun.

A high resolution grid was constructed with the aforementioned models to permit more reliable interpolation of observed stellar properties. Specifically, models were computed with masses in the range of $0.10 - 0.80 M_{\odot}$ in steps of $0.02 M_{\odot}$ and metallicities in the range of -0.5 to $+0.5$ dex with spacing of 0.1 dex. The helium mass fraction was assumed to be linearly proportional to the heavy element mass fraction with slope $\Delta Y / \Delta Z \approx 1.6$ and y -intercept equal to the primordial helium abundance $Y_p = 0.2488$ (Peimbert et al. 2007), and assuming a solar-calibrated mixing length parameter ($\alpha_{\text{MLT}} = 1.884$). The influence of relaxing these assumptions is explored for a few characteristic systems in Section 8.5.

8.2. Stellar Parameter Estimation

Stellar model parameters were inferred using a Markov Chain Monte Carlo (MCMC) method implemented with *emcee* (Foreman-Mackey et al. 2013). The *emcee* package adopts an affine-invariant ensemble sampling algorithm (Goodman & Weare 2010) to evolve a set of random walkers that sample the posterior probability distribution (PPD) within the model grid parameter space. Our sampler explores the mass, age, metallicity, and distance PPDs to find an optimal fit to the observations (T_{eff} , F_{bol} , distance, metallicity) using model outputs (T_{eff} , lu-

minosity) and applying constraints from observations on observable parameters (metallicity, distance). The probability that a random model realization corresponds to the properties of a star in our sample is then evaluated using a likelihood function:

$$\mathcal{L}(\Theta; \mathbf{X}) = \prod_{n=1}^N \left(\frac{1}{2\pi\sigma_n^2} \right)^{1/2} \times \exp \left(-\beta \sum_{n=1}^N \left[\frac{\vartheta_n(\Theta) - X_n}{\sigma_n} \right]^2 \right), \quad (8)$$

where \mathbf{X} is a vector of length N containing the observed data (stellar T_{eff} and F_{bol}) and $\vartheta(\Theta)$ is a vector of model predictions for a given set of unknown parameters Θ , which contains both observable (e.g., metallicity, distance) and unobservable (e.g., mass, age) parameters. Prior information about the stellar metallicity and distance is known from our observations, allowing us to further constrain the PPD. We describe the prior probability distribution for those quantities assuming the true value is normally distributed about the observed value with a standard deviation equal to the formal error. Priors on mass and age are taken to be uniform over the range allowed by the definition of our model grid given in Section 8.

For each sample from the joint PPD, the corresponding set of model observables is obtained by linearly interpolating onto a 4D convex hull¹³ formed by the full grid of model parameters through Delaunay triangulation.¹⁴ We use the Quickhull algorithm for computing the convex hull (Barber et al. 1996), included in the SciPy interpolation package as the `LinearNDInterpolator` routine. We tested the accuracy of the interpolation routine by computing several 5 Gyr model isochrones using the 4D interpolation and then comparing it with 5 Gyr isochrones generated directly from the model mass tracks using cubic-spline interpolation. Results from the 4D interpolation were in agreement to better than 0.1%, except in the region between 0.14 and 0.18 M_{\odot} at higher metallicities, where there are gaps in the model grid due to convergence issues. In this region, the 4D interpolation was accurate to within 2%.

Parameters from the MCMC analysis were tested to ensure they were not biased by the specific MCMC algorithm. We compared results from a standard single-walker Metropolis–Hastings algorithm to results produced by `emcee` for a set of four well-characterized stars in different regions of the model grid parameter space. In all cases, the two approaches yielded identical results, with the exception that `emcee` produced larger estimates for the model uncertainties. This is most likely a consequence of any single-walker becoming stuck in local minima in the vicinity of the global minimum. This was supported by separate experiments on the single-walker MCMC, where

we varied the input parameters such as widths of Gaussian priors, the initial conditions, and the chain length. Most telling was that the use of a rudimentary simulated annealing produces errors more consistent with those of `emcee`. Different values of the factor β in Equation 8 were tested and found to not influence the results. Therefore, we adopted a single value $\beta = 1/2$. Finally, for `emcee`, we settled on using 400 walkers with 100 iterations. The ensemble sampler relaxes to a stable distribution after approximately 40 iterations. We discard the first 10 “burn in” steps of each walker, which are affected by the initial conditions. Otherwise, we do not reject any additional steps taken by the walkers.

Examples of the PPDs for four stars are shown in Figure 14, i.e., the same four stars whose spectra are shown in Figure 2. Recall that Gl 699 and Gl 876 are anticipated to be fully convective, while Gl 411 and Gl 880 are expected to possess a radiative core. Resulting metallicity PPDs are also roughly Gaussian, however, they exhibit sharp cutoffs at either the high or low metallicity end of the distribution, depending on the star’s metallicity. This is a consequence of the limits of the model grid, but does not appear to strongly affect the mass or distance PPDs. One can also see there is little dependence on stellar age for the best-fit model parameters describing these stars, although the age distribution for any given star appears to be mildly skewed toward older ages greater than about 8 Gyr.

8.3. Modeling Results

Stellar parameter values inferred from our comparison to the Dartmouth models are reported in Table 7. We were able to derive model parameters for 178 of 183 of the stars in our sample. Five of the stars have observed properties outside of the convex hull used for interpolation. PM I09437-1747 is too metal-poor for our model grid, while PM I02530+1652, GJ 1111, Gl 444 C, and Gl 412 B have T_{eff} s that are too cool for the model grid.

The overall quality of model fits are shown in Figure 15. Relative errors¹⁵ of the model-predicted T_{eff} s are plotted against the relative errors of the model-predicted F_{bol} . Errors are quoted in number of standard deviations from the observed mean value. There is broad agreement between the model and observed bolometric fluxes, with all stars formally fit within 1σ of their quoted observational errors. The average offset of model predictions from the observed F_{bol} values is $0.01 \pm 0.25\%$, with the distribution around the zero point being consistent with a normal distribution.

We find a significant correlation between the model–observed F_{bol} and the observed T_{eff} . Below about 3500 K, roughly where stars are expected to be fully convective, we find a small offset in the F_{bol} residuals at the 0.2% level with models systematically underestimating F_{bol} s compared to observations. However, above 3500 K, models increasingly overestimate F_{bol} by up to 0.4%. The offsets are insignificant for any given star, however a Spearman rank test indicates that a significant correlation with T_{eff} is present ($\rho = -0.65$ with $p \gg 10\sigma$). This could be the result of model inaccuracies or systematic errors in the observations. Our approximations of the spectrum

¹³ A convex hull for a set of points is defined as the smallest region in parameter space that contains the set of points within which any pair can be connected by a straight line segment without crossing the boundary of that region.

¹⁴ Given a set of points that have been triangulated, a Delaunay triangulation optimizes the minimum angle within the set of triangulations by ensuring that the circumcircle of each triangle contains no points from the original set within it.

¹⁵ by errors we mean difference between model and empirical determinations

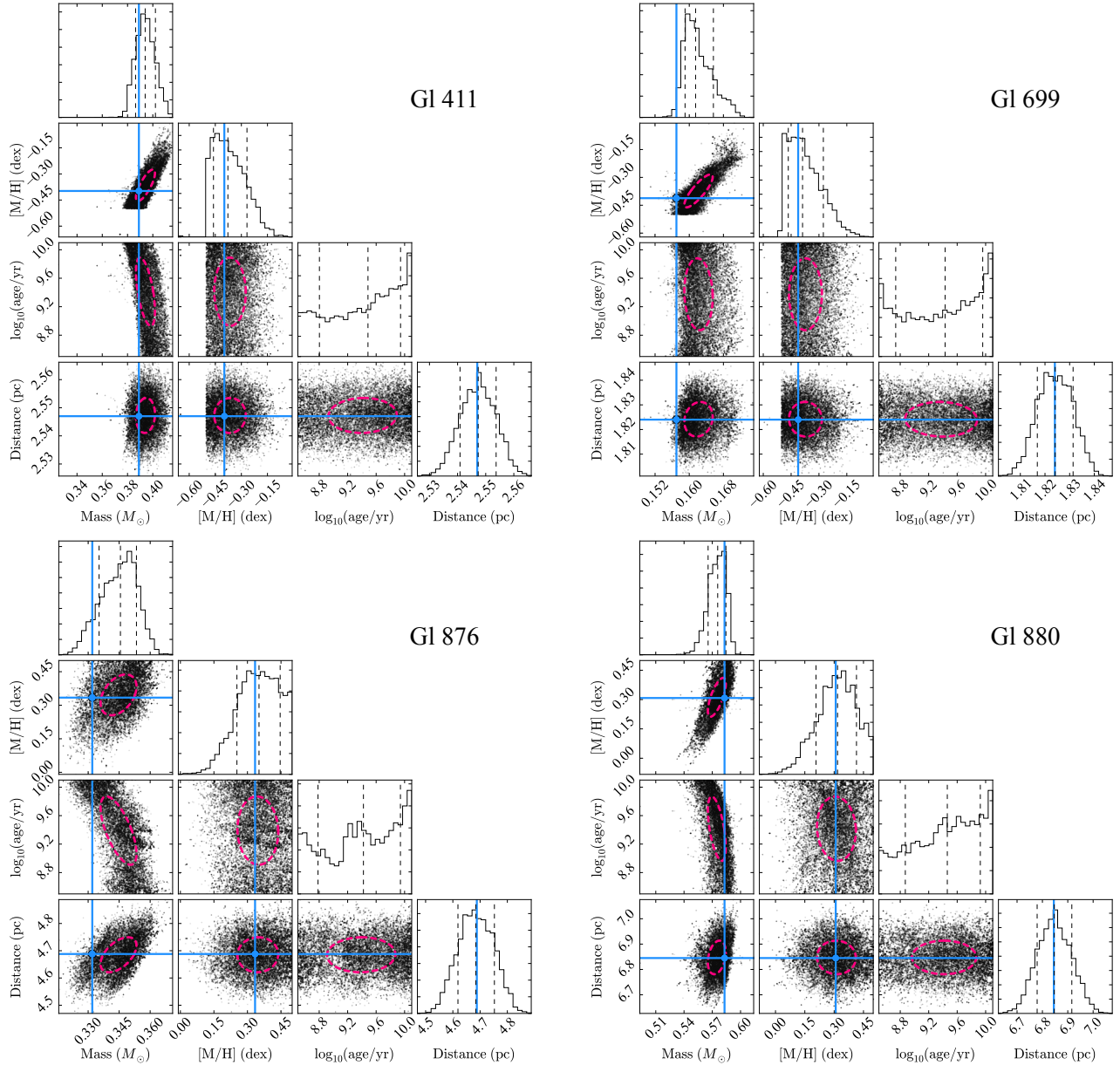


Figure 14. Mass, metallicity, age, and distance posterior probability distributions (PPDs) for Gl 411 (top, left), Gl 699 (top, right), Gl 876 (bottom, left), and Gl 880 (bottom, right). Vertical dashed lines define the 16th, 50th, and 84th quantiles of the distributions. Error ellipses are shown with pink dashed lines. Blue lines mark the observed value for the different quantities, except for the stellar age. Masses are derived from the Delfosse et al. (2000) empirical relation.

(e.g., use of models past $2.5\mu\text{m}$, detailed in Section 3.3) could create these small systematic errors, since the validity of these estimates changes with T_{eff} . However, the change in behavior is coincident with the onset of full convection, suggesting that small model inaccuracies are a more likely explanation.

There is a systematic bias in the models toward hotter temperatures (Figures 15, 16). Models systematically over-predict T_{eff} and under-predict R_* by an average of $-2.2 \pm 0.1\%$ and $+4.7 \pm 0.2\%$, respectively, echoing previous studies of EBs and single main sequence (MS) field stars (See Section 1). Note that small systematic uncertainties are likely present in the data (e.g., in the T_{eff} determination), so the standard errors quoted are likely underestimates. Comparison with LBOI determinations suggest systematic uncertainties of $\lesssim 0.3\%$ in T_{eff} and

$\lesssim 0.7\%$ in R_* in the empirical determinations, still well below the observed offset with models (7.2σ and 6.7σ , respectively). The distribution of T_{eff} differences is also non-Gaussian, with an excess of cases where models are discrepant. Out of the 177 stars successfully modeled, 72 (40%) match the observed T_{eff} within $\pm 1\sigma$, 79 (44%) within $\pm 1 - 2\sigma$, 24 (13%) within $\pm 2 - 3\sigma$, and 3 (2%) with discrepancies $> 3\sigma$.

Unlike F_{bol} disagreements, T_{eff} disagreements do not show any definite correlation with stellar properties, including F_{bol} , T_{eff} , and the inferred stellar mass (Figure 16). This is illustrated for the case of the inferred stellar mass in Figure 16. We also show in Figure 16 that radius disagreements do not exhibit any correlation with inferred stellar mass. With the exception of a few outliers below the fully convective boundary, there appears to be a floor

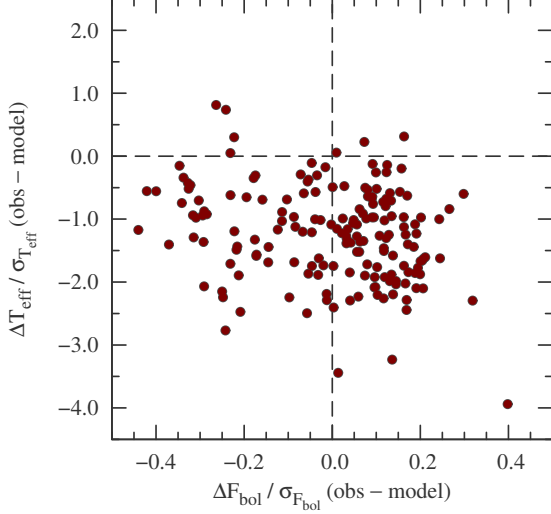


Figure 15. Luminosity and temperature residuals between observations and best-fit model predictions normalized to the observed 1σ observational uncertainties. Zero points are marked with dashed lines.

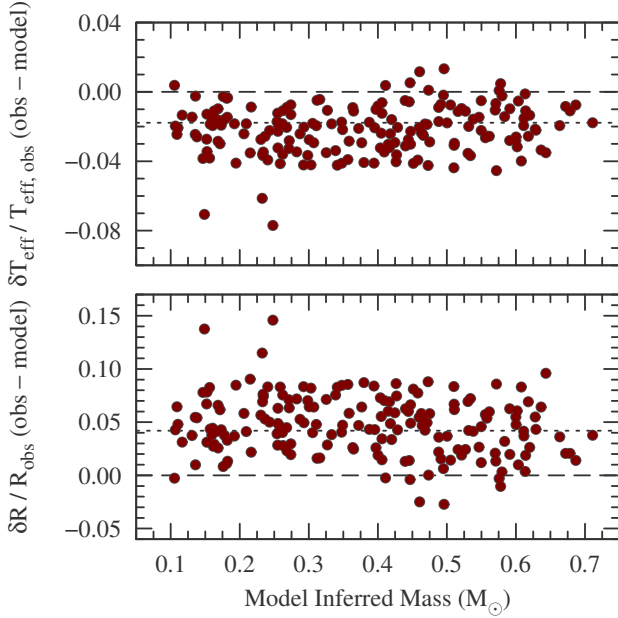


Figure 16. Relative model offsets for T_{eff} (top) and radius (bottom) predictions as a function of the inferred stellar mass. Typical 1σ observational uncertainties are given by dotted lines.

in the observed T_{eff} errors of -4% and a ceiling in the radius errors of $+10\%$. Three exceptions lying beyond the error floor/ceiling are PM I10430-0912, Gl 896 B (EQ Peg B), and Gl 166 C (40 Eri C).

Figure 17 show that neither relative errors in T_{eff} nor R_* show a dependence on the observed metallicity, even when the sample is split into the partially convective and fully convective regimes. The division between partially and fully convective interiors was taken to be $M_* \geq 0.37 M_\odot$ and $M_* \leq 0.33 M_\odot$, respectively, thereby excluding stars whose convective state is uncertain. A linear regression analysis suggests that relative errors in T_{eff} are not correlated with metallicity, with slopes of 0.7% error/dex and -0.2% error/dex for the partially convective and fully convective populations, respectively. The lack of a correlation is confirmed with Spearman ρ , Pearson r ,

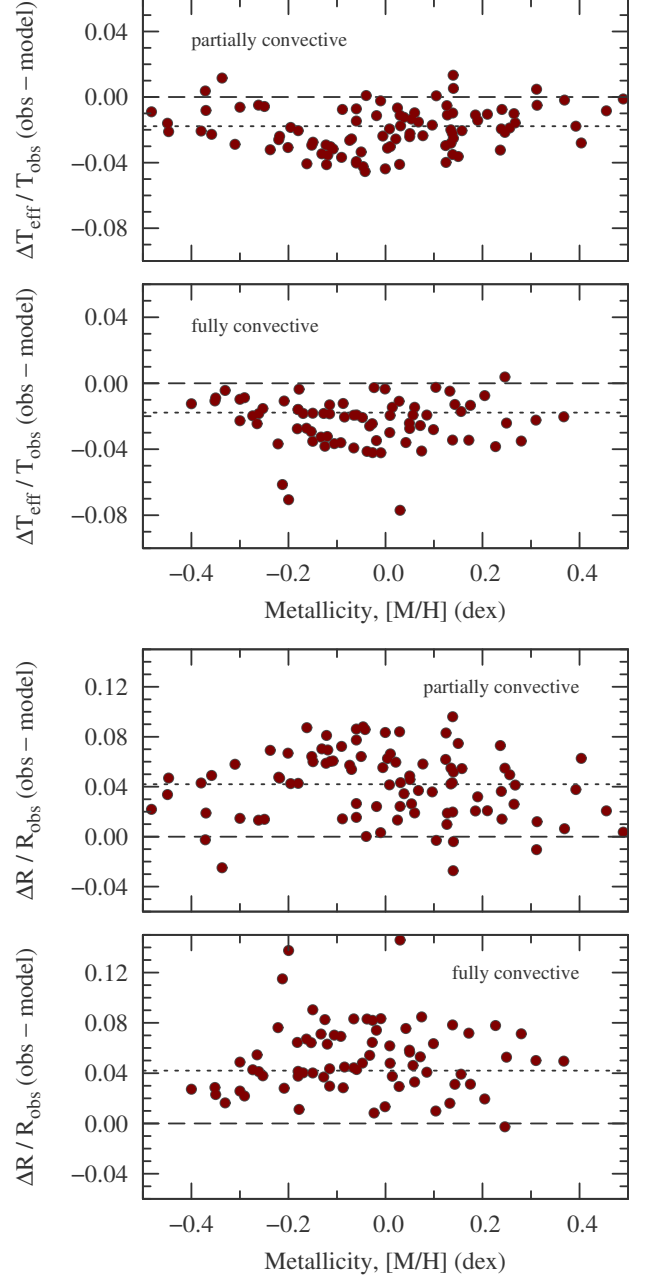


Figure 17. Relative model errors for T_{eff} (left) and radius (right) predictions as a function of the observed metallicity. The sample is split into partially convective stars with a radiative core (top panels) and fully convective stars (bottom panels). Distance between the dashed and dotted line is the median 1σ uncertainty, between which models can be assumed to adequately reproduce the observation of a given star.

and Kendall's τ correlation tests returning results entirely consistent with the null hypothesis.

Plotting model errors against the measured EW of $H\alpha$ for each star also reveals no significant correlations (Figure 18), where we again split the population of stars into partially and fully convective subsets. There are only two partially convective stars with measured $H\alpha$ EWs larger than 0.5 \AA . While they show significant disagreement with models, comparable differences are seen in stars that do not show elevated levels of $H\alpha$ emission. Model errors in the fully convective regime also appear to be independent of $H\alpha$ EW. Fully convective stars appear systematically

larger and cooler, regardless of the EW of $H\alpha$. As with metallicity, different correlation tests all return results that are consistent with the null hypothesis when considering radius and T_{eff} errors as a function of $H\alpha$ EW, with $p \gtrsim 0.20$. Combining the two populations also reveals no significant trend between T_{eff} and $H\alpha$ EW, with Pearson $r = -0.119$ ($p = 0.112$), Spearman $\rho = -0.165$ ($p = 0.027$), and Kendall's $\tau = -0.134$ ($p = 0.008$). Notably, we were able to generate a rank coefficient of an equivalent value for each correlation test by randomly perturbing temperature errors by their quoted uncertainties, suggesting that the observed weak correlations are due to random noise in the measurements.

$H\alpha$ equivalent width alone is not the most accurate measure of chromospheric emission. A more robust indicator is the ratio of the $H\alpha$ luminosity to the total bolometric luminosity of the star ($L_{H\alpha}/L_{\text{bol}}$). Following Tinney & Reid (1998), $L_{H\alpha}/L_{\text{bol}}$ can be computed using:

$$\frac{L_{H\alpha}}{L_{\text{bol}}} = \frac{F_{H\alpha}}{F_{\text{bol}}} = \frac{EW \times S_c}{F_{\text{bol}}}, \quad (9)$$

where S_c is the local continuum flux density. The quantity S_c/F_{bol} is simply a bolometric correction. We derived S_c/F_{bol} as a function of T_{eff} and $[\text{Fe}/\text{H}]$ as was done in Section 7, but using only stars with no detectable $H\alpha$ ($EW \leq 0.27$, $< 1\sigma$ above 0). For this we defined the band of interest as a region spanning 6500\AA – 6600\AA . Our results did not change significantly by making small ($\sim 20\text{\AA}$) adjustments to the width of the region. We then applied the empirical relation to calculate S_c/F_{bol} and $L_{H\alpha}/L_{\text{bol}}$ (as well as its logarithm, $[L_{H\alpha}/L_{\text{bol}}]$) for all stars in the sample. The resulting $[L_{H\alpha}/L_{\text{bol}}]$ values are relatively consistent with those derived from Stassun et al. (K. Stassun, 2015 private communication; 2012) for stars with $T_{\text{eff}} > 3000$ K.

Our current observations are insensitive to small $H\alpha$ values, as poor resolution combined with strong (unresolved) molecular bands and observational uncertainties are capable of mimicking or masking weak ($H\alpha \lesssim 0.8$) values (Gaidos et al. 2014), diluting the result. For these stars we set $[L_{H\alpha}/L_{\text{bol}}]$ to a quiescent value of 10^{-6} , although the result does not change for any reasonable assignment for the quiet stars, or even simply leaving them unadjusted and removing negative $L_{H\alpha}/L_{\text{bol}}$ values.

We find no significant correlation among the data when comparing T_{eff} and radius errors to $[L_{H\alpha}/L_{\text{bol}}]$. Without accounting for uncertainties in the T_{eff} values, we find Pearson $r = -0.216$ ($p = 0.004$), Spearman $\rho = -0.172$ ($p = 0.023$), and Kendall's $\tau = -0.136$ ($p = 0.007$), suggesting a weak correlation is present. Correlation coefficients of similar magnitude, but opposite in sign, and of similar statistical significance were found when considering radius. To account for measurement uncertainties, we followed the same procedure as with $H\alpha$ EWs; we randomly perturbed each T_{eff} by their quoted uncertainties and performed correlation tests on each random realization of the data set. This was performed 1000 times and compared to a similar data set where T_{eff} errors were perturbed, but then assigned a value of $[L_{H\alpha}/L_{\text{bol}}]$ from the data set at random. We find that including uncertainties on the T_{eff} errors produces mean correlation coefficients for the real data set that are entirely consistent with those of the randomly generated data set to within 1.7σ (i.e.,

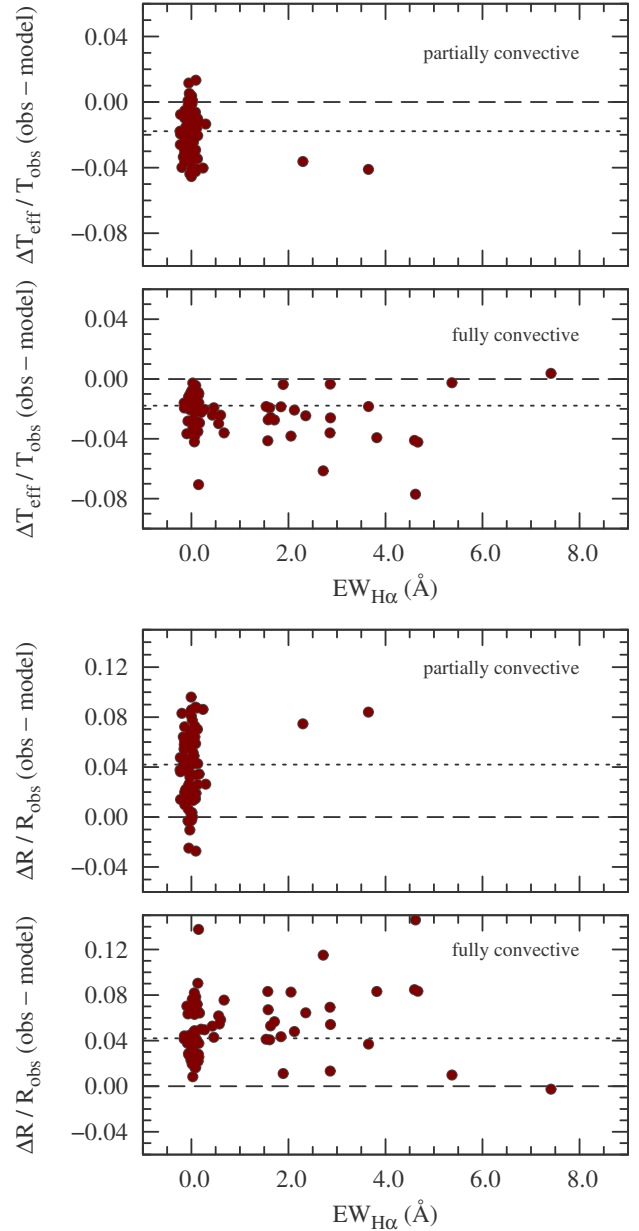


Figure 18. Relative model errors for T_{eff} (left) and radius (right) predictions vs. the equivalent width of the $H\alpha$ line. The sample is split into partially convective stars with a radiative core (top panels) and fully convective stars (bottom panels). Distance between the dashed and dotted line is the median 1σ uncertainty, between which models can be assumed to adequately reproduce the observations of a given star.

$p \geq 0.09$).

X-ray emission is also a proxy for stellar magnetic activity. We cross-referenced our M dwarf sample with the ROSAT All Sky Survey Bright and Faint Source Catalogues (Voges et al. 1999, 2000). X-ray count rates and hardness ratios were converted to X-ray fluxes, F_X , following Schmitt et al. (1995). As with $H\alpha$ EW, model errors show no dependence on F_X/F_{bol} . Finally, we also cross-referenced our sample with the source catalog from the Galaxy Evolution Explorer (GALEX) All-sky Survey (Martin et al. 2005) and extracted near-ultraviolet (NUV) and far-UV (FUV) fluxes. Modeling errors show no correlation with NUV or FUV fluxes. We are therefore

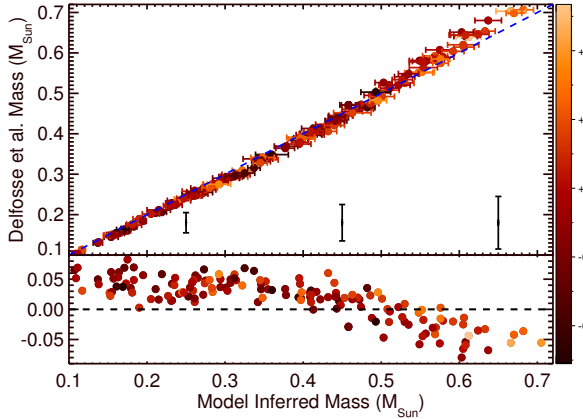


Figure 19. Mass derived from the empirical mass- M_K relation from Delfosse et al. (2000) vs. of the mass inferred from the models (Section 8.3). We show some characteristic errors for Delfosse et al. (2000) masses at the bottom of the panel. The bottom pane shows the fractional mass difference. Points are color-coded by metallicity.

confident that variation in magnetic activity plays no significant role in driving the systematic offset between model predictions and observations of stellar properties.

Even if the proposed correlation is real (despite insignificant p -values for a variety of metrics) it must be a relatively weak effect. The linear slope of the relation between radius and temperature errors (difference between model and observed values) and $[L_{H\alpha}/L_{bol}]$ is $\sim -0.46\%$ error/dex in T_{eff} and 0.84% error/dex in R_* , in contrast to slopes of -4.7% error/dex and 15.4% error/dex found by Stassun et al. (2012).

8.4. Semi-empirical M_{K_S} -Mass Relation

In Section 5.2 we found that our empirical radii combined with masses from the Delfosse et al. (2000) relation could reproduce the mass-radius relation from LMEBs within quoted uncertainties, but there were noticeable systematics (Figure 4). As we show in Figure 19, similar systematics are seen when we compare model-based masses to those from Delfosse et al. (2000). The model and empirical mass determinations agree given the estimated 10% errors on the Delfosse et al. (2000) relation, however the models predict systematically lower masses above $0.50 M_{\odot}$ and systematically higher masses below that threshold. This disagreement cannot be explained by the offsets in F_{bol} and T_{eff} noted in Section 8.3. Slightly lower model masses (T_{eff}) would be needed to produce lower F_{bol} values, which would accentuate the deviations between the model masses and empirically derived masses at the high mass end in Figure 19, albeit slightly.

The consistency between the offsets seen in Figure 19 and those in Figure 4 suggests that the model-derived masses are equally or more reliable, and significantly more precise than those from the Delfosse et al. (2000) relation. Motivated by this, we constructed a luminosity (M_{K_S})-mass relation using masses derived from stellar models and observed absolute K_S -band luminosities. A fourth-order polynomial, i.e.,

$$M_*/M_{\odot} = a + b \cdot M_{K_S} + c \cdot M_{K_S}^2 + d \cdot M_{K_S}^3 + e \cdot M_{K_S}^4 \quad (10)$$

was required to obtain a reasonable fit to the data. Best-fit coefficients are reported in Table 1. Uncertainties were calculated using maximum likelihood through a MCMC

method implemented with `emcee`. We used 500 walkers and 100 steps with random seed parameters for each coefficient normally distributed around the solution derived from a least-squares regression. For each walker and each step in the MCMC analysis, the adopted set of M_{K_S} -mass pairs were a random realization of the set of mean values, allowing individual points to be shifted within their quoted uncertainties. Parameters listed in Table 1 represent the mean value of the PPD from the final step of each walker, although the final values were independent of the number of steps adopted while sampling the PPD.

The best-fit polynomial is plotted in Figure 20. We plot the computed relation for each sample of the joint PPD of the fit coefficients in the domain $M_{K_S} \in [4.5, 9.5)$. Our relation compares well to that from Delfosse et al. (2000), with the most significant deviations between the two occurring in the mid- M_{K_S} and bright- M_{K_S} regions. We note that the scatter around our relation is significantly smaller than the canonical 10% scatter in the Delfosse et al. (2000) relation. The mean absolute error of the data about the relation, shown in the bottom panel of Figure 20, is 1.4%, while the standard deviation of the errors about the zero point is about 1.8%. About two-thirds (69%) of the data have residuals within $\pm 1.8\%$, whereas 95% are located within $\pm 3.6\%$ of the zero point. The residuals show no correlation with metallicity. There appears to be a systematic offset of the data from the fit around $M_{K_S} = 8.25$, which results from interpolation errors around $0.16 M_{\odot}$ that were mentioned previously. This also causes the fit to systematically overestimate masses in the range $8.0 > M_{K_S} > 7.5$. The fit has a nominal $\chi^2_{\nu} = 0.37$, suggesting uncertainties may be overestimated. This can be partially attributed to the fact that mass and M_{K_S} uncertainties are treated independently, though in reality they are correlated along the observed relationship.

We also compare the semi-empirical mass-radius relation for our sample to the mass-radius relation defined by LMEBs in Figure 21. We see that the two estimates compare well in the bottom panel of Figure 21, where we show the relative uncertainty between our semi-empirical fit and a polynomial fit to the LMEB sample. Between 0.2 and $0.7 M_{\odot}$, the maximum deviation between the two fits is $\simeq 4\%$ and the largest deviation occurs in a region where there are no LMEB systems to constrain the LMEB polynomial fit. In addition, the polynomial fit from the LMEB sample provides a $\chi^2_{\nu} = 0.9$ with respect to the data from our single star sample. This provides support to the validity of our derived masses and our semi-empirical mass- M_{K_S} relation.

8.5. Sensitivity to Standard Model Parameter Values

Given that model-observation disagreements appear to not be strongly correlated with either metallicity or magnetic activity indicators, we briefly explore how adopted model physics affect the location of the data in Figure 15 and the results that may have for the inferred stellar masses. Specifically, we address the impact of the adopted solar composition, helium mass fraction, convective mixing length parameter, and radiative opacities on the results for the four representative systems we identified in Section 8.2. Results of these investigations are given in Table 4 and are shown in Figure 22 as the set of displacement vectors in an HR diagram.

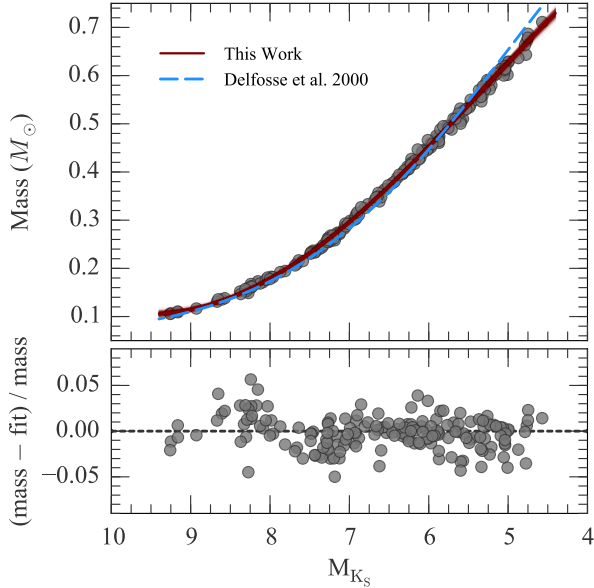


Figure 20. (Top) Mass–luminosity (M_{K_S}) relationship. M_{K_S} was determined from observations and paired with masses inferred from the Dartmouth stellar evolution model (Section 8.3). Red, solid lines are 500 random realizations of quartic polynomial fits to the data drawn from the joint PPD for the polynomial coefficients. The Delfosse et al. (2000) relationship is shown for reference (blue, dashed line). (Bottom) Residuals of the data with respect to a best-fit quartic polynomial whose coefficient values listed in Table 1.

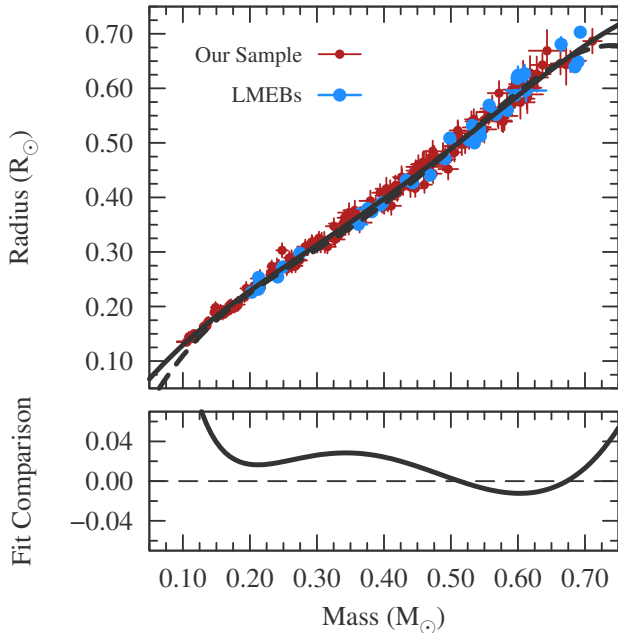


Figure 21. (Top) Mass–radius distribution from our bolometric radii and model-inferred masses compared to the distribution from LMEBs. Similar to Figure 4, but using model-inferred masses instead of those from the empirical mass–luminosity relation of Delfosse et al. (2000). Polynomial fits to the two distributions are shown as solid and dashed lines for our sample and the LMEB sample, respectively. (Bottom) Relative error between the polynomial fits.

Models of four stars are chosen for individual comparison: GJ 411, GJ 699, GJ 876, and GJ 880, the same four representative stars from Figure 2. They occupy different regions of parameter space that may lead to changes

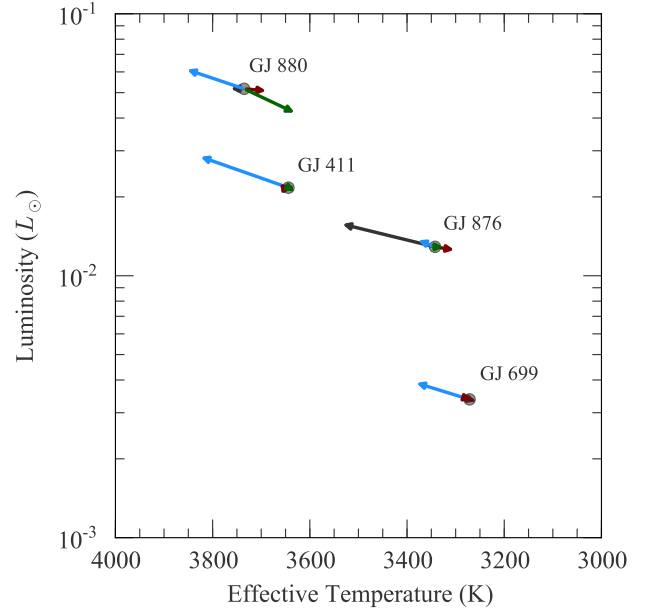


Figure 22. HR diagram showing location of best-fit stellar models (gray points) of four representative stars: GJ 411, GJ 699, GJ 876, GJ 880. Vectors point to the location of test model results for the same stars computed with the Asplund et al. (2009) solar composition (gray), helium enhanced composition with $Y = 0.33$ (blue), reduced convective mixing length parameter $\alpha_{\text{MLT}} = 1.0$ (red), and artificially increased radiative opacities (green).

in the adopted physics having different effects on the model predictions. Two stars are fully convective (GJ 699, GJ 876) and two partially convective (GJ 411, GJ 880). At the same time, two are at the metal-poor end of the spectrum in this study (GJ 411, GJ 699) and two are more metal-rich (GJ 876, GJ 880). All test models below are computed at the precise model-inferred mass from Section 8.3 and with the exact observationally determined metallicity. Differences between test models (see below) and the standard, unaltered model are taken at 5 Gyr.

8.5.1. Solar Composition

The set of absolute abundances of heavy elements in the Sun is an important parameter of stellar evolution models, and there is considerable debate as to the correct values. Stellar abundance analyses performed with sophisticated 3D radiation–hydrodynamic simulations and using the latest atomic and molecular line lists find that the abundance of heavy elements is $Z \approx 0.013 - 0.016$, with a surface $(Z/X)_{\odot} \approx 0.018 - 0.020$ (e.g., Asplund et al. 2009; Caffau et al. 2011). This is well below the solar heavy element abundance distribution adopted in our stellar evolution models, which are taken from the solar abundance study by Grevesse & Sauval (1998), who found $Z \approx 0.017$ and $(Z/X)_{\odot} = 0.023$. However, it is well documented that revised solar heavy element abundances, when included in standard solar models, yield disagreements with the sound speed profile in the solar convective envelope, the lower boundary of solar convection zone inferred from helioseismic inversions, and with the solar surface helium abundance (e.g., Bahcall et al. 2005; Delahaye & Pinsonneault 2006; Basu & Antia 2008). Nevertheless, we test the impact on low-mass star predictions if the solar heavy element abundances are lower.

We adopt the Asplund et al. (2009) solar composition and consistently modify all of the model input physics. The Asplund et al. (2009) composition was adopted for two reasons: (1) it represents the largest shift away from Grevesse & Sauval (1998) among the recent values, and (2) more complete grids of PHOENIX model atmospheres and low temperature opacities exist for the Asplund et al. (2009) mixture. High and low temperature opacities were calculated at the specified solar abundance (Iglesias & Rogers 1996; Ferguson et al. 2005), and new surface boundary condition tables were compiled from PHOENIX BT-Settl model atmosphere structures at a depth of $\tau = 10$ (Allard et al. 2011). Surface boundary conditions were computed with the same grid resolution as our standard models (0.1 dex) using the same interpolation procedures. The distribution of heavy elements in FreeEOS was also updated, for consistency in the computation of the EOS. A new solar calibration was run to identify the appropriate starting conditions for our test models.

Recalibration of the solar model mostly suppresses the influence of changing absolute solar abundances by adjusting other unconstrained model parameters. We see in Figure 22 that changing absolute solar abundances has little effect on the properties of the test models, with the exception of Gl 876. Decreasing the solar metal abundance leads to a decrease in the overall radiative opacity. Onset of nuclear fusion in the core is not affected by the change in opacity. Pre-MS stars transport energy released during gravitational contraction through near-adiabatic convection, and thus the core temperature is largely governed by an adiabatic temperature stratification. However, once fusion begins, the development of a radiative core is directly affected by the radiative opacity, with a lower opacity causing the radiative core to develop more quickly. Lower opacities lead to hotter temperatures and higher densities in the stellar core, which hastens the equilibration of the p - p chain due to a faster build up of ^3He . This halts the stars contraction earlier, leaving it with a larger radius, hotter T_{eff} , and higher luminosity at the zero-age MS. Evolutionary effects then come into play as the star evolves along the MS. Since we require a $1.0 M_{\odot}$ model to reproduce the luminosity and radius of the Sun at the solar age, the solar-calibrated helium abundance and convective mixing length are adjusted to offset changes imparted by lower radiative opacities. In this case, the helium abundance is decreased and the convective mixing length parameter (α_{MLT}) is increased. Helium reduction causes the star to have a lower luminosity, while increasing α_{MLT} shrinks the envelope convection zone, making the star smaller and hotter. By design, effects due to all three of these changes cancel in models of the Sun. At lower masses, stars react in different ways to variations in these three quantities, but overall, negligible changes are imparted to the models.

The sensitivity of Gl 876 to the solar abundance probably erroneous and not representative of the expected changes. Instead, we suspect the increased T_{eff} and luminosity are due to an inaccuracy in the PHOENIX model atmosphere structures at the highest metallicities for stellar parameters of $T_{\text{eff}} \sim 3600$ K at $\log g = 3.5$, precisely the parameter regime occupied by Gl 876 while it is undergoing pre-MS contraction. Specifically, there is a sharp discontinuity in gas temperature at $\tau = 10$ as a function of T_{eff} . The abruptness is indicative of a numerical error,

as a physical change of the model atmospheres at high metallicity would likely create a smoother transition. The resulting atmosphere structures appear to be approximately 250 K hotter at this optical depth than expected from an extrapolation of model atmosphere properties at lower metallicities. An offset of 250 K is very nearly the temperature offset endured by our model of Gl 876. Such an offset ultimately leads to the model arriving on the MS earlier than expected and at a hotter T_{eff} . Therefore, we conclude that the test model of Gl 876 is in error.

8.5.2. Helium Abundance

We test the sensitivity to the model assumption that helium abundance scales linearly with metal abundance by artificially increasing the initial helium abundance to $Y_i = 0.33$. Models were generated with constant Z_i and constant (Z/X). In both cases, increasing the helium abundance moves all models toward higher luminosities, hotter T_{eff} , and larger radii, as shown in Figure 22. We also see in Table 4 that each quantity is positively correlated with Y . This can be understood in terms of helium’s effect on the mean molecular weight. Increasing the amount of helium increases the mean molecular weight, which in turn causes the central temperature to rise, leading to a higher nuclear energy generation rate. While this primarily affects T_{eff} and luminosity, it also causes the model to arrive on the MS at an earlier time with a larger radius compared to the standard case.

As a result, mass estimates from model fits would be lower by about 7% and 3% per 0.05 dex increase in Y for stars above and below the fully convective boundary, respectively. However, model T_{eff} s at these lower masses would increase by approximately 3% and 1% over the T_{eff} s derived assuming a standard linear relation between Y and Z . Fitted model radii, on the other hand, would decrease by about 4% and 1%, for partially and fully convective stars, respectively. Therefore, to provide better agreement between models and observations at constant luminosity and metallicity, the assumed helium abundance needs to be decreased. To match the systematic offsets seen in Figure 16, we estimate that helium abundance needs to be systematically decreased by $\Delta Y \approx 0.03 - 0.04$ dex at constant metallicity. Some stars would therefore have helium abundances at or below the primordial helium abundance (Peimbert et al. 2007), which is typically understood to be unrealistic, although not necessarily precluded by observations.

8.5.3. Convective Mixing Length Parameter

Reducing the convective mixing length parameter is akin to suggesting that convective energy transport is less efficient. It has long been noted that models of low-mass M-dwarfs require a convective mixing length below the solar-calibrated value (e.g., Cox et al. 1981; Chabrier & Baraffe 1997). Recent evidence from asteroseismology of more solar-like stars suggests that required convective mixing length values correlate with intrinsic stellar properties (T_{eff} , $\log g$, metallicity; Bonaca et al. 2012).

Vectors shown in Figure 22 were calculated for a set of models with a convective mixing length parameter $\alpha_{\text{MLT}} = 1$, as compared to the solar-calibrated value of $\alpha_{\text{MLT}} = 1.88$. This leads to models with shallower convective envelopes and a more extensive radiative interior, causing a reduction in model surface T_{eff} s, an increase in predicted

stellar radii, and a slight decrease in the luminosity. Note that the effects are mass dependent, with higher mass stars being relatively more affected than lower-mass stars. Table 4 illuminates this mass dependence, particularly the dependence of the rate of change of T_{eff} with α_{MLT} . The mass dependence is a consequence of the extent of the super-adiabatic layers in the atmosphere and the degree to which they are super-adiabatic. Lower mass stars are more dense and therefore largely undergo near-adiabatic convection with convective properties being fairly insensitive to the choice of input parameters, as compared to higher mass stars, at least within the context of mixing length theory.

Mass estimates are not overly sensitive to variations in the convective mixing length, owing to the fact that the convective mixing length does not affect the stellar luminosity at a significant level. At the high-mass end of our sample, reduction of the convective mixing length from solar $\alpha_{\text{MLT}} = 1.88$ to $\alpha_{\text{MLT}} = 1$ yields models with T_{eff} s that are 1.5% cooler and radii about 1% larger. The mixing length parameter would need to be further reduced to provide agreement at the lower end of the MS where stars are fully convective. Tests models with $\alpha_{\text{MLT}} = 0.5$ indicate that such a reduction largely affects model T_{eff} s and luminosities, owing to the direct coupling between the stellar surface and the core. Mass estimates are affected at the 3% level at $0.30 M_{\odot}$, with T_{eff} reductions of about 2% and radius increases of around 2.5%. We can therefore conclude that α_{MLT} needs to be continually reduced towards lower masses, with $\alpha_{\text{MLT}} \sim 1$ at $0.5 M_{\odot}$ and ~ 0.5 at $0.3 M_{\odot}$. These reductions would provide general agreement between model T_{eff} and observations. However, model radii are still under-predicted by several percent.

8.5.4. Radiative Opacity

We previously mentioned (Section 8.5.1) the effect that radiative opacities have on stellar structure. To isolate the specific effects of the radiative opacity, test models were computed with the Rossland mean opacity κ increased by 50%, such that $\kappa = 1.5\kappa_0$, where κ_0 is the Rossland mean opacity in our standard models with a Grevesse & Sauval (1998) solar abundance distribution. Increasing the radiative opacity has the opposite effects as those described in Section 8.5.3. Evolution through the pre-MS of all the test models is unaffected by the radiative opacity, as the stars contract in convective equilibrium. Ignition of hydrogen burning and increasing temperatures precipitates the formation of a radiative core, after which the base of the convective envelope recedes toward the stellar surface. Increasing the opacity causes the radiative core to form at an older age. Once the radiative core is established, the gas temperature and density decrease with increasing opacity. Stars continue to contract following this occurrence until the abundance of ${}^3\text{He}$ is sufficient for the p - p chain to establish equilibrium. Since a higher opacity cools the core, the star will end up contracting more than a star with a lower opacity. The result is that increasing the opacity leads to cooler, more compact, and therefore less luminous stars. Below approximately $0.28 M_{\odot}$, radiative opacities have no noticeable effect on stellar interiors as models predict the stars will remain entirely convective throughout their pre-MS and MS lifetime. For higher mass stars increasing the radiative opacity by 50%

would increase our mass estimates by about 10%.

However, the insensitivity of models to radiative opacities below the fully convective boundary means that errors in radiative opacities do not provide a robust solution to the disagreements noted in Section 8.3. One shortcoming of the present investigation is that opacities were not modified in the optically thin regions above $\tau = 10$, as pre-computed model atmospheres provide the surface boundary condition. It is not clear to what degree opacity changes are required in the outer layers to impart significant structural changes to fully convective stars.

9. SUMMARY & DISCUSSION

To better characterize the physical properties of M dwarfs, we determined precise temperatures, luminosities, radii, and metallicities for 183 nearby M dwarfs with well-determined distances. We obtained spectra of each star spanning 0.3 – $2.4 \mu\text{m}$ and took advantage of accurate spectrophotometric calibrations to derive T_{eff} , F_{bol} , and $[\text{Fe}/\text{H}]$, and hence R_* using the Stefan-Boltzmann relation. We then derived empirical relations between T_{eff} and $[\text{Fe}/\text{H}]$ and radii and luminosities and compared our derived parameters to predictions from new predictions by the Dartmouth stellar evolution model.

Our method of measuring T_{eff} was calibrated using stars with determinations from interferometry (Boyajian et al. 2012b; Mann et al. 2013b), so consistency between this method of estimation and LBOI is expected, and indeed shown for the set of LBOI stars. Further, using masses derived from the empirical mass- M_{K_s} relation of Delfosse et al. (2000) yields a mass-radius relation for our stars consistent within formal uncertainties for that determined from observations of LMEBs.

Our determinations are largely model-independent. One concern is that LBOI-determined angular diameters and T_{eff} require an estimate of limb darkening, which is typically based on from model spectra. These corrections are $\simeq 3\%$. However, the error from this correction is likely much less than 0.1%, which is a consequence of taking observations in the NIR where limb darkening effects are smaller. Further, Kreidberg et al. (2014) found that model limb darkening parameters are consistent with those derived from fitting high-S/N transits with HST within errors (5-15%).

More importantly, different interferometric observations of the same star have sometimes yielded different angular diameters (e.g., Bazot et al. 2011; Boyajian et al. 2012a). Casagrande et al. (2014) found that disagreement between angular diameter measurements grows with decreasing diameter beyond expected growth in measurement uncertainties. This suggests the presence of systematic errors that become increasingly important with decreasing angular size. This may be due to differences in how calibrator stars are handled, which become important for stars near the resolution limit of the array. Additional observations are needed to better understand these differences.

Another concern involves systematic uncertainties in our estimates of $[\text{Fe}/\text{H}]$, which were calibrated with spectroscopically-determined metallicities of solar-type (FGK) companions to a small number of M dwarfs. Different analyses have yielded systematically different metallicities for the same solar-type dwarfs (Hinkel et al. 2014). This was corrected for in Mann et al. (2013a) and Mann et al. (2014) by adjusting metallicity values from a given

reference using stars common to the reference source and to the SPOCS catalog (Valenti & Fischer 2005). While this puts all metallicities on the same scale, it is not necessarily the true scale.

Metallicity appears to have a minor but statistically significant effect on the M_{K_S} - R_* relation, and a highly significant effect on the T_{eff} - $[\text{Fe}/\text{H}]$ - R_* relation. If there is some systematic offset in the metallicity scale, our empirical relations that include $[\text{Fe}/\text{H}]$ can still be used provided metallicities are adjusted to match our adopted scale. However, systematic offsets in our metallicity scale could more significantly impact our model analysis, since the models rely on absolute metallicities. If our metallicities are systematically too high, the shift to a correct metallicity scale will force the models toward hotter T_{eff} , likely exaggerating the differences between model predictions and observations described in Section 8.3. Conversely, a shift of the metallicity scale in the opposite direction would make models in better agreement with observations.

Pre-MS stars are systematically larger than their older counterparts, and their inclusion could affect our derived relations. However, M dwarfs need to be < 100 Myr to be significantly inflated for a given M_K magnitude. Based on the age distribution of M dwarfs in the Solar neighborhood (Ansdell et al. 2015) there should be just 2-5 such young stars in our sample. Unsurprisingly, two of our stars (Gliese 896A and 896B) are purported to be members of young moving groups with ages $\lesssim 100$ Myr (Zuckerman et al. 2013). As expected, all three stars fall above our best-fit M_{K_S} - R_* relation, by 4.4% and 9.5%, respectively. However, neither of these differences are significant (1.3 and 2.3σ), and removing them from our fits resulted in negligible changes. Even if we assume there are three more such young stars in our sample, this would not create any significant changes in our results.

We used the parameters of this sample to construct empirical relations between more readily observed parameters (T_{eff} , $[\text{Fe}/\text{H}]$, and M_K), and less accessible parameters, i.e., R_* and M_* (Equation 4, Table 1). Our M_{K_S} - R_* relation has a scatter of only 2.9%, and 2.7% when $[\text{Fe}/\text{H}]$ is included. The scatter and χ^2_ν in the absolute magnitude- R_* relation is smallest when using K_S compared to other filters, a consequence of the increasing role of $[\text{Fe}/\text{H}]$ at bluer wavelengths. Unfortunately redder photometry is not available, as *WISE* photometry saturates on a sizable fraction of our stars, and our empirical spectra only go to $2.5\mu\text{m}$, so we could not generate reliable empirical synthetic *WISE* magnitudes.

Our derived T_{eff} - R_* relation can be used to predict stellar radii accurate to 13%. When $[\text{Fe}/\text{H}]$ is included the relation is accurate to 9% in radius, or perhaps better, as suggested by the low χ^2_ν value. In this work, we found a significant correlation between $[\text{Fe}/\text{H}]$ and the T_{eff} - R_* relation. The effect of $[\text{Fe}/\text{H}]$ was not seen in previous empirical studies with smaller collections of stars and sparser sampling in $[\text{Fe}/\text{H}]$ (Boyajian et al. 2012b; Mann et al. 2013b). These earlier findings did not necessarily exclude $[\text{Fe}/\text{H}]$ dependence, but only showed that any correlation was not statistically significant. They were also hampered by a coincidence in the metallicities and temperatures of their sample. In Figure 23 we show the T_{eff} - R_* distribution of stars from our sample along

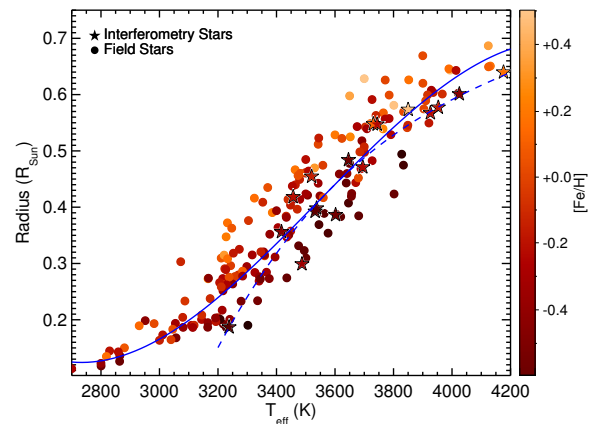


Figure 23. Radius vs. T_{eff} of our sample (circles) and the LBOI sample (5-point stars) used by Mann et al. (2013b). Gliese 725B is not shown because it was not included in the fits from Mann et al. (2013b). The best-fit relation from Mann et al. (2013b) is shown as a blue dashed line, while the fit from this paper (Equation 4) is shown as a blue solid line. Points are color-coded by metallicity.

with those stars used in Boyajian et al. (2012b) and Mann et al. (2013b). The LBOI (long-baseline optical interferometry) stars with $T_{\text{eff}} < 3700$ K happen to be more metal poor. Thus much of the effect of metallicity on the T_{eff} - R_* relation was masked by an (inaccurately) steeper dependence on T_{eff} .

The coverage and quality of our spectra enabled us to generate synthetic $VR_C I_C \text{Griz} JHK_S$ and *Gaia* G , G_{RP} , and G_{BP} photometry for all stars in our sample, which we used to generate empirical relations between color and T_{eff} (Table 2), and derive bolometric corrections for all relevant pass-bands (Table 3). We find that T_{eff} can be determined to an accuracy of 70-80 K and bolometric corrections to an accuracy of 2-3% from color relations alone. More accurate T_{eff} and BC values are possible if $[\text{Fe}/\text{H}]$ is independently established, but even when $[\text{Fe}/\text{H}]$ is not known, the $[\text{Fe}/\text{H}]$ dependence can be mitigated by exploiting relations between JHK_S colors and $[\text{Fe}/\text{H}]$ for M dwarfs.

We compared our parameter values to predictions from the Dartmouth model grid using a MCMC method to obtain best-fit model parameters. We find that, while F_{bol} are accurately predicted by the models (by design), there are still slight discrepancies that correlate significantly with inferred T_{eff} (or mass) above 3500 K ($\sim 0.4 M_\odot$). The broad consensus that models systematically underestimate stellar radii and over-estimate stellar T_{eff} among M dwarfs is supported by our data, which show average systematic offsets of 4.7% and -2.2% , respectively. These correspond to average deviations of 1.1σ and 1.2σ from the observations. While not all offsets between model predictions and the observations for individual stars are significant compared to the formal uncertainties, the offsets are systematic and hence significant when considering the full sample. This characterization of model errors is to similar that for LMEBs (Feiden & Chaboyer 2012a; Spada et al. 2013) and stars in the LBOI sample (Spada et al. 2013; Boyajian et al. 2012b).

Although we uncover significant disagreements between model predictions and observations, we find no significant correlation between these offsets and stellar mass, metallicity, or magnetic activity. There have been no previous

claims that modeling errors correspond with stellar mass, so it is not surprising that no correlation was uncovered. A correlation between model radius offsets and metallicity was suggested by previous investigations of single field stars (Berger et al. 2006; López-Morales 2007), but we find no evidence to support this claim. In a similar manner, we find model errors to be independent of observed $H\alpha$ activity measures, the ratio of coronal X-ray flux to F_{bol} , and both NUV and FUV fluxes. This is a somewhat surprising result given the mounting evidence in favor of magnetic fields and/or activity inflating stars in LMEBs (e.g., Kraus et al. 2011; MacDonald & Mullan 2012; Feiden & Chaboyer 2012b, 2013; Torres et al. 2014). The stars in our sample appear to be systematically larger and cooler than model predictions, *independent of their level of magnetic activity*. If activity does inflate the radii of late-type stars, then the effect must be much weaker than previously suggested. Furthermore, since single stars and LMEBs are similarly inflated, magnetic activity is no longer necessary to explain LMEB inflation.

Previous studies have suggested a need to increase the He abundance to reconcile models and observations of LMEBs (e.g., Paczynski & Sienkiewicz 1984; Metcalfe et al. 1996; Lastennet et al. 2003; Feiden & Chaboyer 2014b). Interestingly, we find the opposite, that He abundance must be reduced to provide better agreement with models. This is most likely a consequence of using luminosity, T_{eff} , and radius as the observables, whereas studies of LMEBs use mass and radius. However, if we assume that the inflation we observe has the same origin as that observed in LMEBs—which is likely given that the discrepancies have almost identical magnitude and direction—this suggests that incorrect He abundances *cannot* be the origin. If He abundance were the cause, the requisite adjustments for LMEBs and our sample would be in agreement.

It would be interesting to apply our methodology to yet cooler stars (i.e., late M dwarfs and even L dwarfs), probing the physics at the stellar-substellar boundary. While previous studies have used similar methods on such ultracool dwarfs (e.g., Dieterich et al. 2014), parameters were either less precise or model-dependent. More importantly, it has only become recently possible to measure metallicities to spectral types as late as M9.5 (Mann et al. 2014), and there are no dwarfs with interferometric measurements beyond M6, making it difficult to test the T_{eff} determinations empirically. Adaptive optics for CHARA (Che et al. 2013), and other instrumentation upgrades may enable measurements for the brightest and closest ultracool dwarfs.

The ESA *Gaia* mission, launched in 2013 December, will enormously expand the number of M dwarfs with precise trigonometric parallaxes (de Bruijne 2012). Our empirical and model-based relations can be applied to these stars, including those hosting planets expected to be discovered by the NASA K2 and TESS missions and the ESA PLATO mission. Currently *Kepler* M dwarf radii have been recently estimated using model fits (Gaidos et al. 2013), T_{eff} -based relations from models (e.g., Muirhead et al. 2014) or nearby stars (e.g., Mann et al. 2013c; Newton et al. 2015). But these methods are only good to $\simeq 10\%$. With *Gaia* trigonometric parallaxes combined with the $M_{K_s} - R_*$ and $M_{K_s} - M_*$ relations from this paper will be possible to measure stellar radii accurate

to 3% and stellar masses to 2% for M dwarfs, enabling far more precise determination of planet radii and densities (with radial velocity measurements). This will also provide accurate parameters for the entire set of targets, important when calculating planet occurrence rates or searching for planet-metallicity correlations.

Thanks to the anonymous referee for their fast and generous comments. Thanks to Keivan Stassun for his comments on activity diagnostics, to Michael Cushing for providing a pre-release version of SpexTools for uSpeX, and to Coryn Bailer-Jones for providing the spectral response profiles for *Gaia*. Additional thanks thanks to Adam Kraus, Chao-Ling Hung, and Aaron Rizzuto for useful discussions on the content of this manuscript. PPD Figures were made with the aid of the triangle.py package (Foreman-Mackey et al. 2014). This research was supported by NASA grants NNX10AQ36G and NNX11AC33G to EG and NASA grants ADAP12-0172 and 14-XRP14 2-0147 to TB.

SNIFS on the UH 2.2-m telescope is part of the Nearby Supernova Factory project, a scientific collaboration among the Centre de Recherche Astronomique de Lyon, Institut de Physique Nuclaire de Lyon, Laboratoire de Physique Nuclaire et des Hautes Energies, Lawrence Berkeley National Laboratory, Yale University, University of Bonn, Max Planck Institute for Astrophysics, Tsinghua Center for Astrophysics, and the Centre de Physique des Particules de Marseille. Based on data from the Infrared Telescope Facility, which is operated by the University of Hawaii under Cooperative Agreement no. NNX-08AE38A with the National Aeronautics and Space Administration, Science Mission Directorate, Planetary Astronomy Program. Some/all of the data presented in this paper were obtained from the Mikulski Archive for Space Telescopes (MAST). STScI is operated by the Association of Universities for Research in Astronomy, Inc., under NASA contract NAS5-26555. Support for MAST for non-HST data is provided by the NASA Office of Space Science via grant NNX09AF08G and by other grants and contracts. The CHARA Array is funded by the National Science Foundation through NSF grants AST-0606958 and AST-0908253 and by Georgia State University through the College of Arts and Sciences, as well as the W. M. Keck Foundation. This research made use of the SIMBAD and VIZIER Astronomical Databases, operated at CDS, Strasbourg, France (<http://cdsweb.u-strasbg.fr/>), and of NASA Astrophysics Data System, of the Jean-Marie Mariotti Center SearchCal service (<http://www.jmmc.fr/searchcal>), co-developed by FIZEAU and LAOG/IPAG.

Facilities: IRTF:SpeX, UH:2.2m (SNIFS), CHARA

REFERENCES

- Adelberger, E. G., García, A., Robertson, R. G. H., et al. 2011, *Reviews of Modern Physics*, **83**, 195
- Aldering, G., Adam, G., Antilogus, P., et al. 2002, in *Society of Photo-Optical Instrumentation Engineers (SPIE) Conference Series*, Vol. 4836, *Survey and Other Telescope Technologies and Discoveries*, ed. J. A. Tyson & S. Wolff, 61
- Aldering, G., Antilogus, P., Bailey, S., et al. 2006, *ApJ*, **650**, 510
- Allard, F., Homeier, D., & Freytag, B. 2011, in *Astronomical Society of the Pacific Conference Series*, Vol. 448, 16th Cambridge Workshop on Cool Stars, Stellar Systems, and the Sun, ed. C. Johns-Krull, M. K. Browning, & A. A. West, 91
- Allard, F., Homeier, D., Freytag, B., et al. 2013, *Memorie della Societa Astronomica Italiana Supplementi*, **24**, 128
- Ansdell, M., Gaidos, E., Mann, A. W., et al. 2015, *ApJ*, **798**, 41
- Asplund, M., Grevesse, N., Sauval, A. J., & Scott, P. 2009, *ARA&A*, **47**, 481
- Aumer, M., & Binney, J. J. 2009, *MNRAS*, **397**, 1286
- Bacon, R., Copin, Y., Monnet, G., et al. 2001, *MNRAS*, **326**, 23
- Bahcall, J. N., Basu, S., Pinsonneault, M., & Serenelli, A. M. 2005, *ApJ*, **618**, 1049
- Barber, C. B., Dobkin, D. P., & Huhdanpaa, H. 1996, *ACM Trans. Math. Softw.*, **22**, 469
- Bass, G., Orosz, J. A., Welsh, W. F., et al. 2012, *ApJ*, **761**, 157
- Basu, S., & Antia, H. M. 2008, *Phys. Rep.*, **457**, 217
- Bazot, M., Ireland, M. J., Huber, D., et al. 2011, *A&A*, **526**, L4
- Berger, D. H., Gies, D. R., McAlister, H. A., et al. 2006, *ApJ*, **644**, 475
- Bessell, M. S. 1999, *PASP*, **111**, 1426
- Bohlin, R. C. 2007, in *Astronomical Society of the Pacific Conference Series*, Vol. 364, *The Future of Photometric, Spectrophotometric and Polarimetric Standardization*, ed. C. Sterken, 315
- Bohlin, R. C., Dickinson, M. E., & Calzetti, D. 2001, *AJ*, **122**, 2118
- Bohlin, R. C., & Gilliland, R. L. 2004a, *AJ*, **128**, 3053
- . 2004b, *AJ*, **127**, 3508
- Bonaca, A., Tanner, J. D., Basu, S., et al. 2012, *ApJ*, **755**, L12
- Bonfils, X., Delfosse, X., Udry, S., et al. 2005, *A&A*, **442**, 635
- Boyajian, T., von Braun, K., Feiden, G. A., et al. 2015, *MNRAS*, **447**, 850
- Boyajian, T. S., McAlister, H. A., van Belle, G., et al. 2012a, *ApJ*, **746**, 101
- Boyajian, T. S., von Braun, K., van Belle, G., et al. 2012b, *ApJ*, **757**, 112
- Buton, C., Copin, Y., Aldering, G., et al. 2013, *A&A*, **549**, A8
- Caffau, E., Ludwig, H.-G., Steffen, M., Freytag, B., & Bonifacio, P. 2011, *Sol. Phys.*, **268**, 255
- Carpenter, J. M. 2001, *AJ*, **121**, 2851
- Carter, J. A., Fabrycky, D. C., Ragozzine, D., et al. 2011, *Science*, **331**, 562
- Casagrande, L., Flynn, C., & Bessell, M. 2008, *MNRAS*, **389**, 585
- Casagrande, L., Portinari, L., & Flynn, C. 2006, *MNRAS*, **373**, 13
- Casagrande, L., Portinari, L., Glass, I. S., et al. 2014, *MNRAS*, **439**, 2060
- Cassan, A., Kubas, D., Beaulieu, J.-P., et al. 2012, *Nature*, **481**, 167
- Chabrier, G., & Baraffe, I. 1997, *A&A*, **327**, 1039
- Chabrier, G., Gallardo, J., & Baraffe, I. 2007, *A&A*, **472**, L17
- Che, X., Sturmman, L., Monnier, J. D., et al. 2013, *Journal of Astronomical Instrumentation*, **2**, 40007
- Chen, Y., Girardi, L., Bressan, A., et al. 2014, *MNRAS*, **444**, 2525
- Cohen, M., Wheaton, W. A., & Megeath, S. T. 2003, *AJ*, **126**, 1090
- Cox, A. N., Hodson, S. W., & Shaviv, G. 1981, *ApJ*, **245**, L37
- Cushing, M. C., Vacca, W. D., & Rayner, J. T. 2004, *PASP*, **116**, 362
- de Bruijne, J. H. J. 2012, *Ap&SS*, **341**, 31
- Delahaye, F., & Pinsonneault, M. H. 2006, *ApJ*, **649**, 529
- Delfosse, X., Forveille, T., Ségransan, D., et al. 2000, *A&A*, **364**, 217
- Demory, B.-O., Ségransan, D., Forveille, T., et al. 2009, *A&A*, **505**, 205
- Dieterich, S. B., Henry, T. J., Jao, W.-C., et al. 2014, *AJ*, **147**, 94
- Dittmann, J. A., Irwin, J. M., Charbonneau, D., & Berta-Thompson, Z. K. 2014, *ApJ*, **784**, 156
- Dotter, A., Chaboyer, B., Jevremović, D., et al. 2008, *ApJS*, **178**, 89
- Doyle, L. R., Carter, J. A., Fabrycky, D. C., et al. 2011, *Science*, **333**, 1602
- Dressing, C. D., & Charbonneau, D. 2013, *ApJ*, **767**, 95
- Feiden, G. A., & Chaboyer, B. 2012a, *ApJ*, **757**, 42
- . 2012b, *ApJ*, **761**, 30
- . 2013, *ApJ*, **779**, 183
- . 2014a, *ApJ*, **789**, 53
- . 2014b, *A&A*, **571**, A70
- Ferguson, J. W., Alexander, D. R., Allard, F., et al. 2005, *ApJ*, **623**, 585
- Fischer, D. A., & Marcy, G. W. 1992, *ApJ*, **396**, 178
- Fischer, D. A., & Valenti, J. 2005, *ApJ*, **622**, 1102
- Foreman-Mackey, D., Hogg, D. W., Lang, D., & Goodman, J. 2013, *PASP*, **125**, 306
- Foreman-Mackey, D., Price-Whelan, A., Ryan, G., et al. 2014, *Zenodo*
- Fukugita, M., Ichikawa, T., Gunn, J. E., et al. 1996, *AJ*, **111**, 1748
- Gaidos, E. 2013, *ApJ*, **770**, 90
- Gaidos, E., Fischer, D. A., Mann, A. W., & Howard, A. W. 2013, *ApJ*, **771**, 18
- Gaidos, E., & Mann, A. W. 2014, *ApJ*, **791**, 54
- Gaidos, E., Mann, A. W., Lépine, S., et al. 2014, *MNRAS*, **443**, 2561
- Gatewood, G. 2008, *AJ*, **136**, 452
- Gatewood, G., & Coban, L. 2009, *AJ*, **137**, 402
- Goodman, J., & Weare, J. 2010, *Commun. Appl. Math. Comput. Sci.*, **5**, 65
- Gregg, M. D., Silva, D., Rayner, J., et al. 2006, in *The 2005 HST Calibration Workshop: Hubble After the Transition to Two-Gyro Mode*, ed. A. M. Koekemoer, P. Goudfrooij, & L. L. Dressel, 209
- Grevesse, N., & Sauval, A. J. 1998, *Space Sci. Rev.*, **85**, 161
- Hamuy, M., Suntzeff, N. B., Heathcote, S. R., et al. 1994, *PASP*, **106**, 566
- Harrington, R. S., Dahn, C. C., Kallarakal, V. V., et al. 1993, *AJ*, **105**, 1571
- Hartkopf, W. I., McAlister, H. A., & Mason, B. D. 2001, *AJ*, **122**, 3480
- Hauschildt, P. H., Allard, F., & Baron, E. 1999, *ApJ*, **512**, 377
- Heap, S. R., & Lindler, D. J. 2007, in *Astronomical Society of the Pacific Conference Series*, Vol. 374, *From Stars to Galaxies: Building the Pieces to Build Up the Universe*, ed. A. Vallenari, R. Tantaló, L. Portinari, & A. Moretti, 409
- Helminiak, K. G., Konacki, M., RóŻyczka, M., et al. 2012, *MNRAS*, **425**, 1245
- Henden, A. A., Levine, S. E., Terrell, D., Smith, T. C., & Welch, D. 2012, *Journal of the American Association of Variable Star Observers (JAAVSO)*, **40**, 430
- Henry, T. J., Jao, W.-C., Subasavage, J. P., et al. 2006, *AJ*, **132**, 2360
- Henry, T. J., Kirkpatrick, J. D., & Simons, D. A. 1994, *AJ*, **108**, 1437
- Hill, F., Fischer, G., Forgach, S., et al. 1994, *Sol. Phys.*, **152**, 351
- Hinkel, N. R., Timmes, F. X., Young, P. A., Pagano, M. D., & Turnbull, M. C. 2014, *AJ*, **148**, 54
- Høg, E., Fabricius, C., Makarov, V. V., et al. 2000, *A&A*, **355**, L27
- Howard, A. W., Marcy, G. W., Bryson, S. T., et al. 2012, *ApJS*, **201**, 15
- Iglesias, C. A., & Rogers, F. J. 1996, *ApJ*, **464**, 943
- Irwin, J., Charbonneau, D., Berta, Z. K., et al. 2009, *ApJ*, **701**, 1436
- Irwin, J. M., Quinn, S. N., Berta, Z. K., et al. 2011, *ApJ*, **742**, 123
- Janson, M., Bergfors, C., Brandner, W., et al. 2014, *ApJ*, **789**, 102
- Janson, M., Hormuth, F., Bergfors, C., et al. 2012, *ApJ*, **754**, 44
- Jao, W.-C., Henry, T. J., Subasavage, J. P., et al. 2005, *AJ*, **129**, 1954
- . 2011, *AJ*, **141**, 117
- Jarrett, T. H., Cohen, M., Masci, F., et al. 2011, *ApJ*, **735**, 112
- Johnson, J. A., Aller, K. M., Howard, A. W., & Crepp, J. R. 2010, *PASP*, **122**, 905
- Johnson, J. A., Gazak, J. Z., Apps, K., et al. 2012, *AJ*, **143**, 111
- Jordi, C., Gebran, M., Carrasco, J. M., et al. 2010, *A&A*, **523**, A48
- Kervella, P., Mérand, A., Pichon, B., et al. 2008, *A&A*, **488**, 667
- Kopparapu, R. K., Ramirez, R., Kasting, J. F., et al. 2013, *ApJ*, **765**, 131
- Kraus, A. L., Tucker, R. A., Thompson, M. I., Craine, E. R., & Hillenbrand, L. A. 2011, *ApJ*, **728**, 48

- Kreidberg, L., Bean, J. L., Désert, J.-M., et al. 2014, *Nature*, **505**, 69
- Lada, C. J. 2006, *ApJ*, **640**, L63
- Lane, B. F., Boden, A. F., & Kulkarni, S. R. 2001, *ApJ*, **551**, L81
- Lantz, B., Aldering, G., Antilogus, P., et al. 2004, in *Society of Photo-Optical Instrumentation Engineers (SPIE) Conference Series*, Vol. 5249, *Optical Design and Engineering*, ed. L. Mazuray, P. J. Rogers, & R. Wartmann, 146
- Lastennet, E., Fernandes, J., Valls-Gabaud, D., & Oblak, E. 2003, *A&A*, **409**, 611
- Leggett, S. K. 1992, *ApJS*, **82**, 351
- Lépine, S., & Gaidos, E. 2011, *AJ*, **142**, 138
- Lépine, S., Hilton, E. J., Mann, A. W., et al. 2013, *AJ*, **145**, 102
- Lépine, S., Rich, R. M., & Shara, M. M. 2003, *AJ*, **125**, 1598
- Lépine, S., Thorstensen, J. R., Shara, M. M., & Rich, R. M. 2009, *AJ*, **137**, 4109
- López-Morales, M. 2007, *ApJ*, **660**, 732
- Lopez-Morales, M., Orosz, J. A., Shaw, J. S., et al. 2006, *ArXiv Astrophysics e-prints*, [astro-ph/0610225](https://arxiv.org/abs/astro-ph/0610225)
- López-Morales, M., & Ribas, I. 2005, *ApJ*, **631**, 1120
- López-Morales, M., & Shaw, J. S. 2007, in *Astronomical Society of the Pacific Conference Series*, Vol. 362, *The Seventh Pacific Rim Conference on Stellar Astrophysics*, ed. Y. W. Kang, H.-W. Lee, K.-C. Leung, & K.-S. Cheng, 26
- MacDonald, J., & Mullan, D. J. 2012, *MNRAS*, **421**, 3084
- Mamajek, E. E. 2012, *ApJ*, **754**, L20
- Mann, A. W., Brewer, J. M., Gaidos, E., Lépine, S., & Hilton, E. J. 2013a, *AJ*, **145**, 52
- Mann, A. W., Deacon, N. R., Gaidos, E., et al. 2014, *AJ*, **147**, 160
- Mann, A. W., Gaidos, E., & Aldering, G. 2011, *PASP*, **123**, 1273
- Mann, A. W., Gaidos, E., & Ansdell, M. 2013b, *ApJ*, **779**, 188
- Mann, A. W., Gaidos, E., Kraus, A., & Hilton, E. J. 2013c, *ApJ*, **770**, 43
- Mann, A. W., & von Braun, K. 2015, *PASP*, **127**, 102
- Markwardt, C. B. 2009, in *Astronomical Society of the Pacific Conference Series*, Vol. 411, *Astronomical Data Analysis Software and Systems XVIII*, ed. D. A. Bohlender, D. Durand, & P. Dowler, 251
- Martin, D. C., Fanson, J., Schiminovich, D., et al. 2005, *ApJ*, **619**, L1
- Mason, B. D., Wycoff, G. L., Hartkopf, W. I., Douglass, G. G., & Worley, C. E. 2001, *AJ*, **122**, 3466
- Mermilliod, J.-C., Mermilliod, M., & Hauck, B. 1997, *A&AS*, **124**, 349
- Metcalf, T. S., Mathieu, R. D., Latham, D. W., & Torres, G. 1996, *ApJ*, **456**, 356
- Morales, J. C., Torres, G., Marschall, L. A., & Brehm, W. 2009a, *ApJ*, **707**, 671
- Morales, J. C., Ribas, I., Jordi, C., et al. 2009b, *ApJ*, **691**, 1400
- Morton, T. D., & Swift, J. 2014, *ApJ*, **791**, 10
- Muirhead, P. S., Becker, J., Feiden, G. A., et al. 2014, *ApJS*, **213**, 5
- Mullan, D. J., & MacDonald, J. 2001, *ApJ*, **559**, 353
- Neves, V., Bonfils, X., Santos, N. C., et al. 2013, *A&A*, **551**, A36
- . 2014, *A&A*, **568**, A121
- . 2012, *A&A*, **538**, A25
- Newton, E. R., Charbonneau, D., Irwin, J., et al. 2014, *AJ*, **147**, 20
- Newton, E. R., Charbonneau, D., Irwin, J., & Mann, A. W. 2015, *ApJ*, **800**, 85
- Oke, J. B. 1990, *AJ*, **99**, 1621
- Orosz, J. A., Welsh, W. F., Carter, J. A., et al. 2012a, *Science*, **337**, 1511
- . 2012b, *ApJ*, **758**, 87
- Paczynski, B., & Sienkiewicz, R. 1984, *ApJ*, **286**, 332
- Pecaut, M. J., & Mamajek, E. E. 2013, *ApJS*, **208**, 9
- Peimbert, M., Luridiana, V., & Peimbert, A. 2007, *ApJ*, **666**, 636
- Raghavan, D., McAlister, H. A., Henry, T. J., et al. 2010, *ApJS*, **190**, 1
- Rajpurohit, A. S., Reylé, C., Allard, F., et al. 2013, *A&A*, **556**, A15
- Rauer, H., Catala, C., Aerts, C., et al. 2014, *Experimental Astronomy*, [arXiv:1310.0696](https://arxiv.org/abs/1310.0696) [[astro-ph](https://arxiv.org/abs/astro-ph).EP]
- Rayner, J. T., Cushing, M. C., & Vacca, W. D. 2009, *ApJS*, **185**, 289
- Rayner, J. T., Toomey, D. W., Onaka, P. M., et al. 2003, *PASP*, **115**, 362
- Reid, I. N., Hawley, S. L., & Gizis, J. E. 1995, *AJ*, **110**, 1838
- Ribas, I. 2003, *A&A*, **398**, 239
- Ricker, G. R. 2014, *Journal of the American Association of Variable Star Observers (JAAVSO)*, **42**, 234
- Riedel, A. R., Subasavage, J. P., Finch, C. T., et al. 2010, *AJ*, **140**, 897
- Rojas-Ayala, B., Covey, K. R., Muirhead, P. S., & Lloyd, J. P. 2012, *ApJ*, **748**, 93
- Santos, N. C., Israelian, G., & Mayor, M. 2004, *A&A*, **415**, 1153
- Schlaufman, K. C., & Laughlin, G. 2010, *A&A*, **519**, A105
- Schmitt, J. H. M. M., Fleming, T. A., & Giampapa, M. S. 1995, *ApJ*, **450**, 392
- Ségransan, D., Kervella, P., Forveille, T., & Queloz, D. 2003, *A&A*, **397**, L5
- Skrutskie, M. F., Cutri, R. M., Stiening, R., et al. 2006, *AJ*, **131**, 1163
- Spada, F., Demarque, P., Kim, Y.-C., & Sills, A. 2013, *ApJ*, **776**, 87
- Stassun, K. G., Kratter, K. M., Scholz, A., & Dupuy, T. J. 2012, *ApJ*, **756**, 47
- Terrien, R. C., Mahadevan, S., Bender, C. F., et al. 2012, *ApJ*, **747**, L38
- Tinney, C. G., & Reid, I. N. 1998, *MNRAS*, **301**, 1031
- Torres, G., Fischer, D. A., Sozzetti, A., et al. 2012, *ApJ*, **757**, 161
- Torres, G., & Ribas, I. 2002, *ApJ*, **567**, 1140
- Torres, G., Sandberg Lacy, C. H., Pavlovski, K., et al. 2014, *ApJ*, **797**, 31
- Vacca, W. D., Cushing, M. C., & Rayner, J. T. 2003, *PASP*, **115**, 389
- Valenti, J. A., & Fischer, D. A. 2005, *ApJS*, **159**, 141
- van Belle, G. T., van Belle, G., Creech-Eakman, M. J., et al. 2008, *ApJS*, **176**, 276
- van Leeuwen, F. 2007, *A&A*, **474**, 653
- Voges, W., Aschenbach, B., Boller, T., et al. 1999, *A&A*, **349**, 389
- . 2000, *IAU Circ.*, **7432**, 3
- von Braun, K., Boyajian, T. S., Kane, S. R., et al. 2011, *ApJ*, **729**, L26
- . 2012, *ApJ*, **753**, 171
- von Braun, K., Boyajian, T. S., van Belle, G. T., et al. 2014, *MNRAS*, **438**, 2413
- Wright, E. L., Eisenhardt, P. R. M., Mainzer, A. K., et al. 2010, *AJ*, **140**, 1868
- Zuckerman, B., Vican, L., Song, I., & Schneider, A. 2013, *ApJ*, **778**, 5

Table 1
 Mass and Radius Relations

Y	X	Eqn #	a	b	c	d	e	f	σ^a %	χ^2_ν
R_*	M_{K_S}	(4)	1.9515	-0.3520	0.01680	2.89	0.93
R_*	$M_{K_S}, [\text{Fe}/\text{H}]$	(5)	1.9305	-0.3466	0.01647	0.04458	2.70	0.88
R_*	$T_{\text{eff}}/3500$	(4)	10.5440	-33.7546	35.1909	-11.5928	13.4	2.35
R_*	$T_{\text{eff}}/3500, [\text{Fe}/\text{H}]$	(5)	16.7700	-54.3210	57.6627	-19.6994	...	0.4565	9.3	1.10
M_*^c	M_{K_S}	(10)	0.5858	0.3872	-0.1217	0.0106	-2.7262×10^{-4}	...	1.8	0.37

Note. — For the first, third, and fifth equation $Y = a + bX + c^2 \dots$, for the equations including $[\text{Fe}/\text{H}]$ the right-hand side is multiplied by $(1+f[\text{Fe}/\text{H}])$.

^a For the first three relations σ is given as the percent scatter in R_* , i.e., the standard deviation of $\frac{R_{*,\text{observed}} - R_{*,\text{predicted}}}{R_{*,\text{observed}}}$. The last relation is quoted as the percent scatter in M_* .

^c Semi-empirical relation derived using empirical K_S -band magnitudes and masses estimated from our model analysis. Coefficients are calculated using maximum likelihood and a MCMC method. See Section 8 for details.

Table 2
 T_{eff} Relation Coefficients

Y	X	a	b	c	d	e	f	g	σ^a K	χ^2_ν
$T_{\text{eff}}/3500$	$BP - RP$	3.245	-2.4309	1.043	-0.2127	0.01649	52	0.88
$T_{\text{eff}}/3500$	$V - J$	2.840	-1.3453	0.3906	-0.0546	0.002913	55	0.93
$T_{\text{eff}}/3500$	$V - Ic$	2.455	-1.5701	0.6891	-0.1500	0.01254	53	0.94
$T_{\text{eff}}/3500$	$r - z$	1.547	-0.7053	0.3656	-0.1008	0.01046	58	1.06
$T_{\text{eff}}/3500$	$r - J$	2.445	-1.2578	0.4340	-0.0720	0.004502	58	1.04
$T_{\text{eff}}/3500$	$BP - RP, [\text{Fe}/\text{H}]$	2.835	-1.893	0.7860	-0.1594	0.01243	0.04417	...	45	0.60
$T_{\text{eff}}/3500$	$V - J, [\text{Fe}/\text{H}]$	2.515	-1.054	0.2965	-0.04150	0.002245	0.05262	...	42	0.53
$T_{\text{eff}}/3500$	$V - Ic, [\text{Fe}/\text{H}]$	1.901	-0.6564	0.1471	-0.01274	...	0.04697	...	48	0.67
$T_{\text{eff}}/3500$	$r - z, [\text{Fe}/\text{H}]$	1.572	-0.7220	0.3560	-0.09221	0.009071	0.05220	...	50	0.71
$T_{\text{eff}}/3500$	$r - J, [\text{Fe}/\text{H}]$	2.532	-1.319	0.4449	-0.07151	0.004333	0.05629	...	47	0.63
$T_{\text{eff}}/3500$	$BP - RP, J - H$	3.172	-2.475	1.082	-0.2231	0.01738	0.08776	0.04355	49	0.78
$T_{\text{eff}}/3500$	$V - J, J - H$	2.769	-1.421	0.4284	-0.06133	0.003310	0.1333	0.05416	48	0.71
$T_{\text{eff}}/3500$	$V - Ic, J - H$	1.568	-0.4381	0.07749	-0.005610	...	0.2441	-0.09257	52	0.85
$T_{\text{eff}}/3500$	$r - z, J - H$	1.384	-0.6132	0.3110	-0.08574	0.008895	0.1865	-0.02039	55	0.90
$T_{\text{eff}}/3500$	$r - J, J - H$	2.151	-1.092	0.3767	-0.06292	0.003950	0.1697	0.03106	52	0.79

Note. — The first five formulae follow Equation 4, the middle five follow Equation 6 (f is the coefficient of the $[\text{Fe}/\text{H}]$ term), and the last five follow Equation 7 (f and g are the coefficients for the $J - H$ and $(J - H)^2$ terms, respectively). Equations using $J - H$ as an additional variable are meant for when the metallicity is not known.

^a We report the scatter in the predicted - observed (from spectrum) T_{eff} . Conservatively, these errors should be added (in quadrature) with our typical spectroscopic uncertainty (60 K).

Table 3
Bolometric Correction Formulae

BC _Y	X	a	b	c	d	e	σ	χ _ν ²
<i>V</i>	<i>V</i> − <i>J</i>	0.5817	−0.4168	−0.08165	4.084 × 10 ^{−3}	...	0.016	0.88
<i>Rc</i>	<i>V</i> − <i>J</i>	2.127	−1.059	0.1029	−7.881 × 10 ^{−3}	...	0.031	2.97
<i>Ic</i>	<i>V</i> − <i>J</i>	0.4440	0.2331	−0.05313	0.037	2.47
<i>r</i>	<i>r</i> − <i>J</i>	0.8958	−0.5081	−0.07387	3.999 × 10 ^{−3}	...	0.016	0.56
<i>i</i>	<i>r</i> − <i>J</i>	0.4431	−0.06470	−0.04038	2.798 × 10 ^{−5}	...	0.031	2.86
<i>z</i>	<i>r</i> − <i>J</i>	0.05373	0.2980	−0.05001	0.035	3.53
<i>Gaia BP</i> − <i>RP</i>		0.7384	−0.7398	0.01340	0.045	5.93
<i>J</i>	<i>V</i> − <i>J</i>	0.8694	0.3667	−0.02920	0.016	0.90
<i>J</i>	<i>r</i> − <i>J</i>	0.8790	0.5068	−0.07791	4.338 × 10 ^{−3}	...	0.016	0.92
<i>H</i>	<i>V</i> − <i>J</i>	1.834	0.2054	−0.01271	0.030	1.96
<i>H</i>	<i>r</i> − <i>J</i>	1.939	0.1969	−0.01337	0.029	1.87
<i>K</i>	<i>V</i> − <i>J</i>	1.421	0.6084	−0.09655	6.263 × 10 ^{−3}	...	0.036	2.44
<i>K</i>	<i>r</i> − <i>J</i>	1.719	0.5236	−0.09085	6.735 × 10 ^{−3}	...	0.036	2.36
<i>V</i>	<i>V</i> − <i>J</i> , [Fe/H]	0.6570	−0.4710	−0.06943	3.206 × 10 ^{−3}	−0.04885	0.012	0.50
<i>Rc</i>	<i>V</i> − <i>J</i> , [Fe/H]	2.183	−1.102	0.1126	−8.579 × 10 ^{−3}	−0.09587	0.025	1.92
<i>Ic</i>	<i>V</i> − <i>J</i> , [Fe/H]	0.5043	0.1994	−0.04883	...	−0.06312	0.032	1.82
<i>r</i>	<i>r</i> − <i>J</i> , [Fe/H]	0.9341	−0.5432	−0.06423	3.170 × 10 ^{−3}	−0.05569	0.012	0.28
<i>i</i>	<i>r</i> − <i>J</i> , [Fe/H]	0.5235	−0.1326	−0.02203	−1.541 × 10 ^{−3}	−0.1396	0.028	2.60
<i>z</i>	<i>r</i> − <i>J</i> , [Fe/H]	0.1009	0.2658	−0.04509	...	−0.07352	0.028	2.44
<i>Gaia BP</i> − <i>RP</i> , [Fe/H]		0.7567	−0.7541	0.01574	...	−0.1212	0.037	4.39
<i>J</i>	<i>V</i> − <i>J</i> , [Fe/H]	0.8879	0.3563	−0.02791	...	−0.04857	0.012	0.64
<i>J</i>	<i>r</i> − <i>J</i> , [Fe/H]	0.9672	0.4291	−0.05677	2.528 × 10 ^{−3}	−0.05249	0.012	0.56
<i>H</i>	<i>V</i> − <i>J</i> , [Fe/H]	1.796	0.2260	−0.01525	...	0.09544	0.021	1.02
<i>H</i>	<i>r</i> − <i>J</i> , [Fe/H]	1.915	0.2135	−0.01582	...	0.09088	0.021	1.01
<i>K</i>	<i>V</i> − <i>J</i> , [Fe/H]	1.197	0.7714	−0.1339	8.998 × 10 ^{−3}	0.09572	0.030	1.68
<i>K</i>	<i>r</i> − <i>J</i> , [Fe/H]	1.572	0.6529	−0.1260	9.746 × 10 ^{−3}	0.08987	0.030	1.68

Note. — All relations are of the form $BC_Y = a + bX + cX^2 + dX^3 + e([\text{Fe}/\text{H}])$, where *Y* is the filter listed above, and *X* is the specified color.

Table 4
Influence of Standard Model Parameter Values on Four Representative Stellar Models

Star	class ^c	Solar Composition ^a			Helium Abundance ^b			Mixing Length, α _{MLT} ^b			Opacity κ = 1.5κ ₀ ^b		
		T _{eff}	L/L _⊙	R/R _⊙	T _{eff}	L/L _⊙	R/R _⊙	T _{eff}	L/L _⊙	R/R _⊙	T _{eff}	L/L _⊙	R/R _⊙
Gl 411	PC–MP	0.0039	−0.0089	−0.0127	2630	0.0988	0.2160	13.07	−0.0002	−0.0044	−32.62	−0.0019	−0.0093
Gl 699	FC–MP	0.0054	0.0225	−0.0001	1614	0.0077	0.0187	5.055	0.0000	−0.0001
Gl 876	FC–MR	−0.0583	−0.2263	0.0109	1590	0.0355	0.1377	49.88	0.0004	−0.0046	−43.68	0.0000	0.0090
Gl 880	PC–MR	−0.0087	−0.0029	0.0157	4332	0.3518	0.4568	56.24	0.0011	−0.0011	−215.7	−0.0202	−0.0532

^a Total variation measured as a relative difference, $(x_{\text{GS98}} - x_{\text{AGSS09}})/x_{\text{GS98}}$, where *x* is one of the stellar parameters.

^b Quoted as a rate of change $\Delta x/\Delta q$, where *q* is the parameter being changed.

^c PC: partially convective; FC: fully convective; MP: metal-poor; MR: metal-rich.

Table 5
Parameters of All Stars in Our Sample

LG11/LSPM Name	CNS3	R.A. J2000	Dec.	F_{bol} 10^{-8} erg s $^{-1}$ cm $^{-2}$	$\sigma_{F_{\text{bol}}}$	T_{eff} K	$\sigma_{T_{\text{eff}}}$	R_* R_{\odot}	σ_{R_*}	M_* M_{\odot}	σ_{M_*}	[Fe/H]	$\sigma_{[\text{Fe}/\text{H}]}$	SpT
PM I00115+5908	...	00:11:31.8	+59:08:39	0.04210	0.00091	2864	60	0.1361	0.0061	0.100	0.010	-0.27	0.08	M6.1
PM I00118+2259	...	00:11:53.0	+22:59:04	0.1307	0.0017	3359	62	0.314	0.015	0.294	0.029	+0.13	0.08	M3.5
PM I00183+4401	Gl 15A	00:18:22.9	+44:01:22	5.669	0.045	3603	60	0.388	0.013	0.398	0.040	-0.30	0.08	M1.4
PM I00184+4401	Gl 15B	00:18:25.8	+44:01:38	0.891	0.010	3218	60	0.1923	0.0082	0.159	0.016	-0.30	0.08	M4.1
PM I00219-3124	GJ 1009	00:21:56.0	+31:24:21	0.4175	0.0035	3600	60	0.528	0.028	0.551	0.055	+0.27	0.08	M2.1
PM I01056+2829	GJ 1029	01:05:37.6	+28:29:33	0.06680	0.00091	2981	61	0.193	0.011	0.148	0.015	+0.14	0.08	M5.3
PM I01076+2257E	Gl 53.1B	01:07:38.5	+22:57:20	0.0675	0.0012	3232	60	0.308	0.013	0.276	0.028	+0.25	0.03	M4.0
PM I01125-1659	Gl 54.1	01:12:30.5	+16:59:56	0.5206	0.0082	3056	60	0.1680	0.0085	0.130	0.013	-0.26	0.08	M4.9
PM I01186-0052S	Gl 56.3 B	01:18:40.2	+00:52:27	0.3579	0.0042	3935	64	0.604	0.026	0.645	0.064	+0.01	0.08	K7.7
PM I01324-2154	GJ 3098	01:32:26.2	+21:54:18	0.3354	0.0044	3641	60	0.460	0.022	0.464	0.046	-0.20	0.08	M1.3
PM I01402+3147	GJ 3105	01:40:16.5	+31:47:30	0.07338	0.00085	3269	63	0.280	0.016	0.258	0.026	+0.06	0.08	M4.1
PM I01432+2750	GJ 3108	01:43:15.9	+27:50:31	0.5536	0.0051	3852	60	0.626	0.032	0.653	0.065	+0.25	0.08	M0.5
PM I01433+0419	Gl 70	01:43:20.1	+04:19:18	0.5422	0.0056	3458	60	0.414	0.017	0.401	0.040	-0.13	0.08	M2.5
PM I01510-0607	GJ 3119	01:51:04.0	+06:07:04	0.07207	0.00082	3011	61	0.1731	0.0078	0.132	0.013	-0.03	0.08	M5.1
PM I01528-2226	Gl 79	01:52:49.1	+22:26:05	2.117	0.020	3900	60	0.620	0.021	0.654	0.065	+0.14	0.08	M0.2
PM I02002+1303	Gl 83.1	02:00:12.9	+13:03:07	0.4275	0.0066	3080	60	0.187	0.010	0.144	0.014	-0.16	0.08	M4.9
PM I02123+0334	Gl 87	02:12:21.0	+03:34:33	0.9124	0.0074	3638	62	0.443	0.017	0.440	0.044	-0.36	0.08	M1.5
PM I02129+0000W	GJ 3142	02:12:54.5	+00:00:16	0.1060	0.0014	3257	60	0.277	0.014	0.251	0.025	+0.09	0.08	M4.1
PM I02164+1335	GJ 3146	02:16:29.8	+13:35:12	0.04532	0.00054	2829	60	0.1447	0.0091	0.103	0.010	-0.03	0.08	M6.1
PM I02171+3526	GJ 3147	02:17:10.0	+35:26:32	0.04153	0.00063	2880	60	0.1502	0.0067	0.113	0.011	+0.17	0.08	M5.8
PM I02190+2352	GJ 3150	02:19:02.3	+23:52:54	0.05432	0.00084	3216	60	0.273	0.015	0.235	0.023	-0.07	0.08	M4.7
PM I02222+4752	Gl 96	02:22:14.6	+47:52:48	1.490	0.016	3785	62	0.599	0.021	0.614	0.061	+0.14	0.08	M0.4
PM I02336+2455	Gl 102	02:33:37.1	+24:55:37	0.1772	0.0020	3199	62	0.204	0.012	0.174	0.017	-0.00	0.08	M4.4
PM I02358+2013	Gl 104	02:35:53.2	+20:13:11	0.6431	0.0057	3542	62	0.512	0.022	0.508	0.051	+0.12	0.08	M2.1
PM I02362+0652	Gl 105 B	02:36:15.2	+06:52:18	0.5005	0.0063	3284	60	0.278	0.010	0.246	0.025	-0.12	0.03	M4.0
PM I02441+4913W	...	02:44:10.2	+49:13:54	1.064	0.023	3685	60	0.498	0.017	0.521	0.052	+0.06	0.03	M1.7
PM I02442+2531	Gl 109	02:44:15.4	+25:31:24	0.9082	0.0080	3405	60	0.364	0.014	0.343	0.034	-0.10	0.08	M3.0
PM I02530+1652	...	02:53:00.8	+16:52:52	0.1655	0.0029	2800	60	0.1180	0.0052	0.0897	0.0090	-0.31	0.08	M7.0
PM I02534+1724	...	02:53:26.1	+17:24:32	0.1486	0.0013	3377	60	0.352	0.019	0.338	0.034	-0.16	0.08	M3.3
PM I02555+2652	Gl 118.2 C	02:55:35.7	+26:52:20	0.06832	0.00077	3227	60	0.347	0.015	0.309	0.031	+0.28	0.03	M3.8
PM I03047+6144	GJ 3195	03:04:43.4	+61:44:09	0.1320	0.0017	3500	61	0.424	0.016	0.415	0.042	-0.12	0.08	M3.0
PM I03181+3815	Gl 134	03:18:07.4	+38:15:07	0.7796	0.0066	3700	61	0.628	0.031	0.639	0.064	+0.53	0.08	M1.5
PM I03361+3118	...	03:36:08.6	+31:18:39	0.0902	0.0011	3086	60	0.233	0.012	0.189	0.019	+0.07	0.08	M4.7
PM I03526+1701	GJ 3253	03:52:41.7	+17:01:04	0.1116	0.0015	3079	60	0.2043	0.0092	0.166	0.017	+0.01	0.08	M4.7
LSPM J0355+5214	...	03:55:36.8	+52:14:29	0.02100	0.00026	3435	61	0.274	0.011	0.255	0.025	-0.35	0.05	M2.8
...	Gl 166 C	04:15:21.7	+07:39:17	0.874	0.012	3167	60	0.274	0.011	0.222	0.022	-0.21	0.08	M4.7
PM I04290+2155	Gl 169	04:29:00.0	+21:55:21	3.028	0.032	4124	62	0.687	0.023	0.744	0.074	+0.39	0.08	K7.7
PM I04376+5253	Gl 172	04:37:40.9	+52:53:37	2.480	0.021	3929	60	0.608	0.020	0.651	0.065	-0.11	0.08	K7.7
PM I04376-1102	Gl 173	04:37:41.8	+11:02:19	0.8354	0.0080	3671	61	0.444	0.017	0.472	0.047	-0.04	0.08	M2.0
PM I04429+1857	Gl 176	04:42:55.7	+18:57:29	1.254	0.011	3680	60	0.452	0.019	0.492	0.049	+0.14	0.08	M2.2
PM I04538-1746	Gl 180	04:53:49.9	+17:46:23	0.5257	0.0047	3506	60	0.421	0.019	0.413	0.041	-0.24	0.08	M2.1
PM I05019-0656	GJ 3323	05:01:57.4	+06:56:45	0.3994	0.0046	3143	60	0.2005	0.0079	0.161	0.016	-0.06	0.08	M4.5
PM I05033-1722	GJ 3325	05:03:20.0	+17:22:24	0.3526	0.0041	3365	60	0.284	0.013	0.262	0.026	-0.12	0.08	M3.2
PM I05314-0340	Gl 205	05:31:27.4	+03:40:38	6.340	0.054	3801	60	0.581	0.019	0.633	0.063	+0.49	0.08	M1.5
PM I05365+1119	Gl 208	05:36:30.9	+11:19:40	2.040	0.020	3966	60	0.601	0.020	0.646	0.065	+0.05	0.08	K7.9
PM I05415+5329	Gl 212	05:41:30.7	+53:29:23	1.205	0.017	3765	60	0.568	0.022	0.593	0.059	+0.19	0.03	M1.0
PM I05421+1229	Gl 213	05:42:09.1	+12:29:22	0.6002	0.0090	3250	60	0.264	0.011	0.229	0.023	-0.22	0.08	M4.0
PM I05557-2651	...	05:55:43.2	+26:51:23	0.6642	0.0072	3652	60	0.525	0.024	0.552	0.055	+0.31	0.08	M2.7
PM I06000+0242	GJ 3379	06:00:03.4	+02:42:23	0.777	0.012	3214	60	0.263	0.010	0.226	0.023	+0.07	0.08	M4.2
PM I06011+5935	GJ 3378	06:01:11.0	+59:35:49	0.4613	0.0085	3340	60	0.269	0.011	0.245	0.024	-0.09	0.08	M3.7
PM I06024+4951	GJ 3380	06:02:29.1	+49:51:56	0.0764	0.0012	3000	60	0.1635	0.0080	0.127	0.013	+0.01	0.08	M5.1
PM I06077-2544	...	06:07:43.7	+25:44:41	0.2913	0.0040	3356	60	0.321	0.015	0.294	0.029	-0.15	0.08	M3.2
PM I06140+5140	GJ 3388	06:14:02.3	+51:40:08	0.1280	0.0017	3326	60	0.284	0.013	0.251	0.025	-0.08	0.08	M3.4
PM I06246+2325	Gl 232	06:24:41.2	+23:25:58	0.1464	0.0020	3165	60	0.1948	0.0096	0.154	0.015	-0.18	0.08	M4.5
PM I06371+1733	Gl 239	06:37:10.8	+17:33:53	1.135	0.014	3801	60	0.423	0.015	0.471	0.047	-0.34	0.08	M0.2
PM I06461+3233	GJ 3408 B	06:46:07.4	+32:33:15	0.1313	0.0026	3656	62	0.419	0.019	0.432	0.043	-0.26	0.03	M0.9
PM I06490+3706	GJ 1092	06:49:05.4	+37:06:50	0.06770	0.00089	3207	61	0.201	0.011	0.163	0.016	-0.51	0.08	M4.3
PM I06523-0511	Gl 250 B	06:52:18.0	+05:11:24	1.180	0.020	3481	60	0.460	0.017	0.444	0.044	+0.14	0.03	M2.3
PM I06548+3316	Gl 251	06:54:48.9	+33:16:05	1.668	0.015	3448	60	0.358	0.013	0.352	0.035	-0.02	0.08	M3.2
PM I07232+4605	Gl 272	07:23:14.9	+46:05:14	0.5915	0.0057	3703	62	0.543	0.025	0.564	0.056	+0.05	0.08	M1.2
PM I07274+0513	Gl 273	07:27:24.4	+05:13:34	2.395	0.021	3317	60	0.315	0.012	0.283	0.028	-0.11	0.08	M3.8
PM I07287-0317	GJ 1097	07:28:45.4	+03:17:52	0.4392	0.0086	3448	60	0.404	0.019	0.397	0.040	-0.01	0.08	M3.1
PM I07344+6256	Gl 277.1	07:34:27.4	+62:56:29	0.5946	0.0086	3681	60	0.385	0.016	0.397	0.040	-0.37	0.08	M0.8
PM I07386-2113	GJ 3459	07:38:40.9	+21:13:28	0.3236	0.0054	3358	60	0.315	0.016	0.290	0.029	-0.18	0.08	M3.1
PM I07393+0211	Gl 281	07:39:23.0	+02:11:01	1.0739	0.0094	3771	60	0.626	0.025	0.633	0.063	+0.12	0.08	M0.3
PM I07482+2022	Gl 289	07:48:16.3	+20:22:05	0.2703	0.0024	3576	60	0.354	0.018	0.348	0.035	-0.45	0.08	M1.7
PM I08105-1348	Gl 297.2 B	08:10:34.2	+13:48:51	0.2480	0.0024	3544	62	0.523	0.019	0.513	0.051	-0.00	0.08	M2.5
PM I08161+0118	GJ 2066	08:16:07.9	+01:18:09	1.101	0.012	3500	60	0.461	0.017	0.452	0.045	-0.12	0.08	M2.2
PM I08298+2646	GJ 1111	08:29:49.3	+26:46:33	0.2016	0.0022	2800	60	0.1226	0.0056	0.0937	0.0094	-0.15	0.08	M6.7
PM I08526+2818	Gl 324B	08:52:40.8	+28:18:58	0.1645	0.0020	3166	61	0.273	0.013	0.238	0.024	+0.31	0.03	M4.1
PM I09143+5241	Gl 338A	09:14:22.8	+52:41:11	6.087	0.057	3920	60	0.550	0.026	0.607	0.061	-0.01	0.08	K7.8
PM I09319+3619	Gl 353	09:31:56.3	+36:19:13	0.7419	0.0068	3692	60	0.518	0.021	0.532	0.053	-0.20	0.08	M0.6
PM I09411+1312	Gl 361	09:41:10.3	+13:12:34	0.8004	0.0070	3500	60	0.485	0.019	0.470	0.047	-0.05	0.0	

Table 5 — Continued

LG11/LSPM Name	CNS3	R.A.	Dec.	F_{bol}	$\sigma_{F_{\text{bol}}}$	T_{eff}	$\sigma_{T_{\text{eff}}}$	R_*	σ_{R_*}	M_*	σ_{M_*}	[Fe/H]	$\sigma_{[\text{Fe}/\text{H}]}$	SpT
		J2000		10^{-8} erg s $^{-1}$ cm $^{-2}$		K		R_{\odot}		M_{\odot}				
PM I10196+1952	Gl 388	10:19:36.2	+19:52:12	2.940	0.035	3370	60	0.435	0.017	0.406	0.041	+0.15	0.08	M3.4
PM I10251-1013	Gl 390	10:25:10.8	+10:13:43	0.8767	0.0073	3700	60	0.497	0.020	0.520	0.052	-0.02	0.08	M1.5
PM I10289+0050	Gl 393	10:28:55.5	+00:50:27	1.612	0.013	3548	60	0.420	0.016	0.426	0.043	-0.18	0.08	M2.2
PM I10430-0912	...	10:43:02.9	+09:12:41	0.05641	0.00074	2951	60	0.198	0.010	0.152	0.015	-0.20	0.08	M5.5
PM I10508+0648	Gl 402	10:50:52.0	+06:48:29	0.5261	0.0055	3238	60	0.276	0.012	0.246	0.025	+0.16	0.08	M3.9
PM I10520+1359	Gl 403	10:52:04.2	+13:59:51	0.1567	0.0024	3298	62	0.295	0.016	0.265	0.027	-0.13	0.08	M3.6
PM I10522+0555	GJ 3631	10:52:14.2	+05:55:09	0.04934	0.00062	3039	60	0.1646	0.0076	0.128	0.013	+0.10	0.08	M5.4
PM I10564+0700	Gl 406	10:56:28.9	+07:00:53	0.5798	0.0069	2818	60	0.1348	0.0058	0.0997	0.0100	+0.25	0.08	M5.9
PM I11033+3558	Gl 411	11:03:20.2	+35:58:13	10.821	0.096	3563	60	0.389	0.013	0.386	0.039	-0.38	0.08	M1.9
PM I11054+4331	Gl 412A	11:05:28.7	+43:31:35	3.087	0.042	3619	60	0.383	0.013	0.390	0.039	-0.37	0.08	M1.1
PM I11055+4331	Gl 412B	11:05:30.9	+43:31:17	0.1311	0.0015	2863	60	0.1262	0.0054	0.0952	0.0095	-0.32	0.08	M6.6
PM I11311-1457	GJ 3668	11:31:08.3	+14:57:20	0.0774	0.0011	3109	62	0.1901	0.0085	0.154	0.015	-0.07	0.08	M4.5
PM I11417+4245	GJ 1148	11:41:44.6	+42:45:07	0.3942	0.0047	3304	61	0.376	0.018	0.336	0.034	+0.07	0.08	M3.8
PM I11421+2642	Gl 436	11:42:11.0	+26:42:24	0.8277	0.0093	3479	60	0.449	0.019	0.445	0.044	+0.01	0.08	M2.8
PM I11477+0048	Gl 447	11:47:44.3	+00:48:17	1.028	0.014	3192	60	0.1967	0.0077	0.168	0.017	-0.02	0.08	M4.3
PM I11509+4822	GJ 1151	11:50:57.7	+48:22:38	0.1681	0.0021	3118	60	0.1903	0.0091	0.154	0.015	+0.03	0.08	M4.5
PM I12100-1504	GJ 3707	12:10:05.5	+15:04:15	0.3499	0.0036	3385	60	0.390	0.018	0.387	0.039	+0.26	0.08	M3.8
PM I12151+4843	Gl 458.2	12:15:08.8	+48:43:57	0.4818	0.0044	3900	61	0.669	0.038	0.701	0.070	+0.14	0.08	M0.4
PM I12194+2822	Gl 459.3	12:19:24.1	+28:22:56	0.4705	0.0044	3993	60	0.643	0.037	0.703	0.070	+0.46	0.08	M0.6
PM I12312+0848	Gl 471	12:31:15.8	+08:48:38	1.0428	0.0089	3726	61	0.591	0.022	0.603	0.060	-0.04	0.08	M0.3
PM I12388+1141	Gl 480	12:38:52.4	+11:41:46	0.4368	0.0043	3463	60	0.466	0.025	0.467	0.047	+0.26	0.08	M3.4
PM I12507-0046	Gl 488	12:50:43.5	+00:46:05	2.721	0.021	3989	60	0.646	0.020	0.698	0.070	+0.24	0.08	K7.9
PM I13168+1700	Gl 505 B	13:16:51.5	+17:00:59	1.293	0.022	3709	60	0.539	0.019	0.541	0.054	-0.12	0.03	M0.7
PM I13196+3320	Gl 507.1	13:19:40.1	+33:20:47	0.6333	0.0051	3650	60	0.598	0.025	0.597	0.060	+0.40	0.08	M1.8
PM I13283-0221Ww	Gl 512A	13:28:21.0	+02:21:36	0.4762	0.0069	3498	60	0.461	0.024	0.461	0.046	+0.08	0.08	M3.1
PM I13299+1022	Gl 514	13:29:59.7	+10:22:38	2.206	0.018	3727	61	0.483	0.016	0.527	0.053	-0.09	0.08	M1.1
PM I13450+1747	Gl 525	13:45:05.0	+17:47:08	0.860	0.011	3828	60	0.494	0.017	0.526	0.053	-0.54	0.08	K7.7
PM I13457+1453	Gl 526	13:45:43.8	+14:53:29	4.013	0.053	3649	60	0.478	0.016	0.465	0.046	-0.31	0.08	M1.4
...	Gl 544 B	14:19:35.8	+05:09:08	0.02828	0.00041	3191	60	0.2032	0.0085	0.173	0.017	-0.18	0.03	M4.3
PM I14201-0937	Gl 545	14:20:07.3	+09:37:12	0.1403	0.0024	3341	60	0.276	0.012	0.256	0.026	-0.17	0.08	M3.7
PM I14251+5149	Gl 549 B	14:25:11.5	+51:49:53	0.3424	0.0054	3479	60	0.414	0.015	0.405	0.040	-0.11	0.08	M2.6
PM I14342-1231	Gl 555	14:34:16.8	+12:31:10	0.7984	0.0080	3211	60	0.310	0.013	0.273	0.027	+0.17	0.08	M4.0
PM I15118+3933	...	15:11:51.4	+39:33:02	0.05340	0.00061	3435	61	0.347	0.015	0.331	0.033	-0.09	0.03	M2.8
PM I15194-0743E	Gl 581	15:19:26.8	+07:43:20	0.9609	0.0077	3395	60	0.311	0.012	0.292	0.029	-0.15	0.08	M3.2
PM I15238+1727	Gl 585	15:23:51.1	+17:27:57	0.0976	0.0013	3164	60	0.187	0.011	0.152	0.015	-0.25	0.08	M4.5
PM I15354+6005	...	15:35:25.6	+60:05:07	0.0894	0.0013	3252	60	0.318	0.013	0.279	0.028	-0.01	0.08	M4.1
PM I16139+3346	Gl 615.2 C	16:13:56.2	+33:46:24	0.1764	0.0023	3454	63	0.437	0.020	0.423	0.042	-0.06	0.03	M2.8
PM I16254+5418	Gl 625	16:25:24.5	+54:18:14	1.087	0.012	3475	60	0.331	0.012	0.315	0.032	-0.35	0.08	M2.1
PM I16303-1239	Gl 628	16:30:18.0	+12:39:44	1.897	0.017	3272	60	0.325	0.012	0.294	0.029	-0.03	0.08	M3.6
PM I16509+2227	GJ 3976	16:50:57.9	+22:27:05	0.0934	0.0010	3054	60	0.1936	0.0097	0.151	0.015	-0.12	0.08	M4.9
PM I16542+1154	Gl 642	16:54:12.0	+11:54:52	0.3703	0.0033	3834	61	0.475	0.026	0.503	0.050	-0.48	0.08	M0.0
PM I16554-0819	Gl 643	16:55:25.2	+08:19:20	0.4005	0.0050	3279	60	0.233	0.011	0.204	0.020	-0.26	0.08	M3.2
PM I16555-0823	Gl 644 C	16:55:35.2	+08:23:40	0.04725	0.00100	2700	60	0.1131	0.0053	0.0841	0.0084	-0.07	0.08	M7.0
PM I16570-0420	GJ 1207	16:57:05.7	+04:20:55	0.2861	0.0046	3229	60	0.262	0.011	0.228	0.023	-0.09	0.08	M4.1
PM I16581+2544	Gl 649	16:58:08.8	+25:44:39	1.298	0.013	3700	60	0.507	0.018	0.534	0.053	+0.03	0.08	M1.3
PM I17095+4340	GJ 3991	17:09:31.5	+43:40:53	0.4951	0.0053	3284	60	0.286	0.012	0.266	0.027	+0.20	0.08	M3.9
PM I17115+3826	GJ 3992	17:11:34.7	+38:26:33	0.4094	0.0046	3432	61	0.384	0.017	0.375	0.037	+0.03	0.08	M3.4
PM I17198+4142	Gl 671	17:19:52.7	+41:42:50	0.3812	0.0040	3433	61	0.382	0.016	0.364	0.036	-0.15	0.08	M2.7
LSPM J1725+0206	Gl 673	17:25:45.2	+02:06:41	5.927	0.045	4124	60	0.649	0.020	0.706	0.071	+0.19	0.08	K7.4
PM I17303+0532	Gl 678.1A	17:30:22.7	+05:32:54	1.557	0.014	3675	60	0.543	0.019	0.549	0.055	-0.09	0.08	M0.5
PM I17355+6140	Gl 685	17:35:34.4	+61:40:53	0.928	0.011	3846	61	0.541	0.019	0.587	0.059	+0.10	0.08	M0.8
PM I17364+6820	Gl 687	17:36:25.9	+68:20:21	3.363	0.028	3439	60	0.414	0.015	0.405	0.041	+0.05	0.08	M3.2
PM I17378+1835	Gl 686	17:37:53.3	+18:35:29	1.418	0.014	3657	60	0.424	0.015	0.442	0.044	-0.25	0.08	M1.2
PM I17439+4322	Gl 694	17:43:55.9	+43:22:43	0.8927	0.0086	3464	61	0.440	0.017	0.430	0.043	+0.00	0.08	M2.6
PM I17578+0441N	Gl 699	17:57:48.5	+04:41:31	3.263	0.057	3228	60	0.1863	0.0071	0.155	0.015	-0.40	0.08	M4.2
PM I17578+4635	GJ 4040	17:57:50.9	+46:35:18	0.3310	0.0046	3470	60	0.396	0.018	0.400	0.040	+0.04	0.08	M3.2
PM I18007+2933	...	18:00:45.4	+29:33:56	0.1170	0.0017	3509	61	0.464	0.018	0.455	0.046	-0.06	0.03	M2.2
PM I18046+1354	...	18:04:38.7	+13:54:14	0.0780	0.0011	3375	61	0.273	0.011	0.247	0.025	-0.21	0.08	M3.0
PM I18051-0301	Gl 701	18:05:07.5	+03:01:52	1.720	0.014	3614	60	0.459	0.016	0.471	0.047	-0.22	0.08	M1.3
PM I18165+4533	Gl 709	18:16:31.0	+45:33:28	0.6393	0.0071	3785	60	0.557	0.021	0.583	0.058	-0.07	0.08	M0.6
PM I18363+1336S	GJ 4065	18:36:19.2	+13:36:26	0.2389	0.0029	3223	61	0.291	0.013	0.247	0.025	+0.04	0.08	M4.1
PM I18411+2447S	GJ 1230A	18:41:09.7	+24:47:14	0.431	0.014	3232	60	0.372	0.017	0.341	0.034	+0.24	0.08	M4.3
PM I18419+3149	GJ 4070	18:41:59.0	+31:49:49	0.4556	0.0060	3400	61	0.394	0.019	0.369	0.037	-0.16	0.08	M2.8
PM I18427+5937N	Gl 725A	18:42:46.7	+59:37:48	3.898	0.045	3441	60	0.351	0.013	0.334	0.033	-0.23	0.08	M3.0
PM I18427+5937S	Gl 725B	18:42:46.9	+59:37:35	2.245	0.038	3345	60	0.273	0.011	0.248	0.025	-0.30	0.08	M3.5
PM I18453+1851	...	18:45:22.9	+18:51:58	0.0876	0.0012	3214	60	0.2170	0.0087	0.184	0.018	-0.13	0.08	M4.4
PM I18498-2350	Gl 729	18:49:49.3	+23:50:10	1.451	0.017	3240	60	0.2008	0.0076	0.170	0.017	-0.18	0.08	M4.1
PM I18580+0554	Gl 740	18:58:00.1	+05:54:29	1.698	0.015	3834	60	0.570	0.020	0.604	0.060	+0.14	0.08	M0.7
PM I19070+2053	Gl 745A	19:07:05.5	+20:53:17	0.5715	0.0066	3500	60	0.310	0.012	0.296	0.030	-0.33	0.08	M2.1
PM I19072+2052	Gl 745B	19:07:13.2	+20:52:37	0.584	0.010	3494	62	0.323	0.014	0.303	0.030	-0.35	0.08	M2.1
PM I19169+0510	Gl 752A	19:16:55.2	+05:10:08	3.017	0.023	3558	60	0.474	0.016	0.475	0.047	+0.10	0.08	M2.6
PM I19220+0702	GJ 1236	19:22:02.0	+07:02:30	0.1829	0.0024	3335	61	0.2338	0.0093	0.206	0.021	-0.29	0.08	M3.3
PM I19321-1119	...	19:32:08.1	+11:19:57	0.06578	0.00096	3211	60	0.258	0.0					

Table 5 — *Continued*

LG11/LSPM Name	CNS3	R.A. J2000	Dec.	F_{bol} $10^{-8} \text{ erg s}^{-1} \text{ cm}^{-2}$	$\sigma_{F_{\text{bol}}}$	T_{eff} K	$\sigma_{T_{\text{eff}}}$	R_* R_{\odot}	σ_{R_*}	M_* M_{\odot}	σ_{M_*}	[Fe/H]	$\sigma_{[\text{Fe}/\text{H}]}$	SpT
PM I20525-1658	...	20:52:33.0	+16:58:29	0.659	0.013	3205	60	0.266	0.012	0.224	0.022	-0.02	0.08	M4.0
PM I20533+6209	Gl 809	20:53:19.7	+62:09:16	3.348	0.036	3791	60	0.529	0.017	0.581	0.058	-0.06	0.08	M1.0
PM I20567-1026	Gl 811.1	20:56:46.6	+10:26:54	0.3720	0.0038	3473	61	0.456	0.028	0.452	0.045	+0.16	0.08	M2.8
LSPM J2106+3844S	Gl 820B	21:06:55.2	+38:44:31	22.25	0.19	4021	74	0.602	0.023	0.641	0.064	-0.22	0.08	K7.3
PM I21092-1318	Gl 821	21:09:17.4	+13:18:08	0.4185	0.0051	3545	60	0.369	0.016	0.356	0.036	-0.45	0.08	M1.4
PM I21518+4220E	Gl 838.3 B	21:51:53.8	+42:20:39	0.2096	0.0039	3771	61	0.557	0.023	0.579	0.058	-0.07	0.08	M0.5
PM I22021+0124	Gl 846	22:02:10.2	+01:24:00	1.791	0.015	3848	60	0.546	0.019	0.590	0.059	+0.02	0.08	M0.6
PM I22096-0438	Gl 849	22:09:40.3	+04:38:26	1.192	0.010	3530	60	0.470	0.018	0.482	0.048	+0.37	0.08	M3.1
PM I22160+5439	GJ 4269	22:16:02.5	+54:39:59	0.05621	0.00094	3226	63	0.289	0.012	0.246	0.025	-0.04	0.08	M4.1
PM I22290+0139	...	22:29:05.8	+01:39:48	0.4854	0.0046	3903	60	0.575	0.030	0.620	0.062	+0.13	0.08	M0.4
PM I22361-0050	Gl 864	22:36:09.6	+00:50:29	0.8303	0.0072	3916	61	0.600	0.026	0.644	0.064	+0.07	0.08	M0.6
PM I22503-0705	Gl 875	22:50:19.4	+07:05:24	0.8949	0.0081	3740	61	0.563	0.024	0.578	0.058	+0.02	0.08	M0.2
PM I22532-1415	Gl 876	22:53:16.6	+14:15:48	1.916	0.015	3247	60	0.363	0.014	0.328	0.033	+0.17	0.08	M3.7
PM I22565+1633	Gl 880	22:56:34.8	+16:33:12	3.545	0.027	3720	60	0.549	0.018	0.574	0.057	+0.21	0.08	M1.5
...	Gl 887	23:05:52.0	+35:51:11	10.89	0.17	3688	86	0.468	0.022	0.495	0.049	-0.06	0.08	M1.1
PM I23099+1425W	...	23:09:54.8	+14:25:35	0.5017	0.0052	4013	62	0.643	0.022	0.680	0.068	-0.05	0.08	K7.4
PM I23182+4617	Gl 894.1	23:18:17.9	+46:17:21	0.3811	0.0034	3910	60	0.589	0.035	0.644	0.064	+0.13	0.08	M0.7
PM I23216+1717	GJ 4333	23:21:37.4	+17:17:26	0.5040	0.0057	3324	60	0.416	0.020	0.391	0.039	+0.24	0.08	M3.9
PM I23245+5751S	Gl 895	23:24:30.5	+57:51:15	1.0011	0.0093	3764	60	0.539	0.020	0.585	0.058	+0.31	0.08	M1.4
PM I23318+1956W	Gl 896A	23:31:52.1	+19:56:14	1.592	0.033	3353	60	0.409	0.016	0.379	0.038	+0.03	0.08	M3.8
PM I23318+1956E	Gl 896B	23:31:52.5	+19:56:13	0.617	0.018	3072	60	0.303	0.013	0.240	0.024	+0.03	0.08	M4.9
PM I23419+4410	Gl 905	23:41:55.0	+44:10:38	0.759	0.012	2930	60	0.1894	0.0079	0.145	0.015	+0.23	0.08	M5.2
PM I23428+3049	GJ 1288	23:42:52.7	+30:49:21	0.05956	0.00072	3113	60	0.1864	0.0086	0.149	0.015	-0.12	0.08	M4.7
PM I23431+3632	GJ 1289	23:43:06.3	+36:32:13	0.2518	0.0045	3173	60	0.238	0.013	0.202	0.020	+0.05	0.08	M4.3
PM I23492+0224	Gl 908	23:49:12.4	+02:24:04	2.362	0.019	3646	60	0.407	0.014	0.408	0.041	-0.45	0.08	M1.4
PM I23505-0933	GJ 4367	23:50:31.5	+09:33:32	0.1196	0.0025	3221	60	0.315	0.015	0.275	0.027	+0.37	0.08	M3.9

Table 6
Synthetic Photometry of All Stars in Our Sample

Name	V	σ	R_C	σ	I_C	σ	g	σ	r	σ	i	σ	z	σ	J	σ	H	σ	K_S	σ	Gaia G	σ
PM I00115+5908	15.611	0.040	13.926	0.012	11.805	0.020	16.325	0.024	14.953	0.011	12.703	0.013	11.594	0.014	9.957	0.018	9.405	0.017	9.075	0.020	13.827	0.014
PM I00118+2259	12.958	0.016	11.780	0.013	10.253	0.020	13.834	0.021	12.362	0.011	11.010	0.013	10.263	0.013	8.861	0.017	8.267	0.017	8.016	0.020	12.024	0.014
PM I00183+4401	8.119	0.016	7.116	0.012	5.991	0.020	8.973	0.020	7.505	0.011	6.638	0.012	6.148	0.013	4.896	0.017	4.303	0.017	4.039	0.020	7.523	0.014
PM I00184+4401	11.007	0.016	9.723	0.012	8.128	0.020	11.993	0.021	10.327	0.011	9.811	0.013	8.134	0.013	6.745	0.017	6.211	0.017	5.940	0.020	9.953	0.014
PM I00219-3124	11.175	0.016	10.142	0.013	8.910	0.020	11.956	0.021	10.577	0.011	9.583	0.013	9.036	0.013	7.713	0.017	7.025	0.017	6.753	0.020	10.500	0.014
PM I01056+2829	14.820	0.018	13.297	0.013	11.361	0.020	15.740	0.023	14.153	0.011	12.260	0.013	11.152	0.013	9.477	0.017	8.882	0.017	8.588	0.020	13.311	0.014
PM I01076+2257E	14.054	0.016	12.770	0.012	11.095	0.020	14.899	0.021	13.438	0.011	11.904	0.013	11.038	0.013	9.538	0.017	8.935	0.017	8.662	0.020	12.937	0.014
PM I01125-1659	12.082	0.016	10.662	0.012	8.866	0.020	13.021	0.021	11.399	0.011	9.710	0.013	8.789	0.013	7.285	0.017	6.751	0.017	6.441	0.020	10.780	0.014
PM I01186-0052S	10.699	0.016	9.800	0.013	8.942	0.020	11.455	0.021	10.110	0.011	9.510	0.013	9.160	0.013	8.032	0.017	7.385	0.017	7.156	0.020	10.271	0.014
PM I01324-2154	11.200	0.016	10.195	0.012	9.056	0.020	12.010	0.020	10.595	0.011	9.705	0.013	9.210	0.013	7.938	0.017	7.364	0.017	7.166	0.020	10.592	0.014
PM I01402+3147	13.954	0.017	12.728	0.013	11.054	0.020	14.700	0.023	13.392	0.011	11.862	0.013	10.982	0.013	9.443	0.017	8.813	0.017	8.546	0.020	12.884	0.014
PM I01432+2750	10.402	0.016	9.473	0.013	8.519	0.020	11.192	0.020	9.807	0.011	9.113	0.012	8.724	0.013	7.493	0.017	6.800	0.017	6.628	0.020	9.923	0.014
PM I01433+0419	10.931	0.016	9.868	0.013	8.569	0.020	11.752	0.021	10.337	0.011	9.253	0.012	8.700	0.013	7.393	0.017	6.800	0.017	6.537	0.020	10.210	0.014
PM I01510-0607	14.444	0.020	12.986	0.013	11.111	0.020	15.410	0.028	13.783	0.012	11.979	0.013	10.988	0.013	9.408	0.017	8.556	0.017	8.553	0.020	13.051	0.014
PM I01528-2226	8.929	0.016	7.976	0.012	7.105	0.020	9.697	0.020	8.318	0.011	7.611	0.013	7.218	0.013	6.055	0.017	5.415	0.017	5.202	0.020	8.426	0.014
PM I02002+1303	12.285	0.016	10.857	0.012	9.068	0.020	13.228	0.021	11.594	0.011	9.910	0.013	8.990	0.013	7.497	0.017	6.949	0.017	6.688	0.020	10.979	0.014
PM I02123+0334	10.062	0.016	9.085	0.012	7.944	0.020	10.848	0.020	9.482	0.011	8.596	0.013	8.090	0.013	6.858	0.017	6.312	0.017	6.124	0.020	9.472	0.014
PM I02129+0000W	13.535	0.017	12.204	0.013	10.527	0.020	14.430	0.022	12.883	0.011	11.329	0.013	10.500	0.013	9.054	0.017	8.489	0.017	8.165	0.020	12.385	0.014
PM I02164+1335	15.758	0.018	14.002	0.013	11.837	0.020	16.734	0.024	15.072	0.011	12.811	0.013	11.559	0.013	9.858	0.017	9.316	0.017	8.988	0.020	13.688	0.014
PM I02171+3526	15.850	0.040	14.205	0.013	12.103	0.020	16.527	0.025	15.205	0.040	13.063	0.013	11.811	0.014	9.974	0.017	9.352	0.017	9.007	0.020	14.085	0.014
PM I02190+2352	14.127	0.017	12.810	0.013	11.193	0.020	15.137	0.023	13.438	0.011	11.971	0.013	11.208	0.013	9.798	0.017	9.219	0.017	8.941	0.020	13.033	0.014
PM I02222+4752	9.413	0.016	8.446	0.013	7.427	0.020	10.196	0.021	8.806	0.011	8.036	0.013	7.611	0.013	6.392	0.017	5.738	0.017	5.563	0.020	8.878	0.014
PM I02336+2455	13.046	0.017	11.703	0.013	10.005	0.020	13.997	0.023	12.381	0.011	10.817	0.013	9.968	0.013	8.493	0.017	7.903	0.017	7.606	0.020	11.875	0.014
PM I02358+2013	10.655	0.016	9.629	0.013	8.412	0.020	11.478	0.021	10.059	0.011	9.079	0.013	8.542	0.014	7.244	0.017	6.587	0.017	6.354	0.020	9.997	0.014
PM I02362+0652	11.070	0.016	10.442	0.012	8.835	0.020	12.546	0.021	11.070	0.011	9.619	0.013	8.804	0.013	7.356	0.017	6.811	0.017	6.562	0.020	10.644	0.014
PM I02441+4913W	9.987	0.016	8.975	0.012	7.815	0.020	10.824	0.020	9.381	0.011	8.468	0.013	7.961	0.013	6.713	0.017	6.105	0.017	5.857	0.020	9.366	0.014
PM I02442+2531	10.599	0.016	9.482	0.012	8.087	0.020	11.428	0.021	9.989	0.011	8.807	0.013	8.156	0.013	6.785	0.017	6.196	0.017	5.965	0.020	9.783	0.014
PM I02530+1652	15.133	0.022	13.054	0.013	10.650	0.020	16.006	0.033	14.473	0.012	11.706	0.013	10.257	0.013	8.409	0.017	7.881	0.017	7.500	0.020	12.723	0.014
PM I02534+1724	12.694	0.016	11.552	0.013	10.123	0.020	13.608	0.021	12.073	0.011	10.855	0.013	10.178	0.013	8.746	0.017	8.102	0.017	7.857	0.020	11.848	0.014
PM I02555+2652	13.827	0.016	12.661	0.012	11.001	0.020	14.675	0.021	13.224	0.011	11.784	0.012	10.986	0.013	9.547	0.017	8.954	0.017	8.663	0.020	12.808	0.014
PM I03047+6144	12.564	0.016	11.496	0.012	10.126	0.020	13.380	0.021	11.995	0.011	10.838	0.013	10.209	0.013	8.896	0.017	8.355	0.017	8.091	0.020	11.799	0.014
PM I03181+3815	10.284	0.016	9.283	0.013	8.167	0.020	11.100	0.021	9.674	0.011	8.807	0.013	8.332	0.013	7.080	0.017	6.395	0.017	6.156	0.020	9.689	0.014
PM I03361+3118	13.995	0.016	12.638	0.013	10.851	0.020	14.864	0.022	13.365	0.011	11.697	0.013	10.762	0.014	9.194	0.017	8.606	0.017	8.306	0.020	12.746	0.014
PM I03526+1701	13.775	0.016	12.383	0.012	10.596	0.020	14.721	0.021	13.123	0.011	11.440	0.013	10.520	0.013	8.964	0.017	8.373	0.017	8.054	0.020	12.505	0.014
LSPM J0355+5214	14.508	0.016	13.418	0.013	12.100	0.020	15.435	0.021	13.885	0.011	12.802	0.013	12.198	0.014	10.900	0.017	10.339	0.017	10.101	0.020	13.763	0.014
GH166C	11.230	0.016	9.947	0.012	8.221	0.020	12.078	0.021	10.638	0.011	9.042	0.013	8.163	0.013	6.708	0.017	6.219	0.017	5.975	0.020	10.087	0.014
PM I04290+2155	8.355	0.016	7.462	0.013	6.631	0.020	9.070	0.020	7.762	0.011	7.187	0.012	6.871	0.013	5.698	0.017	5.044	0.017	4.853	0.020	7.934	0.014
PM I04376+5253	8.627	0.016	7.730	0.012	6.881	0.020	9.395	0.020	8.037	0.011	7.444	0.012	7.119	0.013	5.908	0.017	5.214	0.017	5.031	0.020	8.207	0.014
PM I04376-1102	10.346	0.016	9.319	0.012	8.107	0.020	11.147	0.021	9.747	0.011	8.774	0.012	8.235	0.013	6.949	0.017	6.345	0.017	6.094	0.020	9.688	0.014
PM I04429+1857	9.993	0.016	8.949	0.012	7.699	0.020	10.813	0.020	9.391	0.011	8.380	0.013	7.787	0.013	6.485	0.017	5.841	0.017	5.603	0.020	9.302	0.014
PM I04538-1746	10.910	0.016	9.864	0.012	8.624	0.020	11.748	0.021	10.298	0.011	9.302	0.013	8.728	0.013	7.426	0.017	6.842	0.017	6.597	0.020	10.226	0.014
PM I05019-0656	12.135	0.016	10.788	0.013	9.082	0.020	13.057	0.022	11.468	0.011	9.898	0.013	9.055	0.013	7.594	0.017	7.034	0.017	6.783	0.020	10.959	0.014
PM I05033-1722	11.763	0.016	10.569	0.013	9.089	0.020	12.630	0.021	11.116	0.011	9.838	0.013	9.127	0.013	7.788	0.017	7.249	0.017	6.973	0.020	10.842	0.014
PM I05314-0340	7.932	0.016	7.008	0.013	5.931	0.020	8.767	0.020	7.376	0.011	6.566	0.012	6.096	0.013	4.796	0.017	4.123	0.017	3.856	0.020	7.416	0.014
PM I05365+1119	8.865	0.016	7.962	0.012	7.087	0.020	9.632	0.021	8.276	0.011	7.656	0.012	7.309	0.013	6.103	0.017	5.423	0.017	5.285	0.020	8.430	0.014
PM I05415+5329	9.739	0.016	8.754	0.012	7.667	0.020	10.512	0.021	9.134	0.011	8.299	0.013	7.829	0.013	6.609	0.017	5.983	0.017	5.755	0.020	9.163	0.014
PM I05421+1229	11.580	0.016	10.264	0.012	8.621	0.020	12.440	0.021	10.918	0.011	9.413	0.013	8.605	0.013	7.161	0.017	6.613	0.017	6.355	0.020	10.460	0.014
PM I05557-2651	10.795	0.016	9.730	0.012	8.413	0.020	11.585	0.021	10.209	0.011	9.108	0.013	8.506	0.014	7.183	0.017	6.518	0.017	6.290	0.020	10.055	0.014
PM I06000-0242	11.281	0.016	10.019	0.012	8.386	0.020	12.187	0.021	10.648	0.011	9.183	0.013	8.364	0.013								

Table 6 — Continued

Name	V	σ	R_C	σ	I_C	σ	g	σ	r	σ	i	σ	z	σ	J	σ	H	σ	K_S	σ	Gaia G	σ
GJ 544 B	14.905	0.016	13.668	0.013	12.009	0.020	15.749	0.022	14.320	0.011	12.813	0.013	11.964	0.013	10.479	0.017	9.904	0.017	9.601	0.020	13.844	0.014
PM 114201-0937	12.932	0.016	11.746	0.012	10.207	0.020	13.787	0.021	12.329	0.011	10.971	0.013	10.205	0.013	8.767	0.017	8.192	0.017	7.925	0.020	11.980	0.014
PM 114251+5149	11.467	0.016	10.423	0.013	9.104	0.020	12.291	0.021	10.894	0.011	9.801	0.013	9.204	0.013	7.875	0.017	7.277	0.017	7.037	0.020	10.751	0.014
PM 114342-1231	11.338	0.016	10.063	0.013	8.415	0.020	12.182	0.021	10.717	0.011	9.213	0.013	8.369	0.013	6.861	0.017	6.240	0.017	5.980	0.019	10.246	0.014
PM 115118+3933	13.569	0.016	12.483	0.013	11.143	0.020	14.451	0.021	12.963	0.011	11.847	0.013	11.223	0.013	9.867	0.017	9.291	0.017	9.052	0.020	12.810	0.014
PM 115194-0743E	10.581	0.016	9.448	0.012	8.024	0.020	11.438	0.021	9.970	0.011	8.754	0.013	8.083	0.013	6.716	0.017	6.132	0.017	5.897	0.020	9.740	0.014
PM 115238+1727	13.714	0.016	12.370	0.012	10.636	0.020	14.623	0.021	13.077	0.011	11.460	0.013	10.562	0.013	9.087	0.017	8.593	0.017	8.305	0.020	12.513	0.014
PM 115354+6005	13.426	0.016	12.226	0.012	10.654	0.020	14.211	0.021	12.813	0.011	11.433	0.013	10.662	0.013	9.256	0.017	8.694	0.017	8.426	0.020	12.441	0.014
PM 116139+3346	12.251	0.016	11.164	0.013	9.825	0.020	13.091	0.021	11.647	0.011	10.531	0.013	9.915	0.014	8.589	0.017	8.000	0.017	7.743	0.020	11.489	0.014
PM 116254+5418	10.123	0.016	9.062	0.013	7.821	0.020	11.010	0.021	9.492	0.011	8.502	0.013	7.916	0.013	6.625	0.017	6.069	0.017	5.836	0.020	9.429	0.014
PM 116303-1239	10.097	0.016	8.893	0.012	7.332	0.020	10.912	0.020	9.494	0.011	8.102	0.012	7.337	0.013	5.952	0.017	5.386	0.017	5.080	0.020	9.118	0.014
PM 116509+2227	14.027	0.017	12.582	0.013	10.747	0.020	14.957	0.022	13.360	0.011	11.602	0.013	10.660	0.013	9.139	0.017	8.602	0.017	8.265	0.020	12.678	0.014
PM 116542+1154	10.755	0.016	9.834	0.013	8.911	0.020	11.555	0.021	10.165	0.011	9.499	0.013	9.107	0.013	7.914	0.017	7.327	0.017	7.157	0.020	10.293	0.014
PM 116554-0819	11.772	0.016	10.547	0.012	9.056	0.020	12.709	0.021	11.093	0.011	9.816	0.013	9.067	0.013	7.623	0.017	7.051	0.017	6.796	0.020	10.819	0.014
PM 116555-0823	16.758	0.017	14.577	0.013	12.127	0.020	17.662	0.024	16.019	0.011	13.212	0.013	11.690	0.013	9.777	0.017	9.197	0.017	8.832	0.019	14.204	0.014
PM 116570-0420	12.277	0.016	11.052	0.012	9.444	0.020	13.146	0.021	11.663	0.011	10.233	0.013	9.428	0.013	7.981	0.017	7.411	0.017	7.125	0.020	11.255	0.014
PM 116581+2544	9.667	0.016	8.696	0.012	7.602	0.020	10.476	0.020	9.078	0.011	8.236	0.013	7.767	0.013	6.495	0.017	5.875	0.017	5.634	0.020	9.105	0.014
PM 117095+4340	11.855	0.016	10.590	0.012	8.927	0.020	12.638	0.021	11.250	0.011	9.737	0.013	8.876	0.013	7.397	0.017	6.759	0.017	6.477	0.020	10.759	0.014
PM 117115+3826	11.602	0.016	10.459	0.012	8.981	0.020	12.389	0.021	11.012	0.011	9.725	0.013	9.013	0.013	7.644	0.017	7.044	0.017	6.795	0.020	10.718	0.014
PM 117198+4142	11.422	0.016	10.341	0.012	9.003	0.020	12.240	0.021	10.817	0.011	9.711	0.013	9.076	0.013	7.743	0.017	7.162	0.017	6.922	0.020	10.661	0.014
LSPM J1725+0206	7.510	0.016	6.680	0.012	5.913	0.020	8.306	0.020	6.956	0.011	6.456	0.012	6.158	0.013	4.961	0.017	4.315	0.017	4.183	0.020	7.167	0.014
PM 117303+0532	9.334	0.016	8.373	0.013	7.383	0.020	10.138	0.021	8.722	0.011	7.990	0.013	7.580	0.013	6.307	0.017	5.704	0.017	5.486	0.020	8.819	0.014
PM 117355+6140	10.001	0.016	8.993	0.013	7.897	0.020	10.778	0.021	9.379	0.011	8.533	0.013	8.076	0.013	6.908	0.017	6.293	0.017	6.054	0.020	9.407	0.014
PM 117364+6820	9.182	0.016	8.098	0.012	6.682	0.020	9.986	0.020	8.617	0.011	7.411	0.013	6.725	0.013	5.348	0.017	4.782	0.017	4.504	0.020	8.379	0.014
PM 117378+1835	9.603	0.016	8.595	0.012	7.498	0.020	10.464	0.020	8.978	0.011	8.136	0.012	7.653	0.013	6.382	0.017	5.816	0.017	5.560	0.020	9.013	0.014
PM 117439+4322	10.511	0.016	9.424	0.012	8.100	0.020	11.319	0.020	9.900	0.011	8.799	0.012	8.189	0.013	6.845	0.017	6.211	0.017	5.972	0.019	9.752	0.014
PM 117578+0441N	9.527	0.016	8.315	0.012	7.130	0.020	10.428	0.020	8.913	0.011	7.508	0.013	6.734	0.013	5.296	0.017	4.801	0.017	4.533	0.020	8.537	0.014
PM 117578+4635	11.770	0.016	10.633	0.012	9.196	0.020	12.599	0.021	11.167	0.011	9.928	0.012	9.250	0.013	7.887	0.017	7.281	0.017	6.996	0.020	10.916	0.014
PM 118007+2933	12.538	0.016	11.501	0.013	10.250	0.020	13.316	0.021	11.945	0.011	10.927	0.013	10.375	0.013	9.073	0.017	8.459	0.017	8.218	0.020	11.853	0.014
PM 118046+1354	13.227	0.016	12.101	0.012	10.717	0.020	14.074	0.021	12.600	0.011	11.436	0.013	10.789	0.013	9.443	0.017	8.888	0.017	8.652	0.019	12.411	0.014
PM 118051-0301	9.389	0.016	8.399	0.013	7.308	0.020	10.207	0.020	8.779	0.011	7.942	0.012	7.464	0.013	6.180	0.017	5.588	0.017	5.322	0.020	8.812	0.014
PM 118165+4533	10.296	0.016	9.340	0.013	8.348	0.020	11.086	0.020	9.691	0.011	8.953	0.012	8.542	0.013	7.321	0.017	6.664	0.017	6.471	0.020	9.782	0.014
PM 118363+1336S	12.477	0.016	11.190	0.013	9.591	0.020	13.368	0.022	11.820	0.011	10.356	0.013	9.594	0.013	8.176	0.017	7.609	0.017	7.371	0.020	11.411	0.014
PM 118411+2447S	12.205	0.016	10.856	0.013	9.116	0.020	13.173	0.021	11.569	0.011	9.946	0.013	9.050	0.013	7.511	0.017	6.898	0.017	6.611	0.020	11.002	0.014
PM 118419+3149	11.358	0.016	10.173	0.012	8.782	0.020	12.359	0.021	10.680	0.011	9.502	0.013	8.859	0.013	7.527	0.017	6.968	0.017	6.723	0.020	10.501	0.014
PM 118427+5937N	8.897	0.016	7.835	0.012	6.471	0.020	9.734	0.020	8.324	0.011	7.184	0.013	6.548	0.013	5.198	0.017	4.642	0.017	4.406	0.020	8.143	0.014
PM 118427+5937S	9.733	0.016	8.604	0.013	7.130	0.020	10.559	0.021	9.147	0.011	7.874	0.012	7.166	0.013	5.748	0.017	5.211	0.017	4.958	0.020	8.865	0.014
PM 118453+1851	13.727	0.017	12.413	0.013	10.738	0.020	14.661	0.023	13.068	0.011	11.547	0.013	10.713	0.013	9.259	0.017	8.674	0.017	8.416	0.020	12.595	0.014
PM 118498-2350	10.528	0.016	9.229	0.012	7.619	0.020	11.411	0.021	9.842	0.011	8.404	0.013	7.623	0.013	6.225	0.017	5.661	0.017	5.394	0.020	9.446	0.014
PM 118580+0554	9.247	0.016	8.290	0.012	7.288	0.020	10.036	0.020	8.642	0.011	7.897	0.013	7.464	0.013	6.257	0.017	5.620	0.017	5.416	0.020	8.726	0.014
PM 119070+2053	10.780	0.016	9.725	0.012	8.499	0.020	11.634	0.021	10.152	0.011	9.175	0.012	8.611	0.013	7.321	0.017	6.781	0.017	6.552	0.020	10.096	0.014
PM 119072+2052	10.736	0.016	9.650	0.013	8.433	0.020	11.645	0.021	10.078	0.011	9.102	0.013	8.560	0.013	7.291	0.017	6.770	0.017	6.564	0.020	10.035	0.014
PM 119169+0510	9.141	0.016	8.077	0.012	6.744	0.020	9.940	0.020	8.553	0.011	7.454	0.013	6.813	0.013	5.543	0.017	4.917	0.017	4.696	0.020	8.394	0.014
PM 119220+0702	12.388	0.016	11.223	0.012	9.790	0.020	13.299	0.021	11.738	0.011	10.527	0.013	9.850	0.013	8.509	0.017	7.966	0.017	7.706	0.020	11.520	0.014
PM 119321-1119	13.894	0.016	12.662	0.013	11.036	0.020	14.682	0.021	13.287	0.011	11.832	0.013	11.036	0.014	9.578	0.017	8.950	0.017	8.720	0.020	12.858	0.014
PM 119539+4424E	13.957	0.016	12.273	0.012	10.178	0.020	14.896	0.022	13.275	0.011	11.121	0.013	9.937	0.014	8.260	0.017	7.721	0.017	7.405	0.020	12.189	0.014
PM 120034+2951	14.405	0.018	13.082	0.013	11.292	0.020	15.213	0.023	13.832	0.011	12.139	0.013	11.170	0.013	9.584	0.017	9.013	0.017	8.697	0.020	13.178	0.014
PM 120112+1611	13.991	0.016	12.760	0.013	11.127	0.020	14.786	0.021	13.403	0.011	11.290	0.013	11.089	0.013	9.642	0.017	9.123	0.017	8.857	0.020	12.942	0.014
PM 120167+5017	12.961	0.016	11.906	0.012	10.578	0.020	13.															

Table 7
Inferred stellar evolution model parameters and associated errors.[†]

LG11/LSPM Name	CNS3	Mass (M_{\odot})	σ_M	log(age) (yr)	σ_{age}	F_{bol} ($10^{-8} \text{ erg s}^{-1} \text{ cm}^{-2}$)	$\sigma_{F_{\text{bol}}}$	δF_{bol}	T_{eff} (K)	σ_T	δT_{eff}	Radius (R_{\odot})	σ_R	δR	χ^2
PM I00115+5908	...	0.107	0.009	9.46	0.59	0.04237	0.00138	-0.00636	2921	32	-0.020	0.130	0.003	0.043	1.935
PM I00118+2259	...	0.312	0.016	9.43	0.60	0.13054	0.00271	0.00130	3376	35	-0.005	0.309	0.012	0.016	0.197
PM I00183+4401	Gl 15A	0.406	0.009	9.48	0.56	5.67125	0.06996	-0.00043	3626	32	-0.006	0.382	0.007	0.015	0.345
PM I00184+4401	Gl 15B	0.169	0.006	9.44	0.59	0.88968	0.01519	0.00114	3250	32	-0.010	0.187	0.005	0.026	0.692
PM I00219-3124	GJ 1009	0.538	0.019	9.46	0.52	0.41856	0.00521	-0.00265	3657	45	-0.016	0.507	0.019	0.041	1.646
PM I01056+2829	GJ 1029	0.153	0.009	9.33	0.62	0.06661	0.00136	0.00272	3084	33	-0.034	0.178	0.007	0.078	4.961
PM I01125-1659	Gl 54.1	0.136	0.005	9.40	0.62	0.51956	0.01213	0.00202	3132	31	-0.025	0.159	0.006	0.055	2.817
PM I01186-0052S	Gl 56.3 B	0.611	0.018	9.53	0.53	0.35883	0.00645	-0.00262	4012	51	-0.019	0.579	0.015	0.042	2.593
PM I01324-2154	GJ 3098	0.468	0.017	9.41	0.60	0.33581	0.00653	-0.00109	3708	35	-0.019	0.440	0.016	0.042	2.097
PM I01402+3147	GJ 3105	0.258	0.016	9.47	0.60	0.07336	0.00126	0.00028	3333	36	-0.019	0.267	0.013	0.046	1.754
PM I01432+2750	GJ 3108	0.628	0.019	9.46	0.50	0.55509	0.00731	-0.00268	3935	58	-0.022	0.592	0.018	0.055	3.170
PM I01433+0419	Gl 70	0.409	0.013	9.46	0.59	0.54141	0.00836	0.00148	3578	29	-0.035	0.385	0.011	0.070	6.824
PM I01510-0607	GJ 3119	0.138	0.004	9.35	0.59	0.07203	0.00126	0.00064	3089	29	-0.026	0.164	0.004	0.054	3.117
PM I01528-2226	Gl 79	0.629	0.015	9.49	0.50	2.12160	0.02975	-0.00207	3987	39	-0.022	0.593	0.012	0.043	3.900
PM I02002+1303	Gl 83.1	0.152	0.009	9.34	0.62	0.42641	0.00978	0.00263	3165	31	-0.027	0.174	0.007	0.067	3.533
PM I02123+0334	Gl 87	0.448	0.012	9.44	0.57	0.91215	0.01171	0.00027	3721	35	-0.023	0.421	0.011	0.049	3.479
PM I02129+0000W	GJ 3142	0.256	0.013	9.40	0.60	0.10611	0.00204	-0.00147	3321	33	-0.019	0.266	0.011	0.041	1.818
PM I02164+1335	GJ 3146	0.109	0.006	9.41	0.58	0.04531	0.00092	0.00013	2899	48	-0.025	0.135	0.006	0.064	2.477
PM I02171+3526	GJ 3147	0.117	0.002	9.39	0.61	0.04148	0.00099	0.00122	2919	26	-0.013	0.145	0.003	0.031	0.939
PM I02190+2352	GJ 3150	0.240	0.015	9.37	0.62	0.05424	0.00122	0.00151	3342	33	-0.039	0.251	0.012	0.083	6.819
PM I02222+4752	Gl 96	0.600	0.013	9.48	0.54	1.49357	0.02306	-0.00249	3892	38	-0.028	0.566	0.012	0.055	5.412
PM I02336+2455	Gl 102	0.182	0.010	9.42	0.59	0.17720	0.00288	-0.00018	3210	36	-0.003	0.201	0.009	0.013	0.089
PM I02358+2013	Gl 104	0.511	0.015	9.46	0.56	0.64364	0.00866	-0.00077	3647	39	-0.030	0.480	0.015	0.062	5.067
PM I02442+2531	Gl 109	0.358	0.011	9.37	0.58	0.90655	0.01172	0.00186	3502	29	-0.028	0.342	0.009	0.058	4.844
PM I02534+1724	...	0.339	0.019	9.53	0.58	0.14860	0.00189	-0.00028	3491	29	-0.034	0.325	0.016	0.076	5.567
PM I02555+2652	Gl 118.2 C	0.325	0.012	9.50	0.57	0.06822	0.00118	0.00152	3341	16	-0.035	0.323	0.008	0.071	6.416
PM I03181+3815	Gl 134	0.618	0.022	9.51	0.49	0.78493	0.01239	-0.00680	3795	63	-0.026	0.585	0.030	0.069	5.640
PM I03361+3118	...	0.194	0.009	9.39	0.61	0.09004	0.00163	0.00122	3214	33	-0.041	0.214	0.008	0.085	7.258
PM I03526+1701	GJ 3253	0.171	0.006	9.44	0.60	0.11150	0.00217	0.00073	3171	29	-0.030	0.192	0.005	0.062	4.271
PM I04290+2155	Gl 169	0.711	0.014	9.46	0.49	3.04166	0.05677	-0.00461	4197	40	-0.018	0.661	0.011	0.038	2.899
PM I04376+5253	Gl 172	0.602	0.016	9.45	0.51	2.48586	0.03408	-0.00252	4054	38	-0.032	0.571	0.011	0.061	7.993
PM I04376-1102	Gl 173	0.473	0.013	9.47	0.59	0.83533	0.01244	0.00009	3668	33	0.001	0.444	0.012	0.000	0.010
PM I04429+1857	Gl 176	0.496	0.015	9.36	0.58	1.25666	0.01728	-0.00235	3631	40	0.013	0.464	0.014	-0.027	1.149
PM I04538-1746	Gl 180	0.417	0.015	9.44	0.55	0.52595	0.00721	-0.00049	3619	31	-0.032	0.392	0.013	0.069	5.948
PM I05019-0656	GJ 3323	0.173	0.004	9.38	0.60	0.39830	0.00710	0.00277	3204	24	-0.019	0.192	0.004	0.043	2.258
PM I05033-1722	GJ 3325	0.274	0.013	9.45	0.61	0.35206	0.00580	0.00144	3410	25	-0.013	0.276	0.009	0.030	1.007
PM I05314-0340	Gl 205	0.613	0.010	9.41	0.48	6.37047	0.13131	-0.00477	3805	31	-0.001	0.579	0.009	0.004	0.655
PM I05365+1119	Gl 208	0.620	0.015	9.43	0.52	2.04526	0.02948	-0.00282	4020	41	-0.013	0.585	0.012	0.026	1.536
PM I05415+5329	Gl 212	0.584	0.011	9.40	0.57	1.20701	0.02460	-0.00159	3819	34	-0.014	0.550	0.011	0.032	1.505
PM I05421+1229	Gl 213	0.234	0.009	9.41	0.62	0.59902	0.01334	0.00196	3370	23	-0.037	0.243	0.007	0.076	7.212
PM I05557-2651	...	0.550	0.017	9.47	0.56	0.66548	0.01051	-0.00188	3671	41	-0.005	0.519	0.016	0.012	0.193
PM I06000+0242	GJ 3379	0.237	0.007	9.37	0.61	0.77613	0.01922	0.00066	3297	30	-0.026	0.249	0.006	0.053	3.762
PM I06011+5935	GJ 3378	0.255	0.010	9.41	0.61	0.46026	0.01288	0.00226	3381	26	-0.012	0.261	0.007	0.028	0.947
PM I06024+4951	GJ 3380	0.131	0.005	9.39	0.60	0.07624	0.00181	0.00182	3044	32	-0.015	0.157	0.005	0.037	1.219
PM I06077-2544	...	0.307	0.015	9.46	0.62	0.29037	0.00610	0.00336	3455	25	-0.029	0.300	0.011	0.064	4.637
PM I06140+5140	GJ 3388	0.268	0.013	9.40	0.61	0.12769	0.00255	0.00220	3394	29	-0.020	0.271	0.010	0.045	2.237
PM I06246+2325	Gl 232	0.167	0.008	9.41	0.60	0.14582	0.00315	0.00367	3216	30	-0.016	0.187	0.007	0.041	1.508
PM I06371+1733	Gl 239	0.461	0.012	9.39	0.57	1.13859	0.02213	-0.00305	3758	37	0.012	0.434	0.011	-0.025	1.098
PM I06490+3706	GJ 1092	0.169	0.009	9.39	0.58	0.06790	0.00189	-0.00287	3298	41	-0.028	0.188	0.009	0.066	4.544
PM I06548+3316	Gl 251	0.365	0.009	9.38	0.58	1.66551	0.02223	0.00148	3487	31	-0.011	0.349	0.008	0.025	0.880
PM I07232+4605	Gl 272	0.550	0.018	9.42	0.53	0.59251	0.00834	-0.00169	3786	46	-0.022	0.518	0.016	0.046	2.911
PM I07274+0513	Gl 273	0.298	0.009	9.44	0.60	2.39110	0.03007	0.00143	3438	26	-0.037	0.293	0.005	0.070	7.787
PM I07287-0317	GJ 1097	0.405	0.017	9.45	0.60	0.43861	0.01329	0.00138	3530	38	-0.024	0.381	0.015	0.055	3.251
PM I07344+6256	Gl 277.1	0.411	0.015	9.42	0.57	0.59395	0.01402	0.00106	3667	37	0.004	0.386	0.013	-0.002	0.065
PM I07386-2113	GJ 3459	0.300	0.017	9.44	0.60	0.32331	0.00832	0.00101	3452	28	-0.028	0.295	0.013	0.064	4.010
PM I07393+0211	Gl 281	0.608	0.016	9.48	0.50	1.07584	0.01406	-0.00182	3922	46	-0.040	0.574	0.013	0.083	10.950
PM I07482+2022	Gl 289	0.364	0.019	9.42	0.57	0.27007	0.00399	0.00072	3609	33	-0.009	0.345	0.015	0.026	0.687
PM I08161+0118	GJ 2066	0.451	0.012	9.50	0.58	1.10058	0.01833	0.00003	3644	30	-0.041	0.423	0.009	0.081	10.637
PM I08526+2818	Gl 324B	0.243	0.010	9.41	0.61	0.16444	0.00296	0.00042	3237	17	-0.022	0.259	0.008	0.050	2.564
PM I09143+5241	Gl 338A	0.580	0.019	9.41	0.55	6.10684	0.08455	-0.00325	3930	52	-0.002	0.548	0.018	0.003	0.155
PM I09319+3619	Gl 353	0.510	0.015	9.42	0.54	0.74337	0.00993	-0.00194	3806	37	-0.031	0.483	0.013	0.067	6.400
PM I09411+1312	Gl 361	0.473	0.014	9.49	0.59	0.79918	0.01080	0.00147	3648	37	-0.042	0.442	0.012	0.088	11.261
PM I09447-1812	GJ 1129	0.272	0.013	9.36	0.62	0.24568	0.00666	0.00216	3334	33	-0.028	0.277	0.010	0.063	4.256
PM I09553-2715	...	0.311	0.019	9.40	0.61	0.28934	0.00579	0.00073	3412	35	-0.020	0.305	0.014	0.048	2.115
PM I10113+4927	Gl 380	0.687	0.013	9.43	0.49	14.98949	0.17236	-0.00266	4162	33	-0.008	0.642	0.010	0.014	0.631
PM I10122-0344	Gl 382	0.532	0.012	9.48	0.56	2.18721	0.02719	-0.00055	3696	36	-0.020	0.500	0.012	0.042	2.856
PM I10196+1952	Gl 388	0.427	0.011	9.46	0.57	2.93513	0.05533	0.00174	3492	33	-0.036	0.402	0.010	0.075	8.070
PM I10251-1013	Gl 390	0.516	0.016	9.46	0.56	0.87788	0.01091	-0.00133	3743	41	-0.011	0.485	0.014	0.024	0.930
PM I10289+0050	Gl 393	0.428	0.010	9.45	0.57	1.61261	0.01949	-0.00036	3621	24	-0.020	0.402	0.009	0.043	2.838
PM I10430-0912	...	0.149	0.007	9.41	0.59										

Table 7 — *Continued*

LG11/LSPM Name	CNS3	Mass (M_{\odot})	σ_M	log(age) (yr)	σ_{age}	F_{bol} ($10^{-8} \text{ erg s}^{-1} \text{ cm}^{-2}$)	$\sigma_{F_{\text{bol}}}$	δF_{bol}	T_{eff} (K)	σ_T	δT_{eff}	Radius (R_{\odot})	σ_R	δR	χ^2
PM I11421+2642	Gl 436	0.447	0.015	9.47	0.57	0.82784	0.01482	-0.00023	3584	39	-0.030	0.420	0.014	0.066	5.702
PM I11477+0048	Gl 447	0.176	0.004	9.45	0.60	1.02653	0.02011	0.00169	3201	26	-0.003	0.195	0.004	0.008	0.081
PM I11509+4822	GJ 1151	0.163	0.007	9.40	0.60	0.16780	0.00326	0.00191	3152	31	-0.011	0.185	0.006	0.029	0.743
PM I12100-1504	GJ 3707	0.397	0.017	9.44	0.59	0.35001	0.00558	-0.00039	3420	33	-0.010	0.380	0.014	0.026	0.668
PM I12151+4843	Gl 458.2	0.643	0.023	9.45	0.52	0.48290	0.00656	-0.00225	4037	72	-0.035	0.605	0.021	0.096	8.550
PM I12194+2822	Gl 459.3	0.672	0.018	9.46	0.48	0.47229	0.00720	-0.00373	4027	69	-0.008	0.630	0.016	0.021	0.696
PM I12312+0848	Gl 471	0.572	0.016	9.46	0.52	1.04498	0.01379	-0.00208	3896	42	-0.045	0.541	0.014	0.086	13.365
PM I12388+1141	Gl 480	0.471	0.021	9.45	0.59	0.43682	0.00685	-0.00002	3529	41	-0.019	0.443	0.020	0.050	2.104
PM I12507-0046	Gl 488	0.663	0.013	9.42	0.51	2.72815	0.03081	-0.00244	4067	36	-0.019	0.622	0.011	0.036	3.132
PM I13196+3320	Gl 507.1	0.591	0.013	9.50	0.50	0.63407	0.00776	-0.00117	3752	36	-0.028	0.560	0.013	0.063	5.192
PM I13283-0221Ww	Gl 512A	0.463	0.020	9.49	0.58	0.47581	0.01083	0.00091	3581	43	-0.024	0.435	0.019	0.058	3.266
PM I13299+1022	Gl 514	0.505	0.012	9.45	0.55	2.21200	0.02769	-0.00266	3755	30	-0.008	0.476	0.009	0.014	0.502
PM I13450+1747	Gl 525	0.500	0.014	9.45	0.53	0.86801	0.02035	-0.00887	3896	37	-0.018	0.476	0.015	0.037	4.020
PM I13457+1453	Gl 526	0.475	0.010	9.51	0.56	4.01259	0.08146	0.00003	3755	32	-0.029	0.450	0.009	0.058	6.178
PM I14201-0937	Gl 545	0.262	0.010	9.34	0.63	0.14016	0.00363	0.00083	3403	21	-0.018	0.265	0.007	0.040	1.958
PM I14342-1231	Gl 555	0.283	0.012	9.42	0.59	0.79806	0.01179	0.00040	3322	32	-0.035	0.287	0.009	0.072	6.385
PM I15194-0743E	Gl 581	0.306	0.011	9.44	0.58	0.95994	0.01111	0.00095	3457	22	-0.018	0.299	0.007	0.040	2.120
PM I15238+1727	Gl 585	0.159	0.010	9.45	0.61	0.09749	0.00204	0.00165	3213	36	-0.015	0.180	0.008	0.038	1.111
PM I16254+5418	Gl 625	0.333	0.009	9.54	0.60	1.08685	0.01793	0.00052	3540	34	-0.018	0.319	0.007	0.038	2.338
PM I16303-1239	Gl 628	0.303	0.010	9.43	0.58	1.89620	0.02520	0.00036	3411	34	-0.042	0.299	0.006	0.082	10.202
PM I16509+2227	GJ 3976	0.156	0.007	9.43	0.60	0.09327	0.00154	0.00133	3171	28	-0.038	0.178	0.006	0.083	6.501
PM I16542+1154	Gl 642	0.488	0.018	9.40	0.53	0.37167	0.00645	-0.00371	3868	53	-0.009	0.464	0.020	0.022	0.903
PM I16554-0819	Gl 643	0.209	0.009	9.41	0.60	0.40074	0.00728	-0.00049	3339	27	-0.018	0.223	0.008	0.041	1.904
PM I16570-0420	GJ 1207	0.233	0.007	9.36	0.61	0.28570	0.00692	0.00154	3346	27	-0.036	0.244	0.006	0.069	6.673
PM I16581+2544	Gl 649	0.527	0.013	9.42	0.57	1.29973	0.01963	-0.00102	3741	39	-0.011	0.495	0.012	0.024	1.004
PM I17095+4340	GJ 3991	0.274	0.010	9.40	0.59	0.49539	0.00794	-0.00059	3309	31	-0.007	0.281	0.007	0.019	0.418
PM I17115+3826	GJ 3992	0.388	0.015	9.41	0.58	0.40893	0.00717	0.00106	3493	36	-0.018	0.368	0.012	0.043	1.982
PM I17198+4142	Gl 671	0.377	0.013	9.49	0.58	0.38036	0.00597	0.00216	3534	27	-0.029	0.357	0.010	0.064	5.175
...	Gl 673	0.678	0.014	9.46	0.49	5.94176	0.06313	-0.00257	4170	36	-0.011	0.636	0.010	0.021	1.139
PM I17303+0532	Gl 678.1A	0.534	0.014	9.46	0.54	1.55792	0.02159	-0.00089	3811	36	-0.037	0.504	0.011	0.072	9.740
PM I17355+6140	Gl 685	0.576	0.014	9.43	0.58	0.93072	0.01630	-0.00275	3844	38	0.001	0.543	0.012	-0.003	0.074
PM I17364+6820	Gl 687	0.418	0.010	9.47	0.58	3.36221	0.04364	0.00027	3522	34	-0.024	0.394	0.008	0.049	3.923
PM I17378+1835	Gl 686	0.445	0.010	9.41	0.57	1.42084	0.02168	-0.00176	3678	29	-0.006	0.418	0.009	0.014	0.322
PM I17439+4322	Gl 694	0.440	0.011	9.46	0.56	0.89305	0.01379	-0.00045	3572	36	-0.031	0.412	0.010	0.063	5.965
PM I17578+0441N	Gl 699	0.162	0.004	9.39	0.61	3.25782	0.08858	0.00156	3269	29	-0.012	0.181	0.004	0.027	1.016
PM I17578+4635	GJ 4040	0.406	0.016	9.45	0.59	0.33036	0.00730	0.00185	3514	37	-0.012	0.383	0.013	0.034	1.196
PM I18046+1354	...	0.263	0.009	9.39	0.61	0.07790	0.00168	0.00186	3412	23	-0.011	0.266	0.007	0.028	0.848
PM I18051-0301	Gl 701	0.464	0.009	9.51	0.54	1.72226	0.02062	-0.00114	3701	26	-0.024	0.437	0.008	0.047	3.914
PM I18165+4533	Gl 709	0.558	0.015	9.46	0.55	0.64048	0.01077	-0.00192	3881	40	-0.025	0.528	0.012	0.054	4.866
PM I18363+1336S	GJ 4065	0.262	0.010	9.36	0.59	0.23873	0.00439	0.00088	3339	32	-0.036	0.269	0.008	0.076	6.774
PM I18411+2447S	GJ 1230A	0.348	0.016	9.55	0.60	0.42908	0.02043	0.00448	3365	31	-0.041	0.341	0.013	0.085	8.298
PM I18419+3149	GJ 4070	0.380	0.016	9.38	0.59	0.45495	0.00903	0.00154	3538	29	-0.041	0.359	0.013	0.087	8.571
PM I18427+5937N	Gl 725A	0.349	0.008	9.47	0.60	3.89003	0.06776	0.00192	3517	22	-0.022	0.334	0.006	0.047	3.302
PM I18427+5937S	Gl 725B	0.255	0.008	9.41	0.61	2.24335	0.05514	0.00053	3421	29	-0.023	0.259	0.006	0.049	3.305
PM I18453+1851	...	0.192	0.005	9.38	0.61	0.08751	0.00173	0.00123	3273	23	-0.018	0.209	0.004	0.037	1.821
PM I18498-2350	Gl 729	0.181	0.004	9.44	0.57	1.44826	0.02560	0.00186	3252	21	-0.004	0.199	0.003	0.011	0.160
PM I18580+0554	Gl 740	0.591	0.014	9.48	0.57	1.70112	0.02128	-0.00198	3872	41	-0.010	0.558	0.013	0.020	0.755
PM I19070+2053	Gl 745A	0.316	0.013	9.50	0.59	0.57069	0.01052	0.00142	3516	34	-0.004	0.305	0.010	0.016	0.259
PM I19072+2052	Gl 745B	0.327	0.014	9.54	0.61	0.58142	0.01628	0.00511	3532	34	-0.011	0.314	0.011	0.029	0.959
PM I19169+0510	Gl 752A	0.488	0.011	9.45	0.56	3.01805	0.03599	-0.00020	3619	34	-0.017	0.457	0.010	0.036	2.200
PM I19220+0702	GJ 1236	0.217	0.006	9.45	0.59	0.18285	0.00373	0.00036	3365	29	-0.009	0.229	0.006	0.022	0.533
PM I19539+4424E	Gl 1245B	0.110	0.004	9.49	0.60	0.19831	0.00530	0.00126	2919	34	-0.021	0.136	0.004	0.048	1.985
PM I20034+2951	Gl 777B	0.182	0.007	9.39	0.60	0.06201	0.00209	0.00207	3190	31	-0.015	0.202	0.007	0.033	1.087
PM I20112+1611	Gl 783.2B	0.215	0.015	9.36	0.61	0.06300	0.00152	0.00284	3330	26	-0.035	0.229	0.012	0.090	5.682
PM I20260+5834	GJ 1253	0.152	0.008	9.41	0.61	0.10231	0.00295	0.00172	3084	33	-0.013	0.177	0.007	0.031	0.787
PM I20450+4429	Gl 806	0.444	0.013	9.47	0.59	0.58441	0.01083	0.00167	3640	30	-0.028	0.416	0.011	0.060	4.747
PM I20525-1658	...	0.234	0.009	9.41	0.62	0.65648	0.01944	0.00374	3317	32	-0.035	0.246	0.008	0.074	6.653
PM I20533+6209	Gl 809	0.546	0.013	9.39	0.54	3.35835	0.05639	-0.00306	3846	37	-0.015	0.515	0.010	0.027	1.665
PM I20567-1026	Gl 811.1	0.460	0.025	9.42	0.57	0.37245	0.00587	-0.00127	3545	46	-0.021	0.431	0.022	0.055	2.307
LSPM J2106+3844S	Gl 820B	0.600	0.014	9.43	0.52	22.32370	0.29702	-0.00321	4126	36	-0.026	0.574	0.010	0.048	3.810
PM I21092-1318	Gl 821	0.372	0.014	9.43	0.58	0.41750	0.00851	0.00232	3620	33	-0.021	0.352	0.011	0.047	2.871
PM I22021+0124	Gl 846	0.571	0.015	9.43	0.54	1.79593	0.02242	-0.00271	3875	40	-0.007	0.538	0.012	0.013	0.444
PM I22096-0438	Gl 849	0.495	0.011	9.40	0.58	1.19212	0.01589	-0.00040	3537	32	-0.002	0.467	0.011	0.006	0.050
PM I22290+0139	...	0.604	0.021	9.41	0.53	0.48700	0.00696	-0.00321	3924	56	-0.005	0.569	0.019	0.010	0.270
PM I22361-0050	Gl 864	0.612	0.018	9.46	0.52	0.83252	0.01097	-0.00269	3976	52	-0.015	0.577	0.017	0.037	1.934
PM I22503-0705	Gl 875	0.562	0.016	9.44	0.53	0.89628	0.01202	-0.00155	3836	46	-0.026	0.529	0.015	0.060	4.737
PM I22532-1415	Gl 876	0.341	0.010	9.51	0.58	1.91585	0.02277	-0.00010	3384	32	-0.042	0.333	0.008	0.083	10.077
PM I22565+1633	Gl 880	0.570	0.011	9.46	0.52	3.55013	0.04076	-0.00149	3760	35	-0.011	0.537	0.010	0.021	0.893
...	Gl 887	0.491	0.011	9.46	0.58	10.90031	0.25215	-0.00053	3715	33	-0.007	0.461	0.009	0.015	0.207
PM I23099+1425W	...	0.637	0.016	9.45	0.50	0.50300									

Table 7 — *Continued*

LG11/LSPM Name	CNS3	Mass (M_{\odot})	σ_M	log(age) (yr)	σ_{age}	F_{bol} ($10^{-8} \text{ erg s}^{-1} \text{ cm}^{-2}$)	$\sigma_{F_{\text{bol}}}$	δF_{bol}	T_{eff} (K)	σ_T	δT_{eff}	Radius (R_{\odot})	σ_R	δR	χ^2
PM I23505-0933	GJ 4367	0.293	0.015	9.41	0.60	0.11917	0.00386	0.00387	3287	28	-0.020	0.299	0.011	0.050	2.315
PM I01076+2257E	Gl 53.1B	0.287	0.012	9.42	0.61	0.06732	0.00188	0.00222	3311	17	-0.024	0.292	0.008	0.053	3.249
PM I02362+0652	Gl 105 B	0.255	0.005	9.36	0.61	0.49982	0.00961	0.00128	3390	7	-0.032	0.260	0.002	0.063	5.970
PM I02441+4913W	...	0.521	0.008	9.38	0.59	1.06576	0.03519	-0.00140	3720	22	-0.010	0.489	0.007	0.019	0.662
PM I03047+6144	GJ 3195	0.425	0.011	9.46	0.60	0.13168	0.00253	0.00259	3602	27	-0.029	0.399	0.009	0.059	5.202
LSPM J0355+5214	...	0.268	0.011	9.41	0.61	0.02098	0.00042	0.00094	3466	23	-0.009	0.268	0.007	0.023	0.579
...	Gl 166 C	0.233	0.005	9.44	0.60	0.87259	0.01922	0.00191	3362	18	-0.061	0.242	0.004	0.115	19.414
PM I06461+3233	GJ 3408 B	0.440	0.013	9.42	0.60	0.13147	0.00396	-0.00140	3674	28	-0.005	0.414	0.013	0.013	0.185
PM I06523-0511	Gl 250 B	0.466	0.008	9.41	0.60	1.17659	0.03158	0.00314	3569	19	-0.025	0.436	0.006	0.052	4.199
PM I08105-1348	Gl 297.2 B	0.510	0.012	9.48	0.55	0.24811	0.00374	-0.00056	3700	39	-0.044	0.479	0.011	0.083	12.010
PM I13168+1700	Gl 505 B	0.531	0.008	9.48	0.55	1.29287	0.03335	-0.00022	3840	21	-0.035	0.502	0.006	0.069	8.883
...	Gl 544 B	0.178	0.005	9.43	0.60	0.02826	0.00064	0.00089	3242	13	-0.016	0.196	0.004	0.038	1.560
PM I14251+5149	Gl 549 B	0.415	0.009	9.41	0.59	0.34152	0.00834	0.00258	3585	27	-0.030	0.389	0.007	0.060	5.948
PM I15118+3933	...	0.347	0.012	9.46	0.59	0.05328	0.00095	0.00230	3495	16	-0.017	0.333	0.010	0.041	1.922
PM I15354+6005	...	0.292	0.010	9.45	0.61	0.08919	0.00206	0.00254	3390	34	-0.042	0.292	0.008	0.083	9.946
PM I16139+3346	Gl 615.2 C	0.426	0.013	9.47	0.58	0.17621	0.00369	0.00135	3593	23	-0.040	0.400	0.011	0.086	8.656
PM I18007+2933	...	0.458	0.009	9.50	0.56	0.11690	0.00264	0.00086	3648	21	-0.039	0.428	0.008	0.077	9.048
PM I19321-1119	...	0.230	0.006	9.40	0.61	0.06567	0.00146	0.00170	3299	14	-0.027	0.244	0.004	0.057	4.146
PM I20167+5017	...	0.447	0.013	9.36	0.59	0.08471	0.00183	0.00214	3541	36	0.005	0.419	0.012	-0.004	0.143
PM I21518+4220E	Gl 838.3 B	0.556	0.017	9.41	0.57	0.20971	0.00593	-0.00056	3871	43	-0.026	0.525	0.014	0.057	4.880
PM I22160+5439	GJ 4269	0.259	0.008	9.39	0.63	0.05603	0.00147	0.00318	3360	31	-0.041	0.265	0.007	0.083	8.586

† Relative errors quoted as $\delta X = (X_{\text{obs}} - X_{\text{model}})/X_{\text{obs}}$